TECHNISCHE UNIVERSITÄT MÜNCHEN

Lehrstuhl für Hochfrequenztechnik

Radio Frequency Device and System Design Using Radio Frequency Switches Based on Micro Electro Mechanical Systems

Tae Young Kim

Vollständiger Abdruck der von der Fakultät für Elektrotechnik und Informationstechnik der Technischen Universität München zur Erlangung des akademischen Grades eines

Doktor-Ingenieurs

genehmigten Dissertation

Vorsitzender: Prof. Dr. rer. nat. Marc Tornow

Prüfer der Dissertation: 1. Prof. Dr.-Ing. Thomas Eibert

2. Prof. Dr.-Ing. Georg Fischer

Die Dissertation wurde am 23.11.2017 bei der Technischen Universität München eingereicht und durch die Fakultät für Elektrotechnik und Informationstechnik am 16.03.2018 angenommen.

Abstract

This dissertation discusses radio frequency (RF) device and system design using radio frequency switches based on micro electro mechanical systems (MEMS) where a particular focus is also on the corresponding design methodologies.

As a first contribution, the design of single-pole double-throw (SPDT) RF MEMS switches used in satellite redundancy systems is considered. Redundancy systems are widely used to secure a high reliability for space applications. The SPDT switch is an essential component of the redundancy system. In contrast to the heavy and bulky mechanical switches which have been used so far, RF MEMS SPDT switches are light and small while providing a low insertion loss (IL) and a high isolation up to high frequencies. In this work, two RF MEMS switches are cascaded to increase the isolation. Five types of SPDT switches are designed using various types of RF MEMS switching components (Ohmic series, capacitive shunt, etc.) according to the switch combination and accommodation. The measured results show that the SPDT switch consisting of two capacitive shunt switches possesses a good isolation performance at Ku band (12 GHz - 18 GHz). In terms of IL, a compact SPDT switch using an Ohmic series switch and a capacitive shunt switch shows the best performance out of five variants at Ku band. Overall, the presented SPDT switches result in a 0.8 dB - 1.3 dB IL, a 15.73 dB - 44.2 dB return loss (RL), and a 43.66 dB - 56.19 dB isolation.

As a second contribution, an RF MEMS switch matrix design for space applications is presented. The switch matrix is used in a communication satellite to provide full connectivity with high flexibility. Compared to the counter parts (mechanical switches, solid state switches), an RF MEMS switch matrix provides a low weight, a small size, a low power consumption and low loss signal transition with high linearity up to high frequencies. In this work, starting from a network architecture feasibility study, 4x4 and 12x12 RF MEMS switching matrix designs are presented based on a planar Beneš network. The planar Beneš network is based on RF MEMS double-pole double-throw (DPDT) switches. The low temperature co-fired ceramic (LTCC) technology is adopted to construct a multi-layered circuitry which is used to interconnect the RF MEMS DPDT switches. From the 12x12 switch matrix simulation, it is investigated that the IL is better than -18 dB up to C band (3.4 GHz - 4.2 GHz) and, the RL is better than -15 dB up to Ku band. The crosstalk is better than -40 dB up to C band. A fabricated and measured prototype of a 4x4 switch matrix was used to verify the 12x12 switch matrix design process. The measured performance agrees well with the simulated results. The RF MEMS switching components used up to here have been designed, fabricated and

measured by the University of Perugia, Italy and the Fondazione Bruno Kessler (FBK), Italy and the Consiglio Nazionalle delle Ricerche (CNR), Italy.

A further contribution of this thesis is a beam steerable leaky wave antenna design using RF MEMS technology and a Composite Right-/left-Handed Transmission Line (CRLH-TL). The CRLH-TL is a transmission line approach based on metamaterials (MTMs) and its phase constant can be varied by changing reactive loads. When the CRLH-TL is used for leaky wave antennas, changing the phase constant leads to beam firing direction change. In this work, the reactive loads of the CRLH-TL are controlled by RF MEMS components and corresponding beam firing direction changes are demonstrated by electromagnetic (EM) simulation. It is investigated that the beam is steered between backward and forward. To verify the CRLH-TL cell functionality, simplified test structures are fabricated and measured. The measurement shows that the dispersion curve is shifted according to the state of the reactive components. In addition to that, a two-dimensional beam steerable antenna is proposed and demonstrated by EM simulation. It is possible to combine phase shifters together with CRLH-TL leaky wave antennas, which enables two dimensional beam steering.

Finally, RF MEMS switch simulation and optimization methodologies using artificial neural networks (ANNs) are presented. ANNs are mathematical models inspired by the central nervous system, which enable a fast parameter prediction with much lower computing resources compared to the full wave or multi-physics simulators. In this work, the scattering parameters and the resonant frequency of Ohmic series and of capacitive shunt switches are predicted and demonstrated by ANNs. They show good agreement with EM simulations. The pull-in voltage of the RF MEMS switch is also predicted by ANNs, which is close to the result from multi-physics simulator. The ANN codes have been developed at the University of Nis, Serbia.

Contents

Acronyms and Notations

Acronyms

ANN	Artificial Neural Network
CMOS	Complementary Metal Oxide Semiconductor
CPW	Coplanar waveguide
CRLH-TL	Composite Right/Left-Handed Transmission Line
DPDT	Double Pole Double Throw
EM	Electromagnetic
FBK	Fondazione Bruno Kessler
FEM	Finite Element Method
FET	Field Effect Transistor
FIT	Finite Integration Technique
HEMT	High Electron Mobility Transistor
IL	Insertion Loss
LH	Left Handed
LPCVD	Low Pressure Chemical Vapor Deposition
LTCC	Low Temperature Cofired Ceramics
LWA	Leaky Wave Antenna
MEMS	Micro Electro Mechanical System
MESFET	MEtal Semiconductor Field Effect Transistor
MLP	Multilayer Perceptron
MMIC	Monolithic Microwave Integrated Circuit
MoM	Methods of Moments
MSL	Microstrip Line

MTM	Metematerial
PLH	Purely Left Handed
PRH	Purely Right Handed
PVD	Physical Vapor Deposition
RADAR	RAdio Detection And Ranging
RF	Radio Frequency
RH	Right Handed
RL	Return Loss
SOLT	Short-Open-Load-Thru
SPDT	Single Pole Double Throw
SPnT	Single Pole n-Throw
SPST	Single Pole Single Throw
TDMA	Time Division Multiple Access
TW-SRR	Thin Wires and Slit Ring Resonators

Symbols

α	attenuation constant
β	phase constant
Γ	reflection coefficient
γ	propagation constant
λ	wavelength
ω	angular frequency
θ	electric length
c	light speed
k	wave number
v_p	phase velocity
w_j	artificial neuron weights

1 Introduction

1.1 Switches using RF MEMS technology

A MEMS (Micro Electro Mechanical System) is essentially a miniature system which integrates sensors, actuators, mechanical components or electric circuits on a single substrate. An RF (Radio Frequency) MEMS is a specific type of MEMS, which generally involves reconfigurable sub-millimeter-sized parts to have specific RF functionalities. RF MEMS devices include switches, varactors, variable inductors, resonators, antennas, acoustic devices and filters, etc.

One representative RF MEMS utilization is an RF MEMS switch. RF MEMS switches have been referred to good candidates to replace conventional solid state devices, such as GaAs HEMT (High Electron Mobility Transistor), CMOS (Complementary Metal Oxide Semiconductor) transistors or PIN diodes. Compared to these counterparts, RF MEMS switches are highly linear up to the high frequency band while providing high isolation and low insertion loss. When they are actuated by an electrostatic force, they virtually do not consume power. However, RF MEMS switches generally require a high actuation voltage and the switching speed is relatively slow compared to solid state based devices.

Due to their small size, RF MEMS switches are normally produced by micro-machining technologies such as lithography, etching or deposition, which are now relatively mature technologies. Since the first prototype for microwave applications was reported in 1991, lot of researches have been carried out to improve and develop the performance of RF MEMS switches [Larson et al., 1991].

RF MEMS switches can be categorized according to their actuation mechanism, clamping methods, axis deflection directions, contacts or circuit building methods, etc. Table 1.1 lists various types of RF MEMS switches [Rebeiz, 2003b].

1.2 RF devices using RF MEMS switches

RF MEMS switches can be implemented into an RF device to add tunability. For example, a phase shifter is one of the representative applications. The phase shifter is widely used in radar, communication systems, sensor and measurement systems, etc. Conventionally, phase shifting has been achieved by semiconductor switches, such as PIN diodes or FETs (Field Effect Transistors), which generally consume power and possess non-linearity. RF MEMS phase shifters are gaining more interest due to a low loss, a

Criteria	Type	Description
Actuation	Electrostatic	consume no power, small, high switching speed, need high actuation voltage
	Magnetic	consume power
	Piezoelectric	consume no power
	Thermal	high contact force, slow, big, consume power
Clamping	Cantilever	need lower actuation force than bridge types
	Bridge	robust, reliable, need high actuation force
Axis deflection	Inline	small size
	Broadside	large size in general
Contacts	Capacitive	high isolation, narrowband
	Ohmic	broadband, contact resistance

Table 1.1: RF MEMS switch types and description [Rebeiz, 2003b]

high linearity and a low power consumption. RF MEMS phase shifters generally consist of several switches which digitally control the phase or time delay of the transmission line. There are several RF MEMS phase shifting approaches such as switched lines, loaded lines, reflective lines or distributed lines, etc.

Tunable filters and matching networks by RF MEMS switches are also attractive, since they can provide high adaptability to the varying signal conditions with low loss and high linearity together with high isolation. Generally, a broadband microwave system is partitioned by multiple channels and each channel is filtered or rejected by a dedicated narrowband filter. To achieve more band selection capability, more filters need to be accommodated, which consumes more area. A tunable filter is an alternative approach which promises a significant size reduction. RF MEMS tunable filters can provide filter tunability with low loss and high linearity. A tunable impedance matching network is also referred to as an attractive application of RF MEMS switches. This is mainly due to its low loss characteristic.

RF MEMS switches are used for other reconfigurable RF devices such as tunable antennas, metamaterials or resonators which require high Q operation up to microwave frequencies [Newman, 2002; Rebeiz, 2003a].

1.3 RF MEMS switches using FBK technology

1.3.1 Switch configurations

Figure 1.1 shows RF MEMS switches designed and fabricated by the University of Perugia and Fondazione Bruno Kessler (FBK). These switches are used to build RF devices which are discussed in Chapter 2 and Chapter 3.

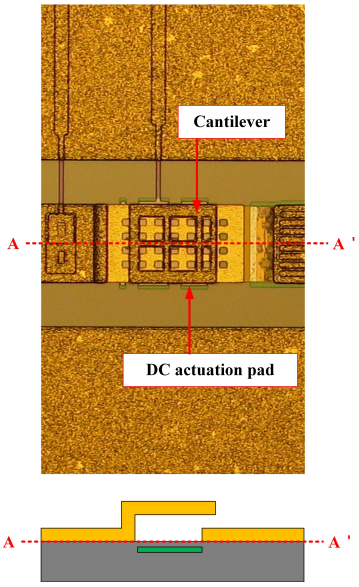

(a) Cantilever type Ohmic series switch

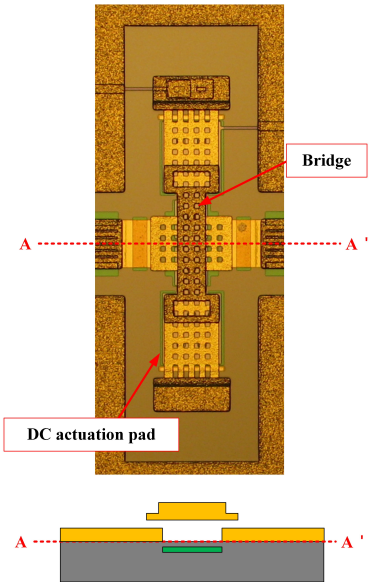

(b) Bridge type Ohmic series switch

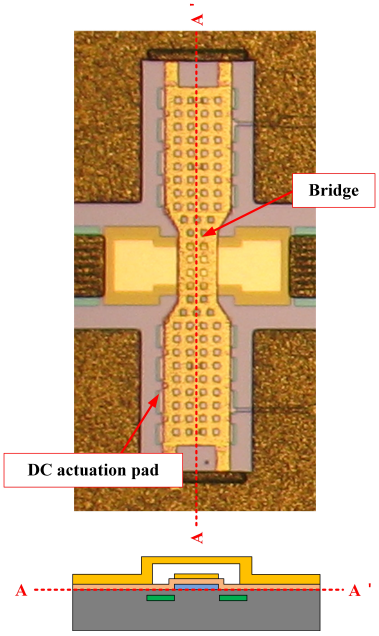

(c) Bridge type capacitive shunt switch

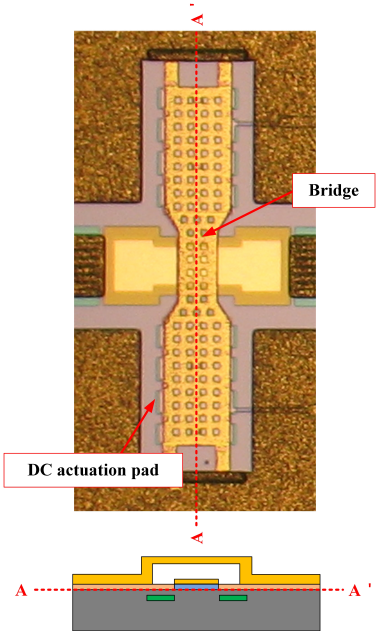

(d) Bridge type Ohmic shunt switch

Figure 1.1: RF MEMS switches using FBK technology [Farinelli et al., 2004; DiNardo et al., 2006]

Figure 1.1(a) describes a cantilever type Ohmic series switch. When the actuation voltage is applied to the DC actuation pad, the cantilever comes down and contacts the center line, which is the ON state. After the applied potential is removed, the cantilever comes back to the initial position by the mechanical restoring force - OFF-state. Compared to bridge type switches, a cantilever switch is simple and operated by a low actuation voltage. However, it has low isolation in OFF-state. Figure 1.1(b) shows the bridge type Ohmic series switch. Compared to the cantilever type, it has higher OFF-state isolation. However, it needs higher actuation voltage due to the clamped-clamped structure. Additionally, the ON-state IL (Insertion Loss) is higher due to the double Ohmic contacts. Figure 1.1(c) shows the bridge type capacitive shunt switch. The capacitive shunt switch uses a shunt resonance to achieve a high OFF-state isolation, which is discussed again in Chapter 2. This switch has no Ohmic contact part. Therefore, it has a low ON state IL. However, capacitive shunt switches can be operated in narrow bands, since they can only provide a narrowband rejection on the OFF-state(details are discussed in Chapter 2). Compared to the capacitive type, a bridge type Ohmic shunt switch (Figure 1.1(d)) is a more broadband approach. The difference is that the bridge is directly contacted to the CPW (Coplanar waveguide) centerline without intermediate dielectric materials like dielectric layers. The contact is Ohmic and a shunt capacitance does not exist at the bridge down state. The band rejection of the bridge type Ohmic shunt switch is more broadband. But the isolation is worse compared to the capacitive type [Farinelli et al., 2004; DiNardo et al., 2006].

1.3.2 Fabrication

As aforementioned, the RF MEMS switches in Figure 1.1 are fabricated by the FBK technology. The fabrication process is based on the standard silicon based CMOS (Complementary Metal Oxide Semiconductor) process. Figure 1.2 schematically shows the RF MEMS switch fabrication process [Farinelli et al., 2004; DiNardo et al., 2006].

- **Figure 1.2(a)**; The switches are fabricated on a 525 μm thick high-resistivity silicon wafer (5 kΩ-cm, <100>). After growing 1 μm thermal oxide for isolation, a 630 nm thick un-doped poly-silicon layer is deposited by 620 °C LPCVD (Low Pressure Chemical Vapor Deposition) and slightly doped with Boron by ion implantation to construct actuation pads, bias lines and Ohmic series switch contact dimples. The dimples secure an Ohmic contact. Next, a 300 nm silicon oxide passivation layer is deposited and a contact hole is defined.
- **Figure 1.2(b)**; The multi-layer underpass line (Ti/TiN/Al/Ti/TiN) is sputtered up to a comparable level to the poly silicon layer. When it is down, the bridge should touch on the underpass line before contacting the poly silicon layer.
- **Figure 1.2(c)**; The line is covered with a 100 nm thick low temperature oxide (LTO) layer. After defining LTO vias, the aluminum underpass line is exposed

by removing the TiN capping using a dry etching process. By using lithography and wet etching, a Cr/Au floating metal layer (5 nm/150 nm) is deposited by PVD (Physical Vapor Deposition). The floating metal secures capacitive switching by providing a bridge landing pad.

- **Figure 1.2(d)**; The air gap in the bridge/cantilever structure is fabricated by using a sacrificial layer formed by 4 μm thick positive photo resist.
- **Figure 1.2(e)**; An 1.8 μm thick gold layer is grown in a gold sulphite bath after forming a Cr/Au seedlayer (10 nm/150 nm). These are used for a bridge and grounds.
- **Figure 1.2(f)**; 2 μm thick Au layers are selectively grown for moving parts - bridge/cantilever - and a 4 μm thick Au layer for CPW and anchor posts. Lastly, the moving parts are released by a plasma ashing process to avoid stiction.

1.4 Thesis Overview

The thesis mainly discusses RF device design and optimization using RF MEMS switches. Chapter 2 deals with RF MEMS redundancy switches for space applications. In Chapter 3, a 12x12 RF MEMS switch matrix is discussed. Chapter 4 is dedicated to beam steerable smart antenna design using RF MEMS and metamaterial technologies. Chapter 5 introduces artificial neural networks as efficient RF MEMS switch design tool and Chapter 6 makes an overall conclusion.

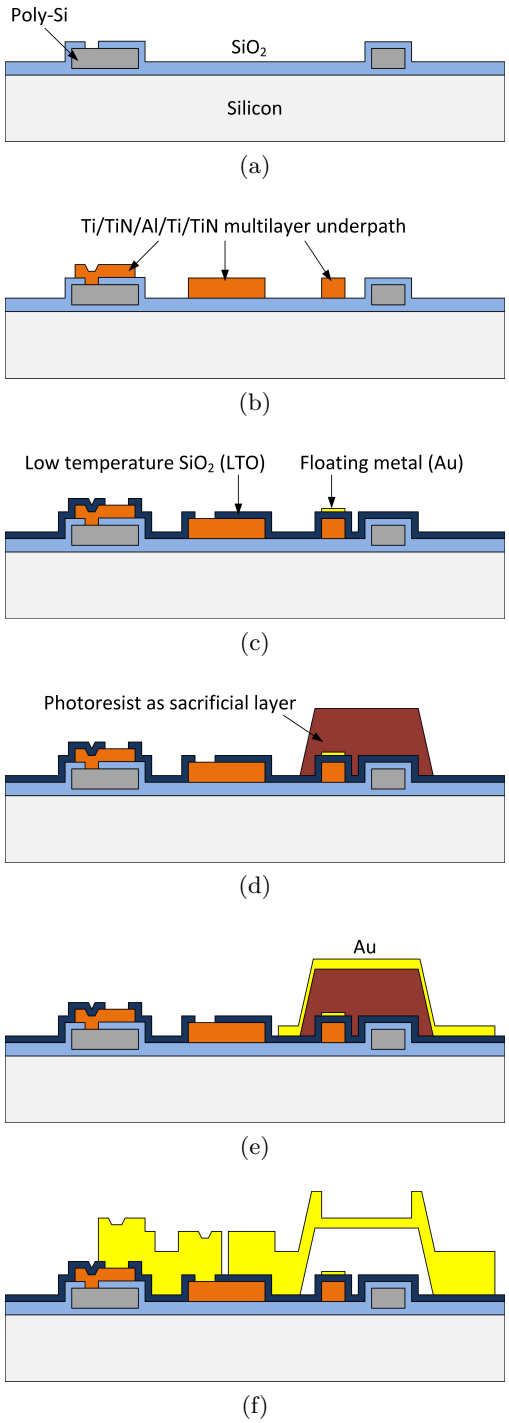

Figure 1.2: RF MEMS switch fabrication process schematic by FBK technology [Farinelli et al., 2004]

2 RF MEMS Redundancy Switch

2.1 Introduction

A redundancy system is an attractive solution when a system requires high reliability and availability. It generally increases system cost and complexity. However, if the cost of failure is significantly high, a redundancy system might be a good option.

Various redundancy concepts have been discussed, such as a standby redundancy, a N modular redundancy, and $1 : N$ redundancy systems, etc. They are basically based on the construction of additional backup paths. The backup path substitutes a main path when a failure on the main path is detected. Figure 2.1 shows the concepts of common standby redundancy systems. They consist of main and backup paths together with SPDT (Single Pole Double Through) switches. In a cold standby system (Figure 2.1(a)), a backup path is powered off, whereas a main path is powered on. The backup path can preserve the unit reliability, however, it needs a certain length of time to reach up to the operating state and be synchronized. In hot standby (Figure 2.1(b)), the backup path is already powered on and monitors the state of the main path. When a failure is detected, the backup path can quickly take over a role, which shortens the downtime and increases the availability. However, since it has been already powered on before the main path's failure, the life span of the backup path is expected to be shorter than the 'Cold Standby' case.

In a redundant system, SPDT switches are essential, since they control the path between Main and Backup. They are bi-directional and can have one input and two outputs or two inputs and one output. According to the control signal, the RF signal which is applied to the input port is routed to one of the two outputs (1:2) or on the other way around (2:1) [National-Instruments, 2008].

A redundancy system would be one of the most important parts in space application, such as a satellite broadcast or a communication system. Since they should be functional for a long time period (15 years in general) under a physically non-accessible environment, redundancy systems in space application should be highly reliable. This means, SPDT switches in the redundancy system should be highly reliable as well. Until now, mechanical SPDT switches like coaxial transfer switches have been used for the redundancy system because they can provide high reliability, low loss, high isolation and high immunity to space radiation. However, they are bulky and heavy, which makes the system complicated and requires high launching cost. As alternatives, solid-state switch based SPDTs can be discussed as an option, but they suffer from high insertion

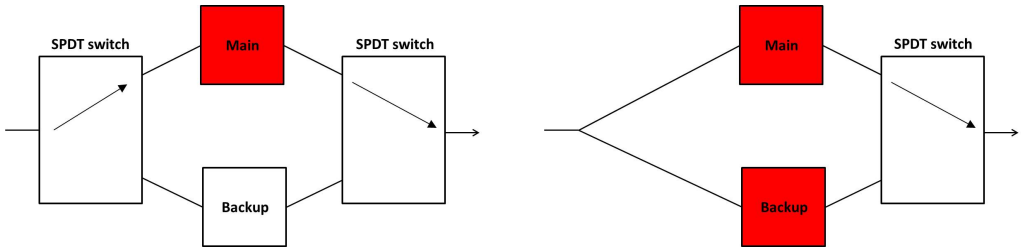

(a) Cold Standby (b) Hot Standby

Figure 2.1: Standby redundancy system

loss, constant power consumption, nonlinearity along with frequency increase and low immunity to the space radiation as well as temperature change. Recently, RF MEMS SPDT switches are referred as good candidates to replace mechanical switches. They are light, small, relatively immune to space radiation and possess a suitable RF performance for space application.

Parameter	**Specification**
Frequency band	12-18 GHz (Ku band)
RL	-15 dB max
IL	0.5 dB min
Isolation	50 dB min

Table 2.1: SPDT switch RF specification

2.2 Design

Table 2.1 shows RF specifications of the redundant SPDT switch, which is proposed from European Space Agency (ESA). Among those, the most critical item is the isolation. A redundant path should be well excluded from the unit operation when the other path is working. This mainly depends on the isolation performance of the SPDT switches. Among the RF MEMS switches depicted in Figure 1.1, a capacitive shunt switch (c) shows the best isolation at Ku band. However, it only provides 30 dB rejection. It turns out that 50 dB isolation cannot be easily achieved by a single switching component. Therefore, in this work, two-component switching is used by cascading two RF MEMS switches.

Table 2.2 lists the SPDT switch design approaches which are discussed in this work. They are based on the RF MEMS switching components in Figure 1.1. Figure 2.2 explains the terminology difference between ′not distanced′ and ′distanced′. In ′distanced′

Model	Switching elements	Remark
BB	Double capacitive shunt	No distance between switches
BB_Opt_T	Double capacitive shunt	Switches are distanced
SB	Ohmic series + Capacitive shunt	No distance between switches
SBO	Ohmic series + Ohmic shunt	Switches are distanced
CC	Double Ohmic series (cantilever type)	Redundant path

Table 2.2: RF MEMS SPDT switches

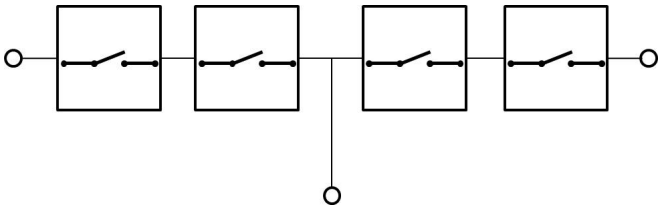

(a) Switches are NOT distanced

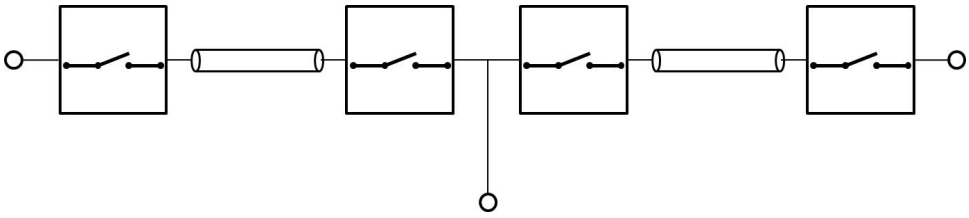

(b) Switches are distanced

Figure 2.2: Concept definition of the distance between switches

SPDT switches, a certain length of transmission line is inserted between switching components. In Table. 2.2, each configuration has its own advantages and disadvantages. For example, the series configurations have broadband nature but the isolation is low, whereas shunt switches are generally narrowband but have low IL and high isolation.

2.2.1 RF MEMS switch modeling and simulation

In Chapter 2, all RF MEMS switches have been modeled and optimized using the Momentum simulator provided by the commercial Advanced Design System (ADS) package [Keysight Technologies, 2009]. Since this is a 2.5D solver, the RF MEMS switches have been modeled as a stack of multiple layers. The ON/OFF states have been modeled as the air layer thickness change between a bridge and a center line layer. Figure 2.3 shows dielectric and metal layer definitions for the ADS Momentum simulation [Keysight Technologies, 2009]. Figure 2.4 shows a simplified capacitive shunt switch model for EM simulation and the meshed model. A poly silicon layer used for DC actuation pads has been ignored during simplification. The meshing frequency is 20 GHz and an adaptive frequency sweeping plan has been used.

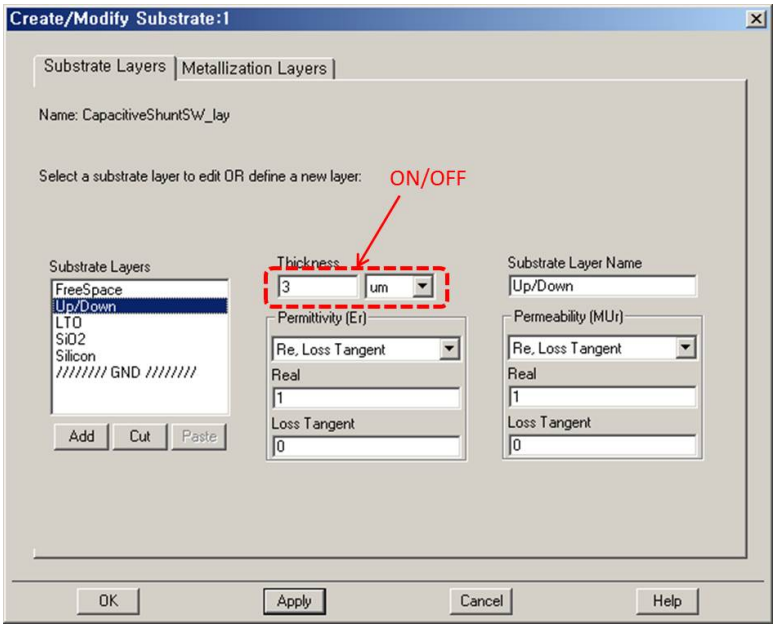

(a) Dielectric substrate definition

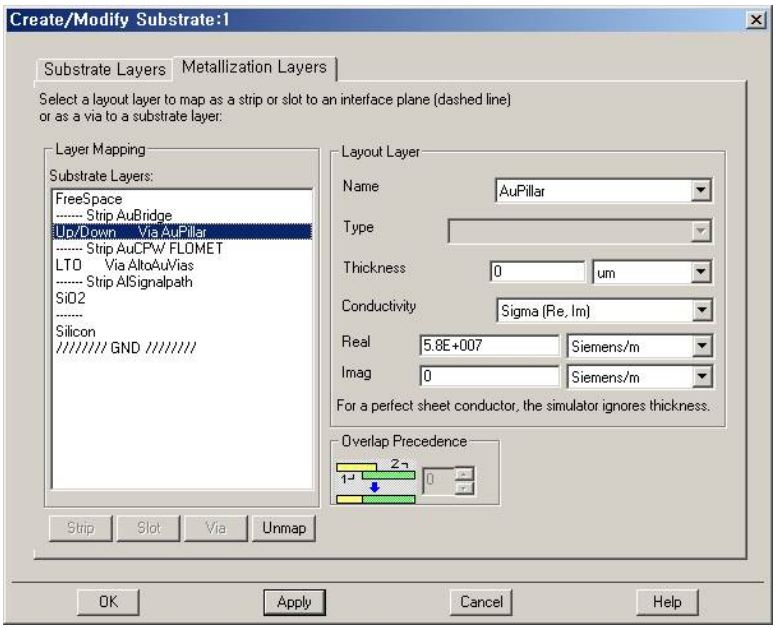

(b) Metal layer definition

Figure 2.3: RF MEMS switch layer definitions for ADS Momentum simulation [Keysight Technologies, 2009]

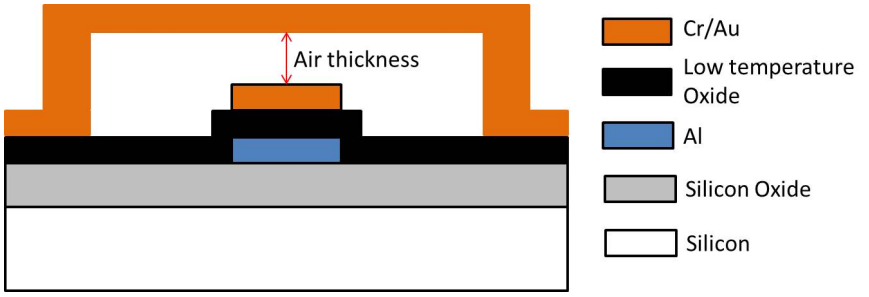

(a) Simplified capacitive shunt switch model for ADS Momentum simulation [Keysight Technologies, 2009]

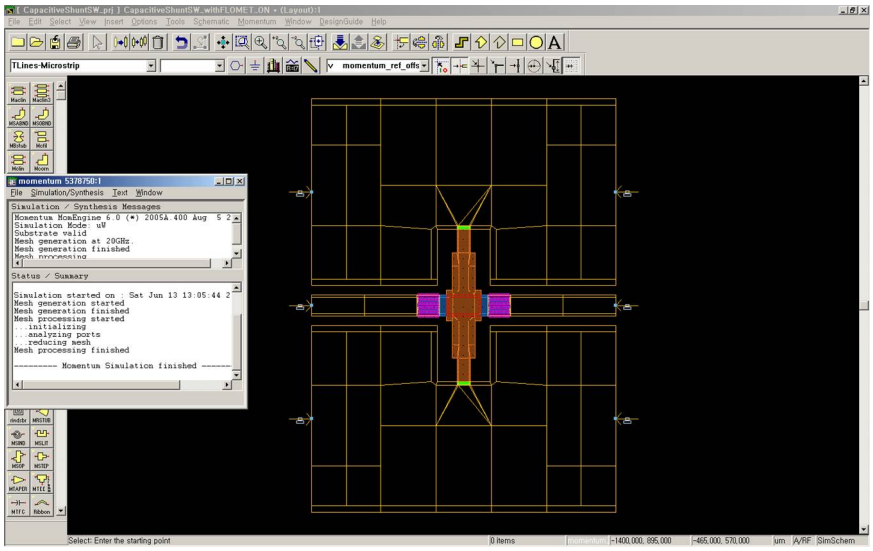

(b) Meshed model

Figure 2.4: EM model of the capacitive shunt switch for ADS Momentum simulation [Keysight Technologies, 2009]

2.2.2 BB (Capacitive Shunt + Capacitive Shunt)

A BB type SPDT switch has two capacitive shunt switches on each path. Capacitive shunt switches use their bridge downstate LC resonance to reject RF signals. It consists of a membrane bridge suspended over the center line of a CPW. The bridge is anchored on the ground conductor in both ends (see Figure 1.1(c)). When a DC voltage is applied on the actuation pads, an electrostatic force is induced and the suspended bridge is snapped down onto the dielectric surface on the CPW center line, which forms a low impedance path to the ground at the downstate LC resonant frequency. Figure 2.5 shows the equivalent circuit representation of the capacitive shunt switch. C_b is the capacitance between a bridge and a center line. According to the bridge position, the bridge capacitance (C_b) is varied from upstate (C_u) to downstate (C_d) capacitance. This capacitance change shifts the LC resonant frequency. R_{DC} and C_{DC} are resistive and reactive components from the DC actuation lines, which are mainly pronounced when the bridge is up where C_b is comparable to C_{DC}. At the bridge down state, they are usually ignored. At the shunt resonant frequency, the switch is grounded by a small bridge resistance R_b, which leads to a high signal rejection. R_{se} is the loss of the transmission line between the reference planes.

In the BB type SPDT switch, capacitive shunt switches are directly cascaded. Figure 2.6 and Figure 2.7 show a BB type SPDT switch and its equivalent circuit representation. To minimize the accommodation area, a Y-junction is used, which makes the chip more compact and rectangular. In the junction and CPW bending positions, air bridges are constructed to suppress an odd CPW mode. DC control pads are made to apply the DC control voltage to the switching components.

The equivalent circuit representation in Figure 2.7 supposes that the path P1-P2 is

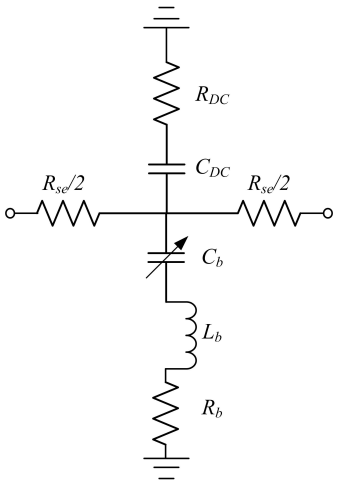

Figure 2.5: Equivalent circuit representation of the capacitive shunt switch

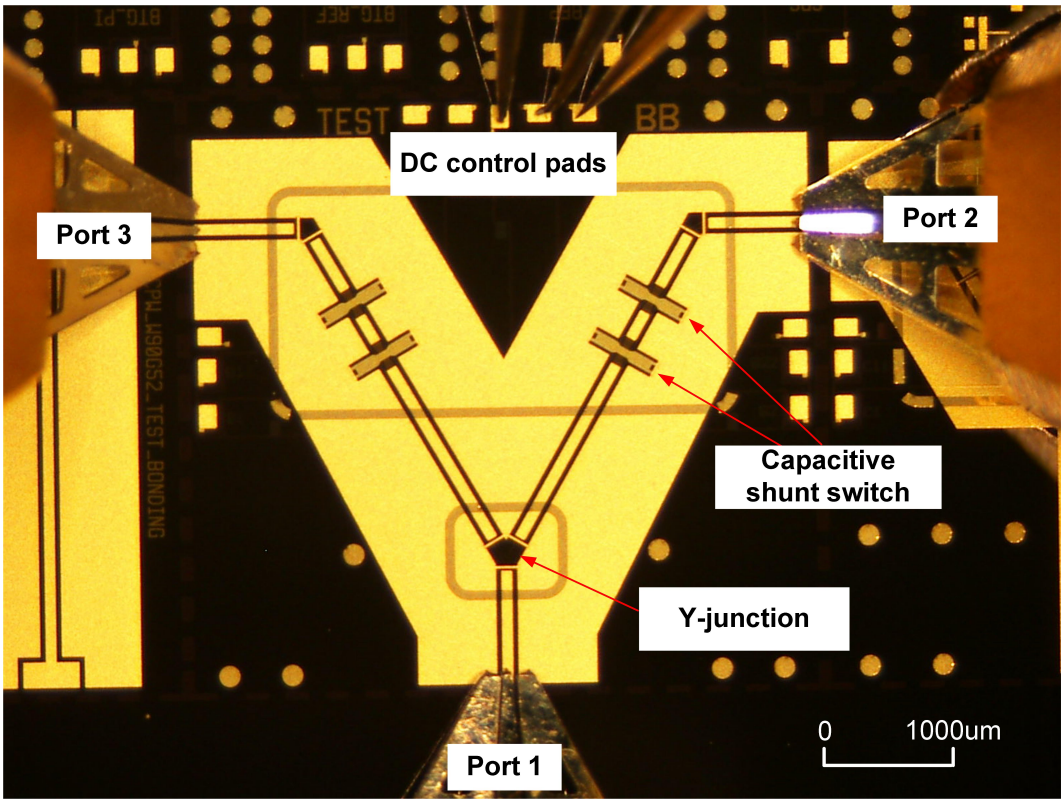

Figure 2.6: BB type SPDT switch [TUM et al., 2012]

switched ON and the path P1-P3 OFF. Y_{ON} and Y_{OFF} correspond to the ON/OFF shunt admittances of the switches accordingly, which are given as

$$Y_{ON} = \frac{1}{R_b + j\omega L_b + \frac{1}{j\omega C_{up}}} + \frac{1}{R_{DC} + \frac{1}{j\omega C_{DC}}}, \tag{2.1}$$

$$Y_{OFF} = \frac{1}{R_b + j\omega L_b + \frac{1}{j\omega C_{down}}}. \tag{2.2}$$

C_{up} and C_{down} are the bridge up/down state shunt capacitances between the bridge and the CPW centerline.

In the path P1-P3 in Figure 2.7, the bridges of two capacitive shunt switches are down. Their reactive components are canceled out and $Y_{OFF} = 1/R_b$. Considering the bridge resistance R_b is very small, the bridges are almost shorted to the ground. However, from the junction's point of view, the path to Port 3 should be opened. This open-short transition is done by a θ_1 long transmission line. Considering $\Gamma_2 \approx 1\angle 180°$, θ_1 can be expected as a quarter wavelength ($\lambda/4$) according to the impedance transformation

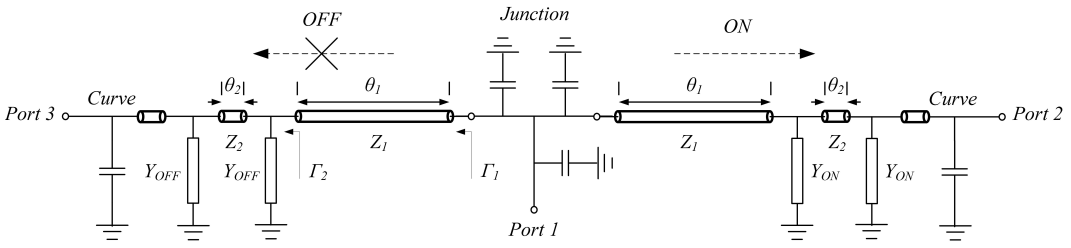

Figure 2.7: Equivalent circuit representation of BB type SPDT switch

under ideal conditions [Pozar, 2005]. Practically, starting from a quarter wavelength, θ_1 is adjusted by full-wave EM optimization. As aforementioned, RF MEMS switches and air bridges on Y-junction/curves are modeled as the stack of layers to use 2.5D ADS Momentum solvers [Keysight Technologies, 2009].

The switch has been fabricated by FBK and measured by CNR (Consiglio Nazionale delle Ricerche) - Institute for Microelectronics and Microsystems, Roma, Italy. Wafer probes (G-S-G type) are 50 Ω matched and calibrated by a SOLT (Short, Open, Load, and Thru) calibration technique. Figure 2.8 shows the comparison between designed and measured results. Measured results correspond well with the simulation. The discrepancy on IL seems to be due to the wafer probe contact resistance. The RL is below -15 dB at the design frequency. The isolation is also in line with the simulation. There are local isolation spec violations at Ku band where the isolation is worse than 50 dB. Those could be explained by wafer probe coupling or substrate mode propagation.

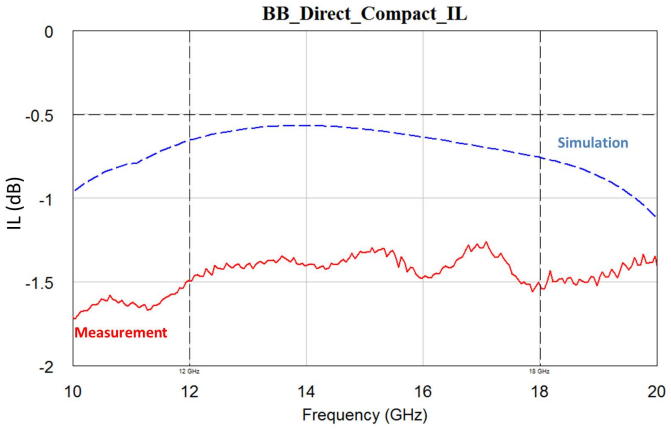

(a) IL

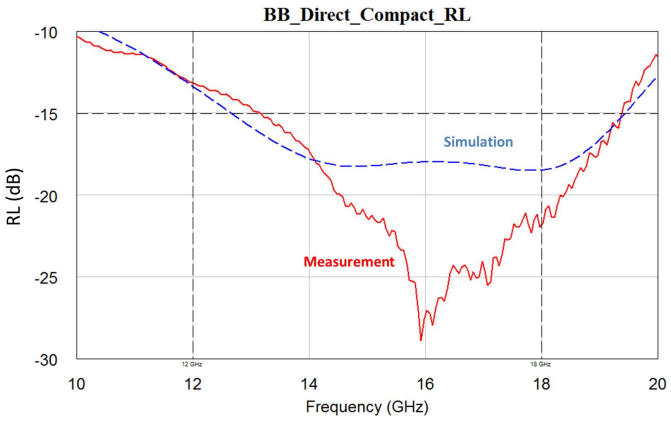

(b) RL

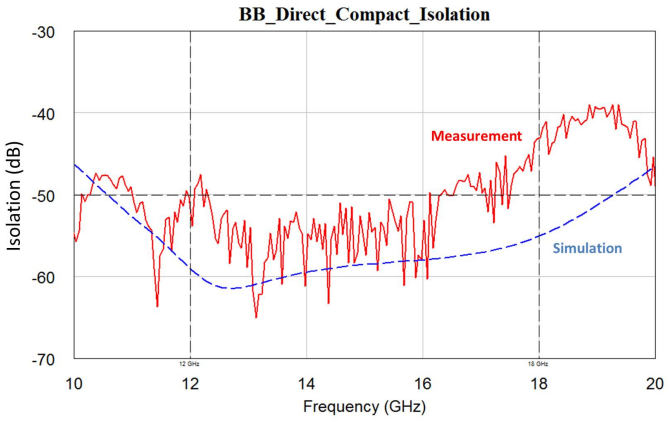

(c) Isolation

Figure 2.8: Measured performance of the BB SPDT switch shown in Figure 2.6

2.2.3 BB_Opt_T (Capacitive Shunt + Line + Capacitive Shunt)

A BB_Opt_T type SPDT switch consists of two switching paths and a single T junction. Each switching path has two capacitance shunt switches which are distanced. Figure 2.9 and Figure 2.10 describes a fabricated BB_Opt_T type SPDT switch and its equivalent circuit representation. θ_1, θ_2 are the electrical lengths of the lines between the switches and the junction. Z_1 and Z_2 are line impedances. Y_{ON} and Y_{OFF} represent corresponding shunt reactive components as shown in Eq.(2.1) and Eq.(2.2).

As BB type switches, the BB_Opt_T type SPDT switch has two cascading switches. But they are distanced by a certain length (θ_2). The BB_Opt_T type SPDT's lateral size is larger than the size of BB type switches, which makes the IL worse due to the loss from the θ_2 long transmission line. The θ_2 long midline is inserted to improve the

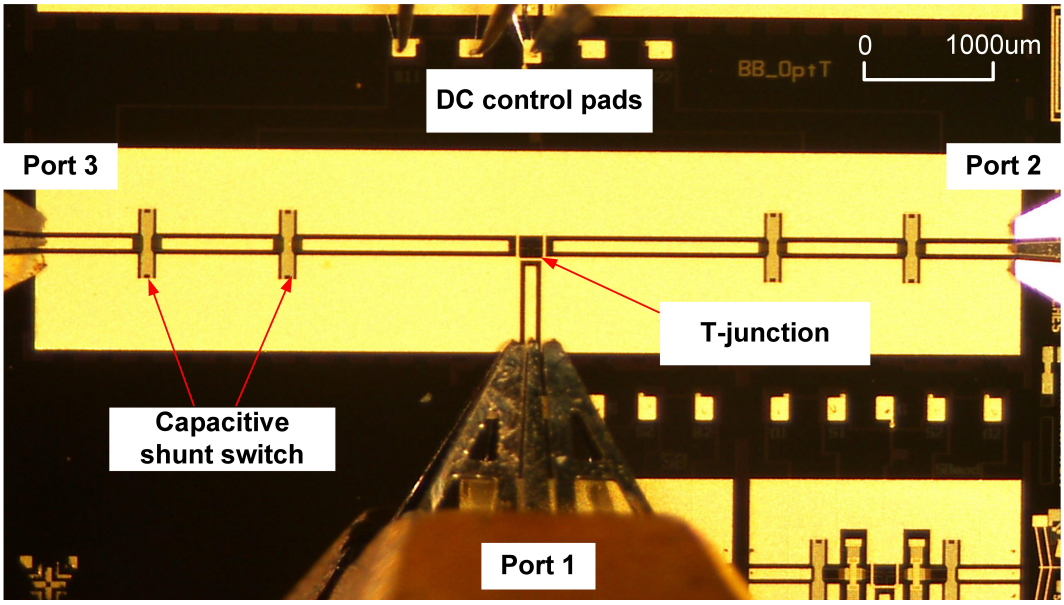

Figure 2.9: BB_Opt_T type SPDT switch [TUM et al., 2012]

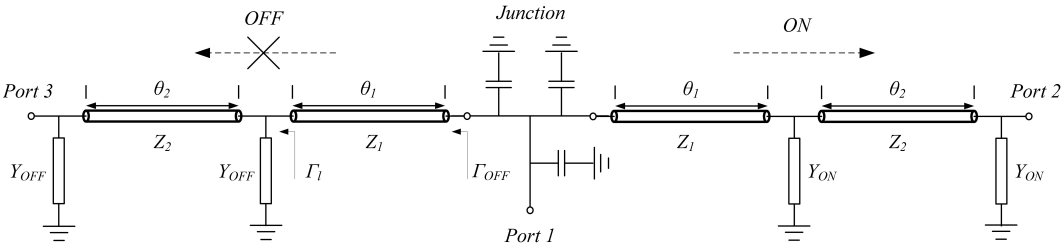

Figure 2.10: Equivalent circuit representation of BB_Opt_T type SPDT switch

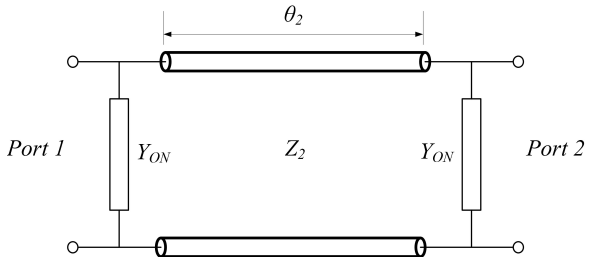

Figure 2.11: Equivalent circuit representation of the double switching transmission line

RL. There are two conditions to get a good RL. First, the OFF path should be well isolated from the ON path, which is mainly done by θ_1 long transmission lines. Second, the reflected signal from the ON path itself should be small. The reflections mainly come from the discontinuities. These discontinuities also include ON-state capacitive shunt switches. Even though their bridges are up, some reactive portions contribute due to the small capacitance between lines and bridges, which makes a signal reflection. The θ_2 long midline is designed such that the reflected waves (from the first and second switches) are destructively superpositioned as much as possible. Figure 2.11 shows an equivalent circuit representation of the double RF MEMS switching transmission line where the switches are distanced by θ_2.

The lumped element circuit in Figure 2.11 is analyzed by ABCD parameters as

$$\begin{bmatrix} A & B \\ C & D \end{bmatrix}_{ON} = \begin{bmatrix} 1 & 0 \\ Y_{ON} & 1 \end{bmatrix} \begin{bmatrix} \cos\theta_2 & Z_2 \sin\theta_2 \\ Y_2 \sin\theta_2 & \cos\theta_2 \end{bmatrix} \begin{bmatrix} 1 & 0 \\ Y_{ON} & 1 \end{bmatrix}. \tag{2.3}$$

θ_2 is the electrical length and Y_{ON} is the bridge susceptance. Y_2 is $1/Z_2$ and $Y_0 = 1/Z_0$. By Eq.(2.1), Eq.(2.3) together with an ABCD-S parameter transformation, S_{11} is calculated as

$$S_{11} = \frac{jZ_2\left[\{Y_0 - Z_0(Y_2^2 - \omega_0 C_{up}^2)\}\sin\theta_2 - 2\omega_0 C_{up} Y_2 Z_0 \cos\theta_2\right]}{2\cos\theta_2 + j\{Z_2(Y_0 + Z_0 Y_2^2 - 2\omega_0 C_{up} - Z_0\omega_0^2 C_{up}^2)\sin\theta_2 + 2Z_0\omega_0 C_{up}\cos\theta_2\}}. \tag{2.4}$$

A small bridge resistance, an inductance and a DC line contribution are neglected ($Y_{ON} = j\omega_0 C_{up}$). ω_0 is the shunt resonant frequency which is based on Ku band center frequency. To minimize S_{11}, the numerator of Eq.(2.4) should be 0. This also means no reflection. This condition is fulfilled when

$$\theta_2 = \tan^{-1}\frac{2C_{up}\omega_0 Z_2 Z_0^2}{Z_2^2 - Z_0^2 + (C_{up}\omega_0 Z_2 Z_0)^2}. \tag{2.5}$$

Eq.(2.5) says the optimum θ_2 is given by the bridge upstate capacitance (C_{up}) and line impedance (Z_2). Since all line impedances are Z_0 ($Z_2 = Z_0 = 50\,\Omega$), Eq.(2.5) can be

reformulated as

$$\theta_2 = \tan^{-1} \frac{2}{C_{up}\omega_0 Z_0}. \tag{2.6}$$

Because the bridge upstate shunt capacitance C_{up} is given by the switch RF characteristics, θ_2 is determined by the center frequency ω_0.

Practically, the optimum $\theta_2|_{opt}$ of the BB_Opt_T SPDT switch is different from the θ_2 in Eq.(2.6) because Eq.(2.3)-Eq.(2.6) do not account for the RF contributions of the junction and the bridge resistance/inductance. Therefore, starting from the calculated θ_2 in 2.6, a full-wave optimization should be carried out. Additionally, what is worthy of remark is, Eq.(2.5) says that the midline length θ_2 can be decreased by using an increased Z_2 higher than Z_0. This means, it is possible to design a more compact SPDT switch by using high impedance lines [Atwater, 1985; Muldavin and Rebeiz, 2000].

θ_1 is determined by a similar process to the BB type switch OFF state analysis. At the junction, the OFF path should be opened. Hence, the distance between the junction and the switch is chosen as a quarter wavelength of the guided wave. Full-wave simulations using ADS Momentum have been used for the fine tuning [Keysight Technologies, 2009].

Figure 2.12 depicts the comparison between simulation and measured results of the BB_Opt_T type SPDT switch. Due to the reflected signal cancellation by θ_{2opt} spacing, the RL of the BB_Opt_T is better than the BB type's. However, the isolation is worse because the grounding at the quarter wavelength ($\theta_1 = 90°$) is not as good as BB type. The difference between simulated IL and measured IL is mainly due to the contact resistance which is not considered in the EM simulation.

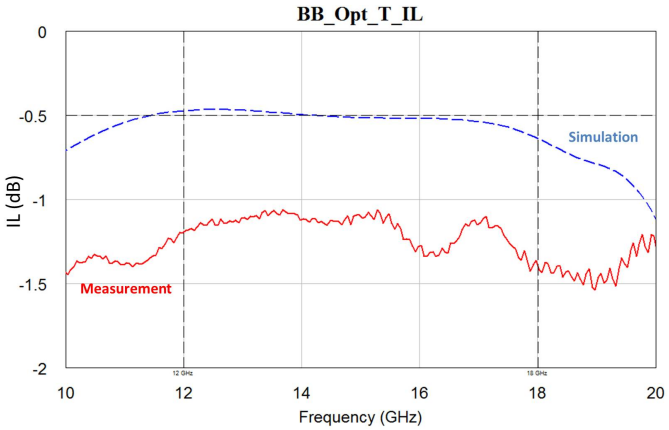

(a) IL

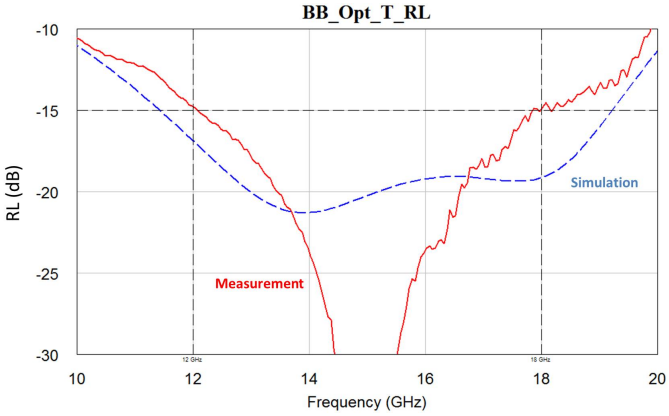

(b) RL

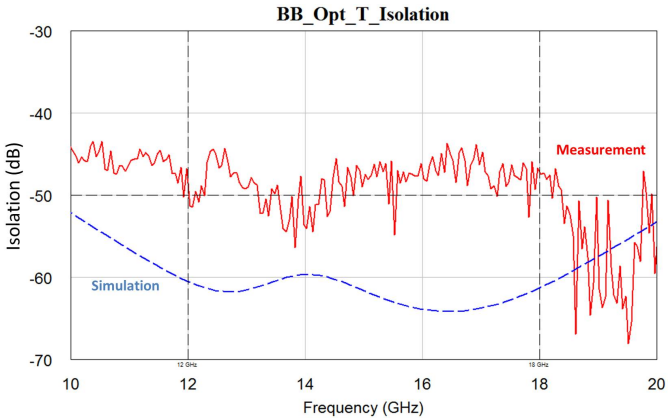

(c) Isolation

Figure 2.12: Measured performance of the BB_Opt_T SPDT switch shown in Figure 2.9

2.2.4 SB (Ohmic Series + Capacitive Shunt)

In the SB type SPDT switch, Ohmic series switches are directly connected to the capacitive shunt switches. Figure 2.13 and Figure 2.14 show an SB type SPDT switch and a lumped element representation of Ohmic series switches. When the bridge is down, the switch is ON by direct Ohmic contacts. Due to the Ohmic contact resistance, the ON state IL is normally worse than the capacitive type's. When the bridge is up, the switch becomes OFF. Compared to the capacitive type, the Ohmic series switch generally has a broadband OFF-state isolation. However, the isolation is not as good as of the capacitive type due to the capacitances C_1, C_2.

The SB type SPDT switch combines the characteristics of the capacitive shunt switch and the Ohmic series switches. Compared to the other types, the SB type SPDT switch

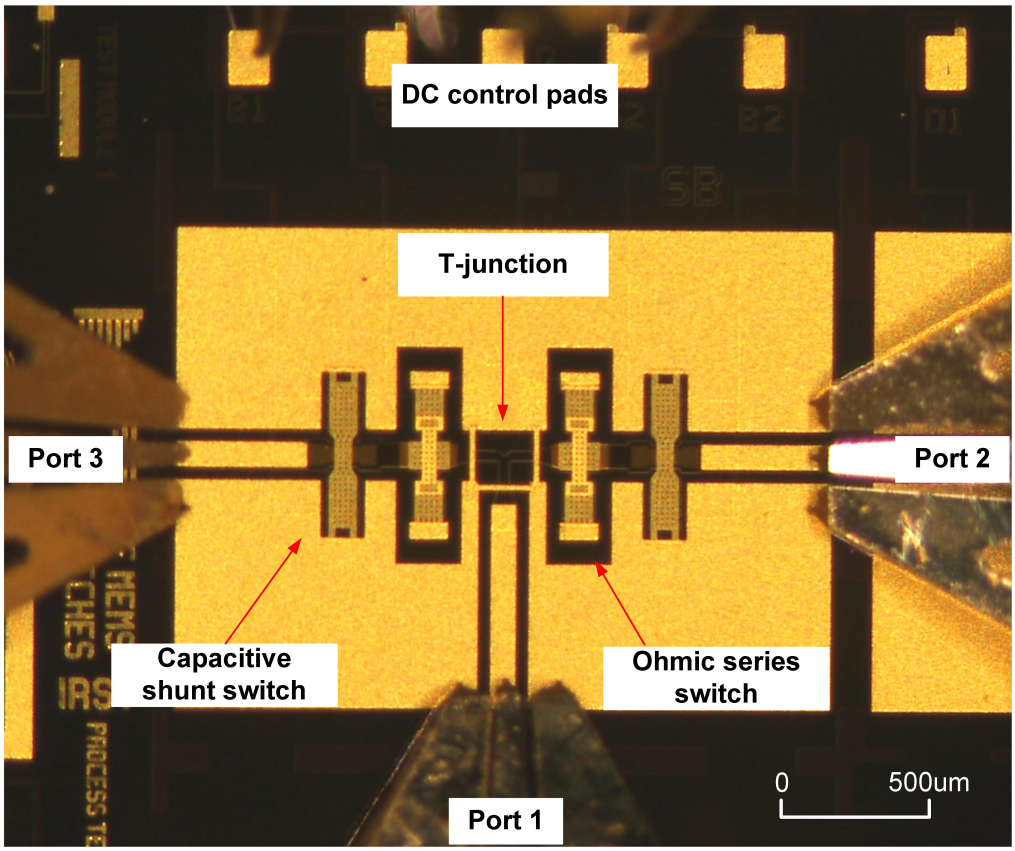

Figure 2.13: SB type SPDT switch [TUM et al., 2012]

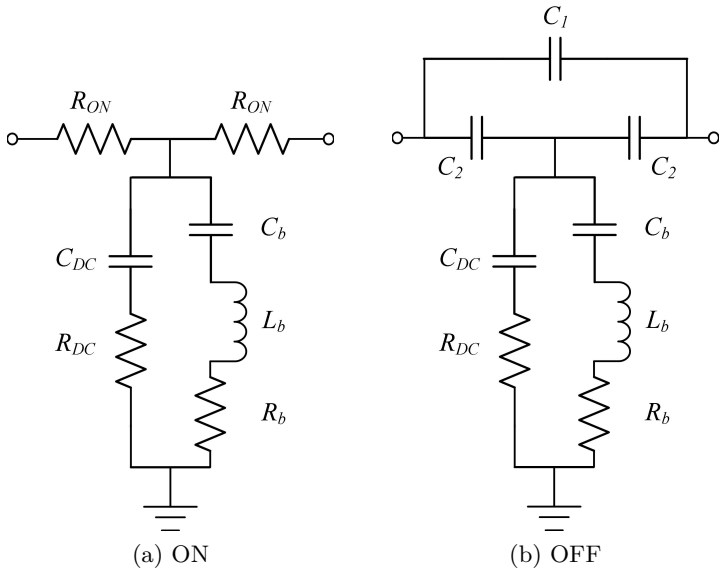

(a) ON (b) OFF

Figure 2.14: Equivalent circuit representation of the Ohmic Series switch

is compact and suitable to be accommodated on a limited area. Figure 2.15 shows the measured result of the SB type switch. The simulations and measurements show a good agreement. Due to the nature of the Ohmic series switch, the SB type SPDT switch is broadband, but the isolation is worse compared to the BB type switch employing two capacitive shunt switches.

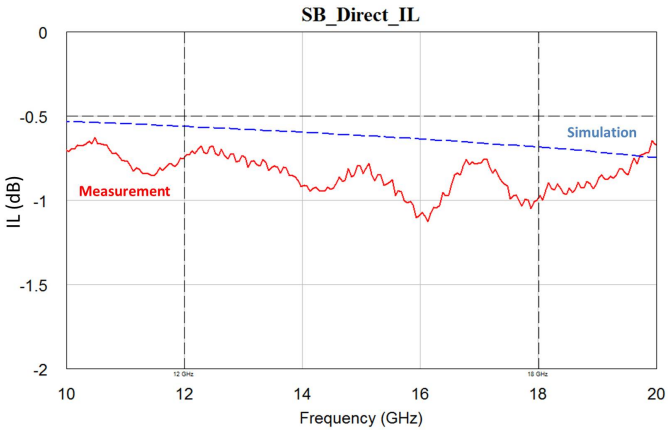

(a) IL

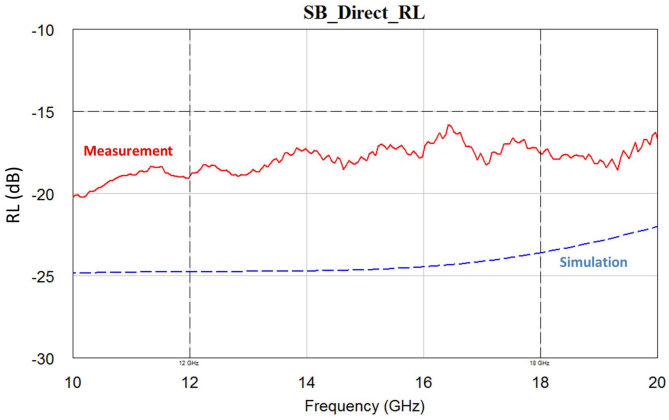

(b) RL

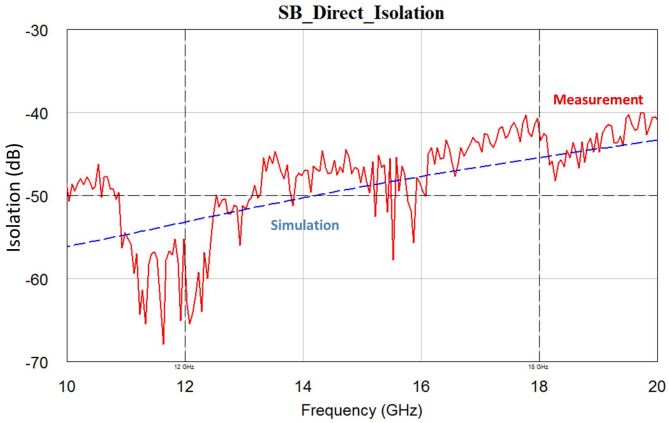

(c) Isolation

Figure 2.15: Measured performance of the SB SPDT switch shown in Figure 2.13

2.2.5 SBO (Ohmic Series + Ohmic Shunt)

Figure 2.16 and Figure 2.17 show a SBO type SPDT switch and its equivalent circuit representation. An SBO type SPDT switch uses Ohmic shunt switches. The feature of the Ohmic shunt switch is similar to the capacitive shunt switch. The difference is that the Ohmic series switch does not have a dielectric layer between the CPW center line and the bridge. Figure 2.18 shows the equivalent circuit representation of the Ohmic shunt switch. The switch uses an Ohmic shunt grounding for the signal rejection. Because the contact resistance $R_{contact}$ is much higher than the bridge resistance R_b, the grounding is not as good as the capacitive shunt switch's, which makes the isolation worse. However, since it does not use a shunt resonance, the signal is rejected for a broader frequency band.

The SBO type switch consists of Ohmic series switches and Ohmic shunt switches. Figure 2.17 describes the equivalent circuit representation. Y_{shON} and Y_{shOFF} are the

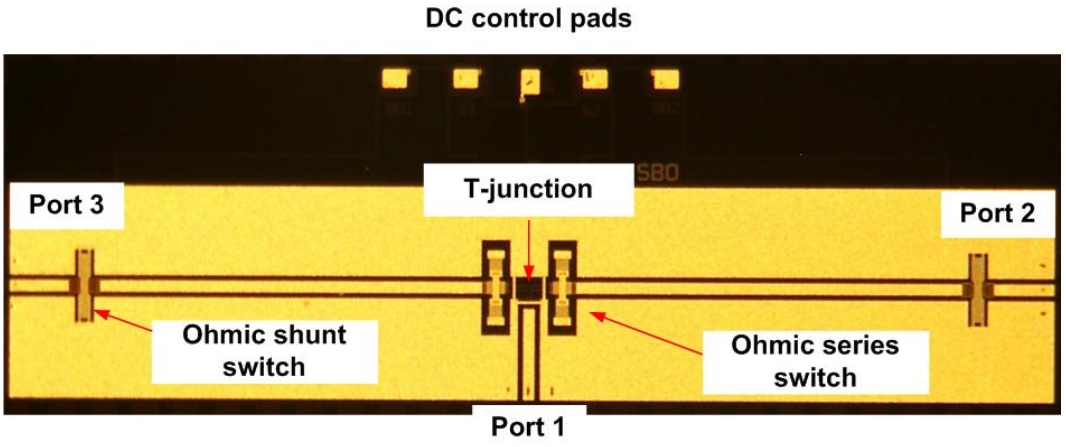

Figure 2.16: SBO type SPDT switch [TUM et al., 2012]

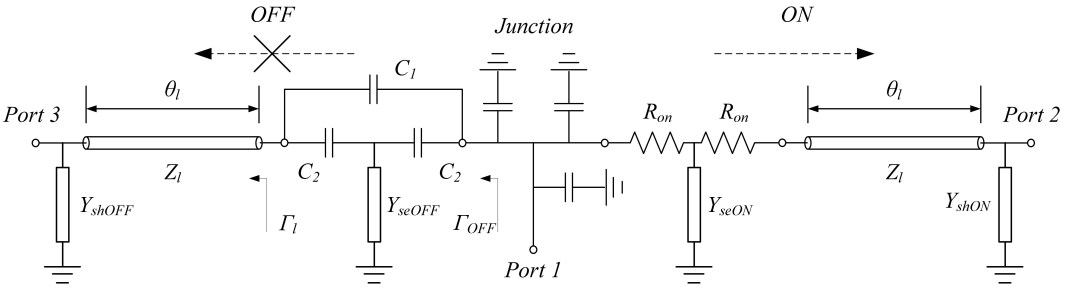

Figure 2.17: Equivalent circuit representation of SBO type SPDT switch

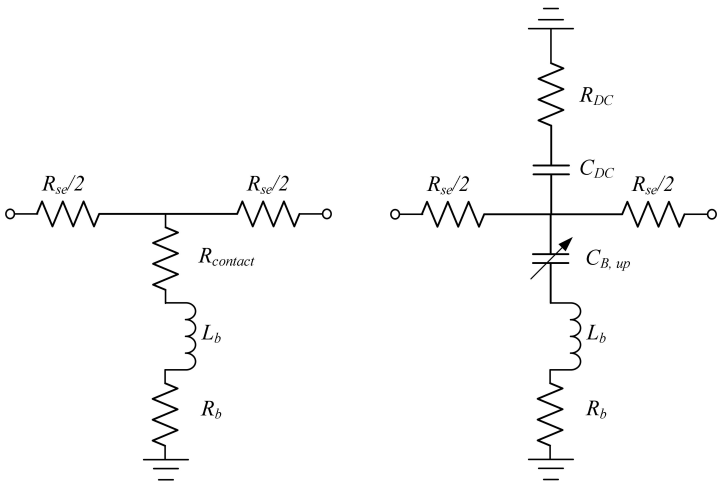

Figure 2.18: Equivalent circuit representation of the Ohmic Shunt switch

shunt admittances of the ON/OFF Ohmic shunt switches. Y_{seON}, Y_{seOFF} are the corresponding shunt admittances of the ON/OFF Ohmic series switches. An R_{ON} is the Ohmic contact resistance. As depicted in Figure 2.16, the Ohmic series switches are located right after a T-junction and shunt switches are distanced by a certain length θ_l. The ABCD matrix of the ON branch is given as

$$\begin{bmatrix} A & B \\ C & D \end{bmatrix}_{ON} = \begin{bmatrix} 1 & 0 \\ Y_j & 1 \end{bmatrix} \begin{bmatrix} 1 + R_{ON}Y_{seON} & 2R_{ON} + R_{ON}^2 Y_{seON} \\ Y_{seON} & 1 + R_{ON}Y_{seON} \end{bmatrix} \begin{bmatrix} \cos\theta_l & Z_l \sin\theta_l \\ Y_l \sin\theta_l & \cos\theta_l \end{bmatrix} \begin{bmatrix} 1 & 0 \\ Y_{shON} & 1 \end{bmatrix}. \tag{2.7}$$

The parameters R_{ON}, Y_{seON} and Y_{shON} are given switch characteristics. The RL (S_{11}) on the ON path is calculated from Eq.(2.7) by the ABCD - S parameter transformation [Pozar, 2005]. Figure 2.19(a) shows an $|S_{11}|$ variance according to θ_l. It is investigated that the θ_l should be 72° to minimize the RL.

On the other hand, the OFF path should be opened to the ON path, which means the $\angle\Gamma_{OFF}$ must be 0° in Figure 2.17. In BB type switches, the first shunt switches are distanced by a quarter wavelength from the junction and this fulfills $\angle\Gamma_{OFF} = 0°$. However, in the SBO type switch, the OFF path is already opened by Ohmic series switches at the junction. However, due to the contribution of C_1 and C_2, the path is not fully opened and θ_l and Ohmic shunt switches also contribute the signal blocking.

Ignoring the bridge inductance and the shunt capacitance (Y_{seOFF} ignored), the phase

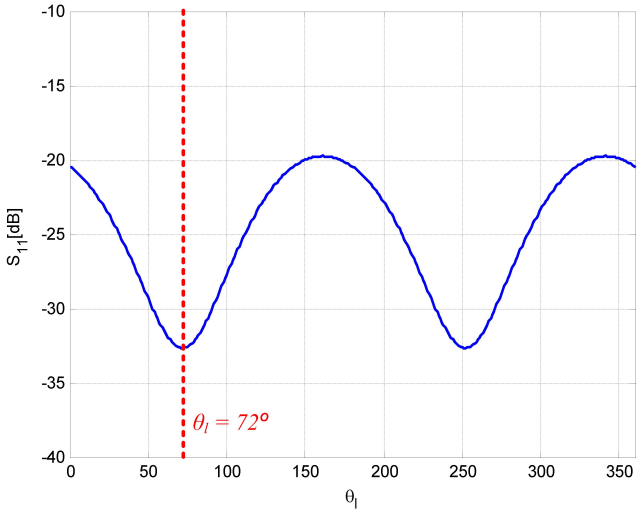

(a) $|S_{11}|$ according to the θ_l variation

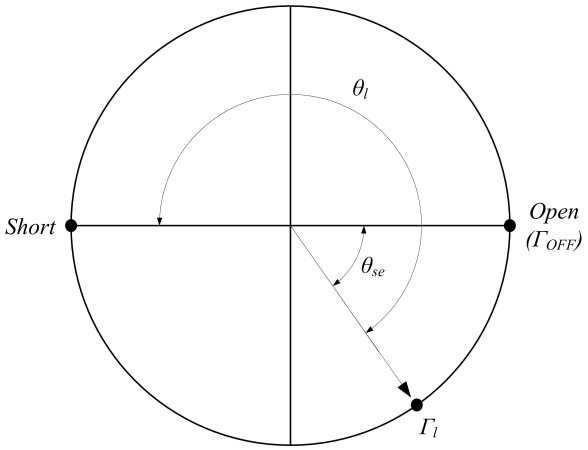

(b) Phase analysis in the smith chart

Figure 2.19: SBO switch ON/OFF branch analysis

difference between Γ_{OFF} and Γ_l is calculated as

$$\theta_{se} = \angle\Gamma_l - \angle\Gamma_{OFF} = tan^{-1}\frac{1}{\omega Z_0(2C_1 + C_2)}. \tag{2.8}$$

This advanced phase(θ_{se}) should be accounted as an additional electrical length. Therefore, θ_l should be $\theta_{se} + 90°$ (see Figure 2.19(b)).

However, according to the ON branch analysis, θ_l should be 72° for best RL, which is less than $\lambda/4$. This means, a compromise between RL and isolation should be made. In this work, θ_l is optimized to achieve a good isolation, which makes θ_l be larger than 90°.

Figure 2.20 shows the measured RF performance of the switch and the comparison to the ADS momentum simulation [Keysight Technologies, 2009]. Some discrepancies are investigated. The possible reason is the modeling error of the contact resistance of the Ohmic switch. In an SBO type SPDT switch, the Ohmic contact resistance ($R_{contact}$) affects the isolation as well as the IL, since an Ohmic shunt grounding is used for rejecting a signal. If the isolation in the OFF path is degraded, the RL also suffers as shown in Figure 2.20.

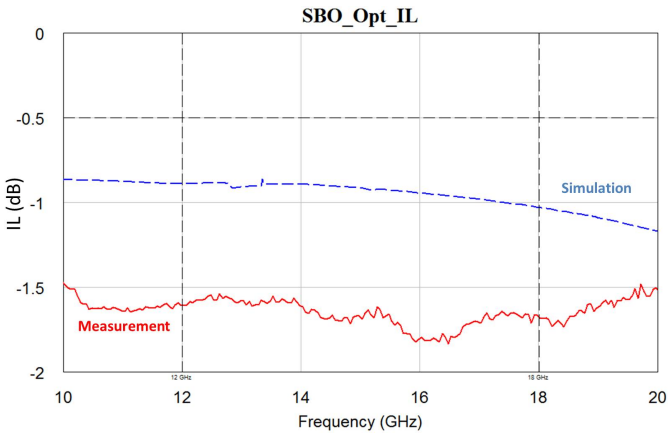

(a) IL

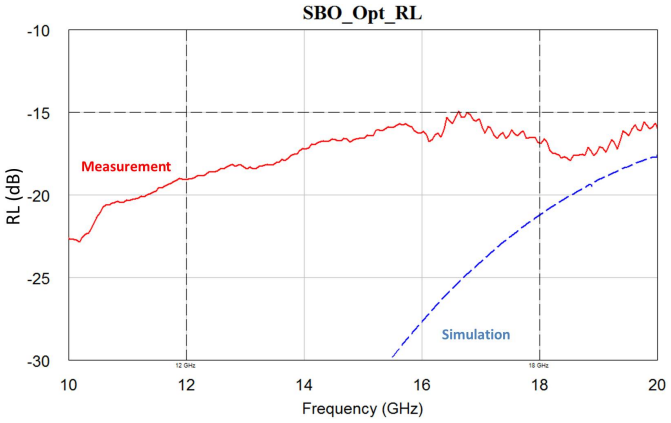

(b) RL

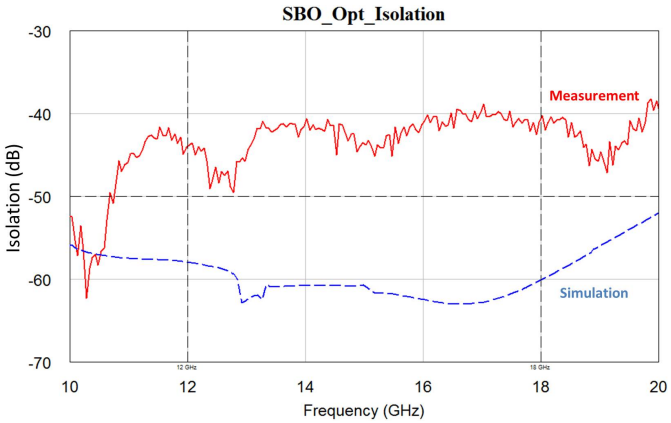

(c) Isolation

Figure 2.20: Measured performance of the SBO SPDT switch shown in Figure 2.16

2.2.6 CC (Ohmic Series + Ohmic Series)

Satellite redundancy switches have to be highly reliable. They work only very few times during a satellite lifetime. However, they should be sure to work when a redundancy unit needs a switch-over. One of the major concerns of the RF MEMS switch is the long term contact failure. Since the switch stays on the same state (Main ON or Backup ON) for a long time, it may happen that the switch is not successfully switched over. This long term failure has been a serious issue and many long term switch failure mechanisms have been reported, such as the bridge/cantilever stiction by a charge accumulation or a metal-to-metal micro welding, etc. To overcome these issues, many researches have been done by changing contact areas, materials or increasing the restoring force, etc [Spengen, 2012; Kim et al., 2013a; Ishida et al., 2013; Kwon et al., 2007; Rebeiz et al., 2013].

A CC type SPDT switch adopts a new approach. Figure 2.21 shows the CC type SPDT switch. In the CC type SPDT switch, cantilever type Ohmic series switches are used, since they are compact and more suitable to be accommodated on the limited area. The CC type SPDT switch consists of a 1-to-4 junction and double sub paths (Path 1,

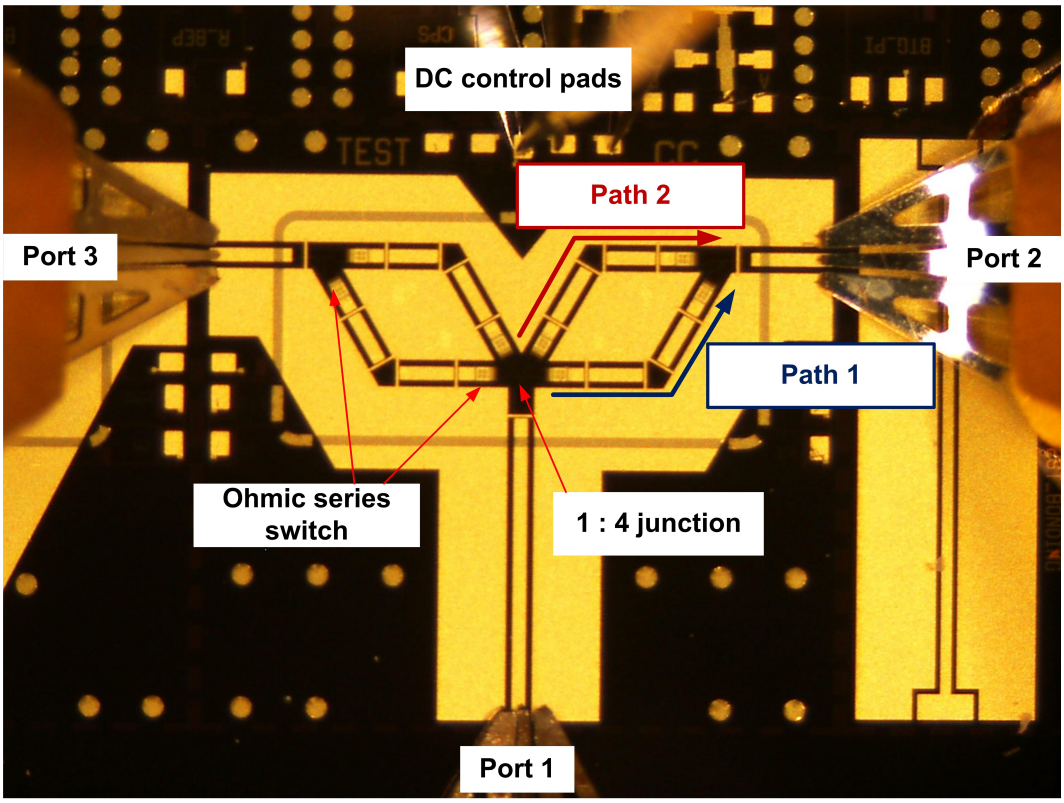

Figure 2.21: CC type SPDT switch [TUM et al., 2012]

Path 2) on each path (main, backup). The sub paths are regularly toggled to avoid a long term contact. In other words, the CC type SPDT switch is potentially free from long term contact failure. However, it has more complicated signal paths. Moreover, CC type SPDT switches can be used for the limited cases in which a periodic downtime is allowed for a subpath toggling. This periodic downtime should also account for the setting of the switching components. Since the cantilever switch closing time is faster than the opening time, there is a state in which Path 1 and Path 2 are simultaneously connected. In this case, the system could be broken due to high impedance mismatch. This means, the system should be down during a switch settling.

Figure 2.22 and Figure 2.23 show the CC type SPDT switch measurements for Path 1 and Path 2.

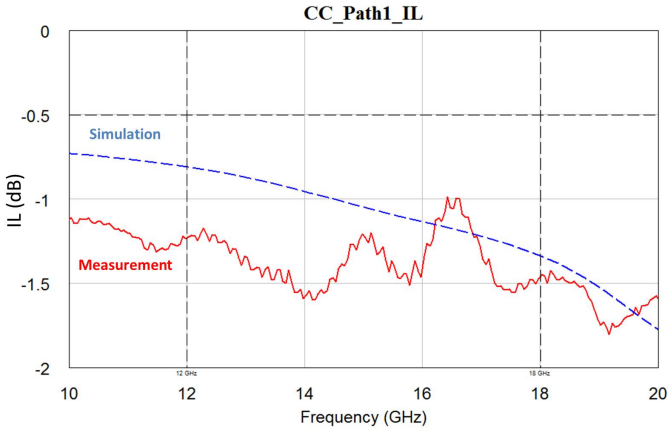

(a) IL

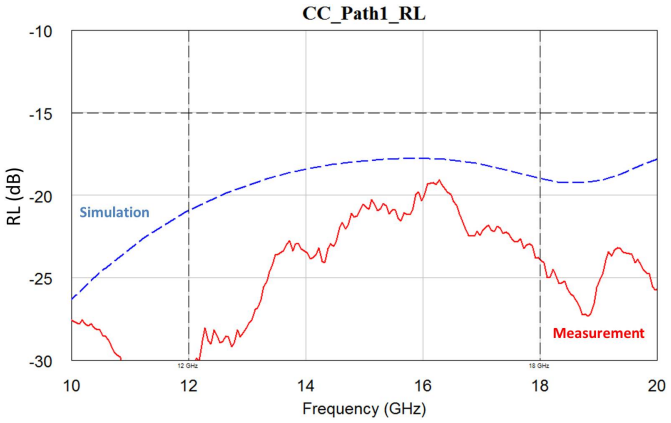

(b) RL

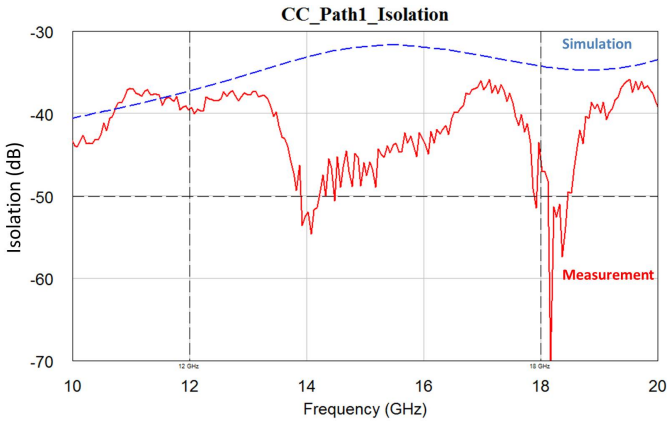

(c) Isolation

Figure 2.22: Measured performance of the CC type SPDT switch (shown in Figure 2.21) for Path 1

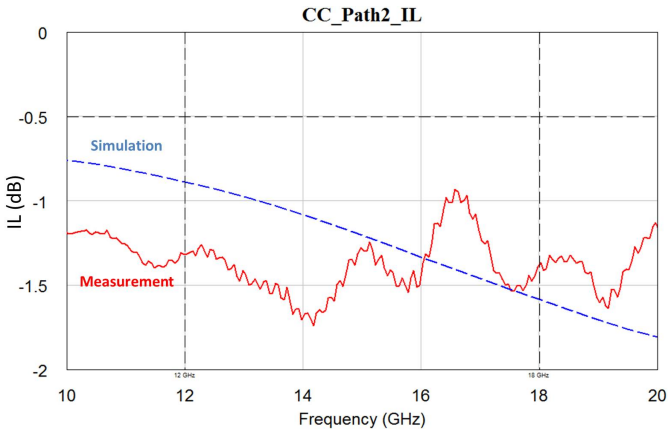

(a) IL

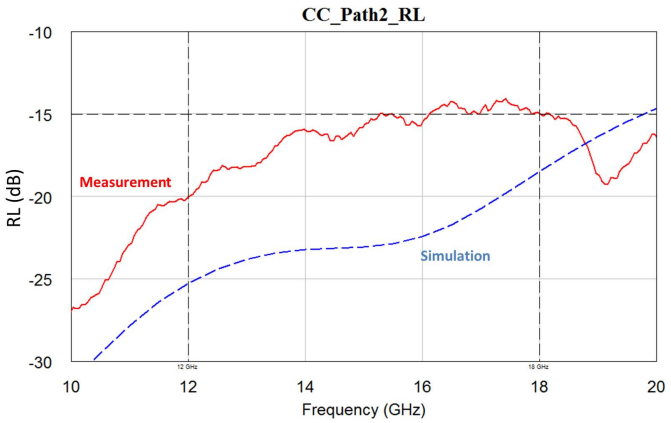

(b) RL

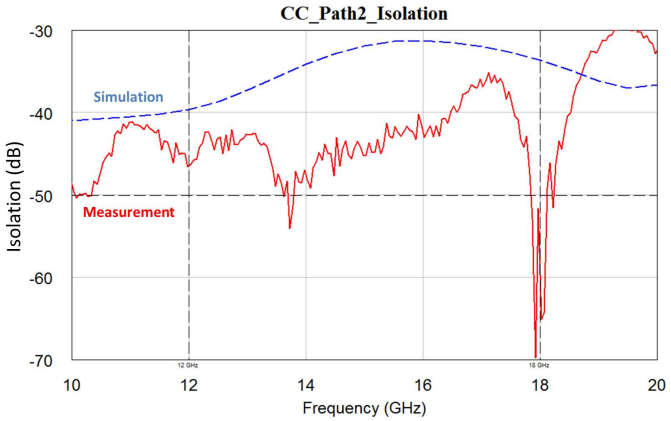

(c) Isolation

Figure 2.23: Measured performance of the CC type SPDT switch (shown in Figure 2.21) for Path 2

2.3 Package for environmental test

All components used in space applications have to be tested under the harsh space environment, such as a severe shock and vibration or a rapid temperature change, etc. The package depicted in Figure 2.24 is to test BB, SB and CC type SPDT switches under space environments. It has been designed by TUM and fabricated by Thales Alenia Space, Rome. The package has been designed based on an LTCC (Low Temperature Cofired Ceramics) technology. The LTCC is a multi-layer technology which is suitable for high frequency applications. In comparison with the printed resin board, it has good high frequency characteristics with good thermal stability [Imanaka, 2005].

During environmental tests, the SPDT switches are mounted on the center cavity which is surrounded by metal vias and a metal lid covered frame. As described in the figure, the switches are connected through double bondwires. A bondwire compensation structure is to compensate a high inductance of bondwires. All the other parts are optimized to minimize RF discontinuities.

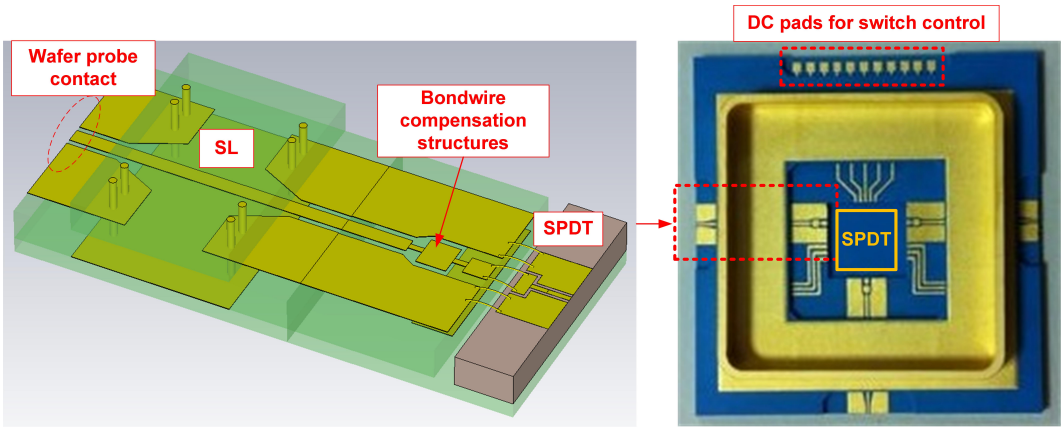

Figure 2.24: LTCC package for environmental test

2.4 Conclusion

In this chapter, five types of SPDT switches have been presented and their performance was demonstrated. Table 2.3 lists the RF performance at Ku band according to the SPDT switch type. The bold letters stand for the best and worst cases at the Ku band center frequency.

In terms of IL, the SB type SPDT switch has the best performance. This is mainly due to its small size. However, all SPDT switches do not meet the given IL specification.

The BB_Opt_T type SPDT switch shows the best RL. As aforementioned, the BB_Opt_T switch is designed in a way that the reflected signals are efficiently canceled out.

The best isolation performance is achieved by the BB type SPDT switch employing double capacitive shunt switches. Considering that the redundancy switch should possess a high isolation, the BB type can be regarded as the best candidate. The CC type SPDT switches also show an acceptable performance. Since they use complicated structures like a 1:4 junction, their RLs are higher than for the others. However, they are still attractive if they are used for other applications which do not require critical RF specifications and allow regular downtimes.

Model	**IL[dB]**	**RL[dB]**	**Isolation[dB]**
BB	-1.324,...,-1.296 (-1.32@15 GHz)	-28.9,...,-13.16 (-21.38@15 GHz)	-65.07,...,-43.14 **(-56.19@15 GHz)**
BB_Opt_T	-1.392,...,-1.062 (-1.101@15 GHz)	-44.86,...,-14.81 **(-44.2@15 GHz)**	-56.39,...,-43.69 (-47.13@15 GHz)
SB	-1.131,...,-0.677 **(-0.816@15 GHz)**	-18.97,...,-15.84 (-17.95@15 GHz)	-65.5,...,-40.33 (-47.69@15 GHz)
SBO	-1.836,...,-1.539 **(-1.679@15 GHz)**	-19.08,...,-14.95 (-16.58@15 GHz)	-49.6,...,-38.86 **(-43.66@15 GHz)**
CC (Path 1)	-1.6,...,-0.987 (-1.215@15 GHz)	-31.08,...,-19.11 (-20.61@15 GHz)	-54.63,...,-35.88 (-46.65@15 GHz)
CC (Path 2)	-1.742,...,-0.931 (-1.285@15 GHz)	-20.04,...,-14.08 **(-15.73@15 GHz)**	-69.75,...,-35.18 (-45.19@15 GHz)

Table 2.3: SPDT switch performance comparison at Ku band

3 RF MEMS Switching Matrices

3.1 Introduction

In a communication satellite, switch matrices are used to deliver the received signals to the assigned outputs. They provide a full and high connectivity to the satellite broadcasting system. Until now, electromechanical switches have been used due to the high reliability and the low loss signal delivery capability. They are also able to deliver a high power signal with high linearity. However, the electromechanical switches are slow, heavy, bulky and need additional switching motors. These drawbacks cause the necessity of developing novel devices to replace them.

Solid state switches, such as PIN diodes, MESFETs (MEtal Semiconductor Field Effect Transistors) or HEMTs (High Electron Mobility Transistor), are attractive candidates. They are fast and cheap. Moreover, they can be integrated on small areas. Their compact size and light weight gain more interest for space applications. However, they generally not only consume DC power but also may generate intermodulation spurious modes. Their applicable frequency bands are limited as well.

RF MEMS technology for the switch matrices is an attractive solution. As discussed in Chapter 1, RF MEMS switches are small and virtually consume no power in case of electrostatic actuation. Since they are highly linear and less lossy, they can be operated up to microwave frequencies. The cost for RF MEMS fabrication is also going down on maturing microfabrication technologies [DiNardo et al., 2013; De Angelis et al., 2012].

Chapter 3 is dedicated to the design of 12x12 switch matrix using RF MEMS technology. The discussion includes the choice of a network architecture, the physical realization and the corresponding RF circuit design. Starting from the network architecture, the RF design process based on full-wave and circuit simulations is presented. During the development process, a smaller 4x4 switch matrix is designed as a test vehicle to verify the matrix design process.

3.2 High order network by RF MEMS switches

3.2.1 Network topology

A network topology is defined as the arrangement of various components such as nodes, links and peripherals, etc. Network topologies have been mainly investigated in the area of computer architecture and biological networks. In RF networks, they usually stand for a schematic representation of a network which consists of nodes and interconnections. Representative network topologies are Crossbar, Omega, Beneš and Clos network, etc.

An RF MEMS switch network topology should be carefully decided, because the number of required switching elements and stages are different according to the network topology, which determines the construction feasibility, the signal transition quality and the network functionality. In the present work, Beneš and Clos networks have been figured out, since they consist of acceptable numbers of switching elements and can be controlled by a simple control algorithm.

A Beneš network is a powerful rearrangeable network. In a rearrangeable network, any permutation can be statically assigned through the network path rearrangement if necessary. For around 40 years, Beneš networks have been widely used in shared memory-multiprocessor systems, telecommunication networks, TDMA (Time Division Multiple Access) systems for satellite communications and switching fabrics in Internet routers, etc. A Clos network is also a rearrangeable network which consists of two symmetric outside switching stages and an inner stage of nPnT (n-Pole n-Throw) switches. Those three-stage-modules are interconnected with every module in the adjacent stage by a unique link [Yeh and Feng, 1992]. The architecture difference between Beneš and Clos networks is briefly described in Figure 3.1 for 12x12 network.

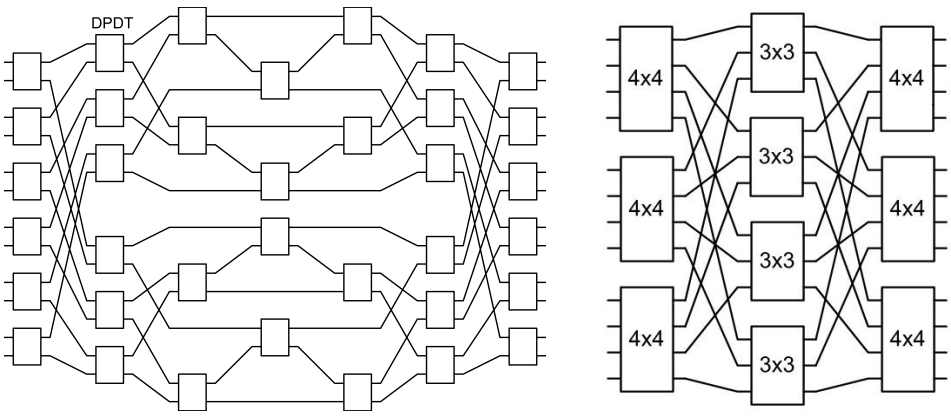

(a) Planar Beneš network (b) 3D Clos Beneš network

Figure 3.1: 12x12 Planar Beneš and 3D Clos Beneš Network [DiNardo et al., 2013]

3.2.2 Network architecture feasibility

Physically, Beneš networks using RF MEMS switches can be constructed in a planar way. Figure 3.1(a) and Figure 3.2(a) show the block diagram and the feasible physical realization of a 12x12 RF MEMS planar Beneš network. It is the simplified form of a 16x16 network [Chang and Melhem, 1997]. Planar Beneš networks use DPDT (Double Pole Double Throw) switches having two inputs and two outputs. Planar Beneš networks are simple, compact and easy to assemble. However, compared to a Clos network, the isolation can be worse because the whole network is packaged by a single housing.

The RF MEMS switch matrix employing the Clos network is physically constructed in a 3D way (see Figure 3.2(b)) and this is a so-called 3D Clos-Beneš network. The 3D Clos-Beneš network consists of small sub-matrices adopting SPnT (Single-Pole n-Throw) or DPDT RF MEMS switches. Those sub-matrices are connected to each other as shown in Figure 3.1(b). In the described 3D Clos-Beneš network, 8 SP4T switches make a single 4x4 switch sub-matrix and 6 SP3T switches do a single 3x3 sub-matrix in the same manner. The inner stage (3x3) is 90° rotated and assembled to the outer stages (4x4) in a 3D way for an easy connection. In terms of isolation, the 3D Clos Beneš network is an attractive solution, since the simple sub-matrix circuitries are separately installed on different metal housings. Moreover, it is easier to be extended to higher order networks. However, the assembly is mechanically complicated because the inner stage should physically be rotated by 90°. In addition to that, the connections to the other stages are achieved by several coaxial cables, which requires high costs and a large footprint together with complex DC control input port connects. The 3D Clos Beneš network is expected to be larger and heavier than the planar Beneš network. Therefore, in this work, it is decided to go on with a planar Beneš network due to its simplicity, smaller footprint and lower weight.

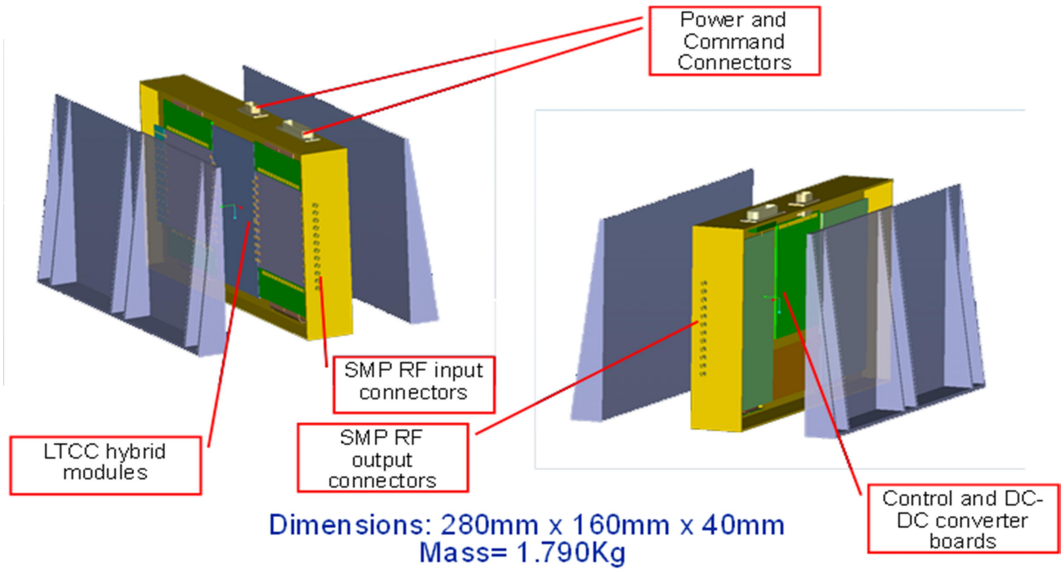

(a) Planar Beneš network

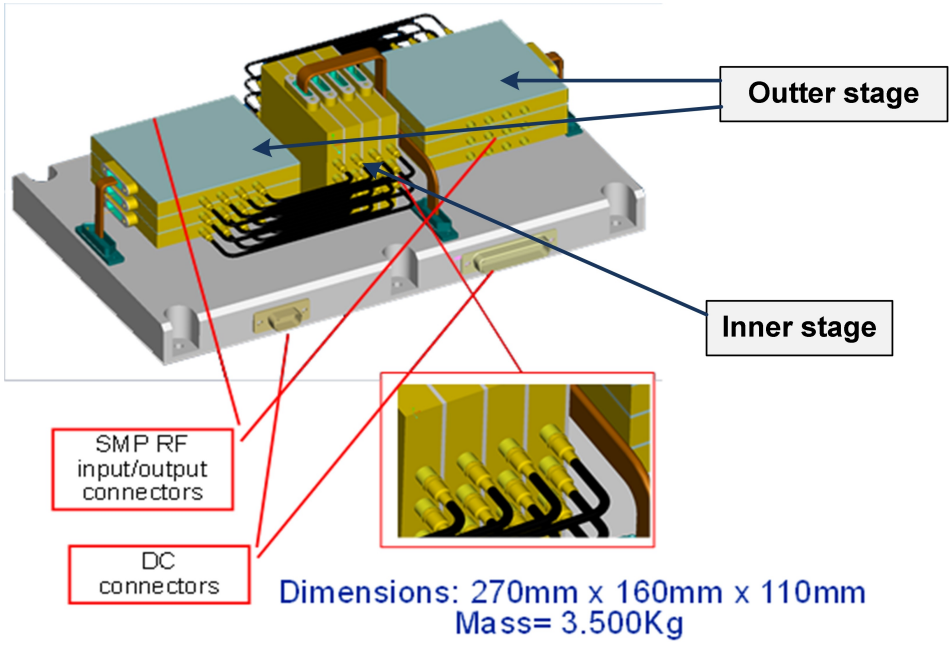

(b) 3D Clos Beneš network

Figure 3.2: Physical realization of 12x12 Planar Beneš and 3D Clos Beneš Network [DiNardo et al., 2013]

3.3 12x12 planar Beneš network

3.3.1 Physical realization

Figure 3.3 and Figure 3.4 describe the physical realization and the unit assembly of the 12x12 RF MEMS planar Beneš network. Since the planar Beneš network needs paths to cross each other, a multi-layered circuit technology is needed. In this work, an LTCC technology is adopted to construct multi-level circuits as shown in Figure 3.5. As drawn in the figure, the RF paths consist of two level connections. In Figure 3.3 and Figure 3.5, 1^{st} level stripline is drawn on blue and 2^{nd} on red.

The current TAS-I LTCC technology allows an 8.4 cm by 8.4 cm board as its maximum

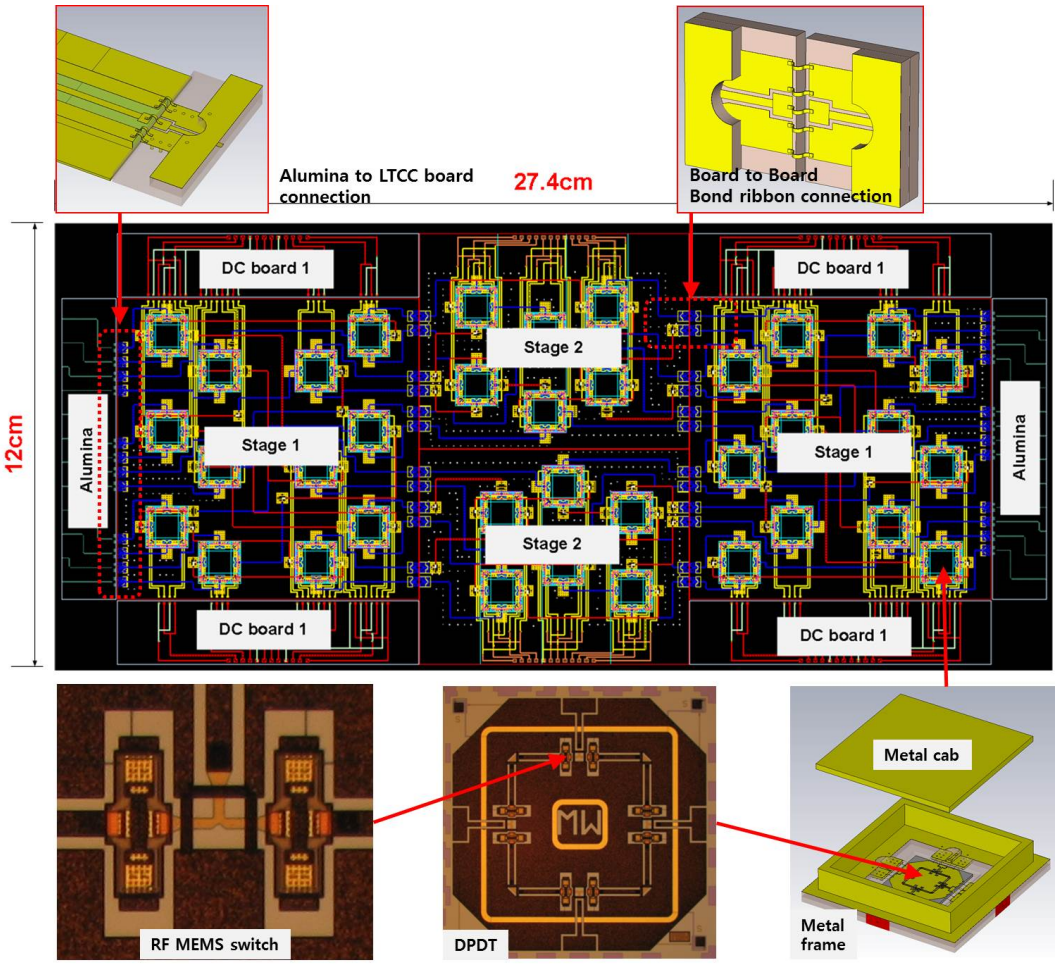

Figure 3.3: Physical realization of the RF MEMS Planar Beneš network

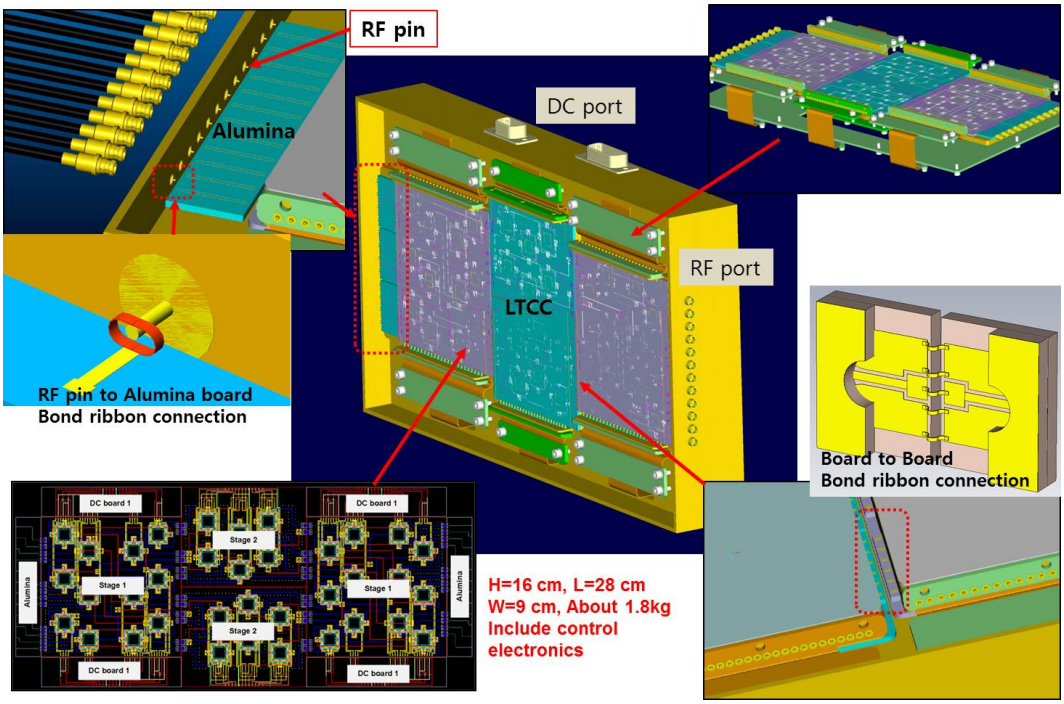

Figure 3.4: Physical assembly of 12x12 switch matrix [DiNardo et al., 2013]

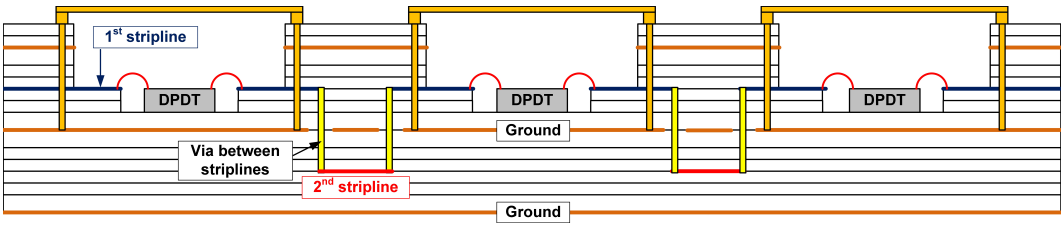

Figure 3.5: Multi-layered circuit using LTCC technology

size. Since it is difficult to build a 12x12 network on a single board, the network must be divided. In this work, the planer Beneš network is divided into 4 sections according to the network symmetry and each section is separately built on a different LTCC board. In Figure 3.3, it is shown that the two 'State 1' and two 'Stage 2' sections are identically designed in each case. This can save design/fabrication effort.

RF signal connections between LTCC boards are done by bond ribbons. The bond ribbon connection is robust and strong against shocks and vibrations compared to the bond wire connection. This is important because the device should survive under a launching condition.

The RF paths on the LTCC board are not directly connected to the RF Input/Output pins. Intermediate paths on the alumina board are inserted between them. This is to avoid physical collisions between LTCC boards and RF pin connectors during the LTCC board mounting.

Fig. 3.6 shows how RF MEMS switches are mounted on the LTCC board. They are mounted deep into the LTCC cavity. The cavity is surrounded by a metal cap, via fences and a ground plane. These shielding structures suppress the coupling between the switches and secure a high EM isolation from the environment. All transitions and discontinuities are optimized to have the desired RF performance, which is further discussed in this chapter [Kim et al., 2009].

In addition to that, the LTCC based planar Beneš network should be packaged together with switch matrix control electronics. The control electronics consist of a digital interface, a power interface, a high voltage driver and ancillary control boards. The digital interface is to deliver control signals to the control board. The high voltage drivers actuate RF MEMS switches according to the control signals. The power interface supplies a control board power and a high DC voltage applied to RF MEMS switches.

The present switch matrix has a 16 cm x 20 cm x 9 cm size and 1.8 kg weight, which is much more compact and light compared to the commercially available 12x12 mechanical

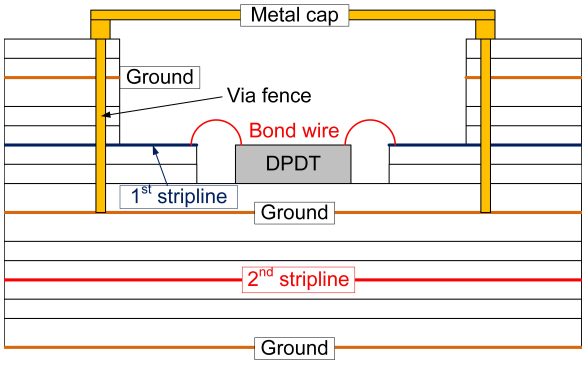

Figure 3.6: DPDT switch mount on LTCC cavity [DiNardo et al., 2013]

Figure 3.7: Commercially available 12x12 Electromechanical RF Switching System [Dowkey, 2013]

switching system. Figure 3.7 shows a commercial mechanical switch matrix system, which has 48.3 cm x 63.5 cm x 17.8 cm size and 38.56 kg weight [Dowkey, 2013]. Even after considering the additional redundant power supply and the local control system, it is much larger and heavier than the proposed 12x12 RF MEMS switch matrix.

3.3.2 Specific RF part design

Table 3.1 shows the proposed specification of the 12x12 switch matrix. The frequency bands are defined based on the commercial broadcasting satellite up/down link standards (L band 1.2-1.8 GHz, S band 2.025-2.3 GHz, C band 3.4-4.2 GHz, Ku band 10.7-12.75 GHz). The input match should be better than -15 dB and the IL lower than 10 dB. The crosstalk between any channels should be lower than -50 dB. Also, the IL of any channel should not differ from the other channel's IL over 1 dB.

Parameter	**Specification**
Frequency band	L, S, C or Ku band
RL	-15 dB max
IL	10 dB max
Crosstalk	-50 dB max
Gain variation	±1 dB

Table 3.1: 12x12 switch matrix RF specification

3.3.2.1 RF MEMS DPDT switch and DPDT-LTCC circuit connection

The switching element of the planar Beneš network is a DPDT switch. Figure 3.8(a) shows a DPDT switch using the RF MEMS technology. It consists of 8 SPST Ohmic series switches. The switch has been designed, fabricated and measured by the University of Perugia, Fondazione Bruno Kessler (FBK) and Consiglio Nazionale delle Ricerche

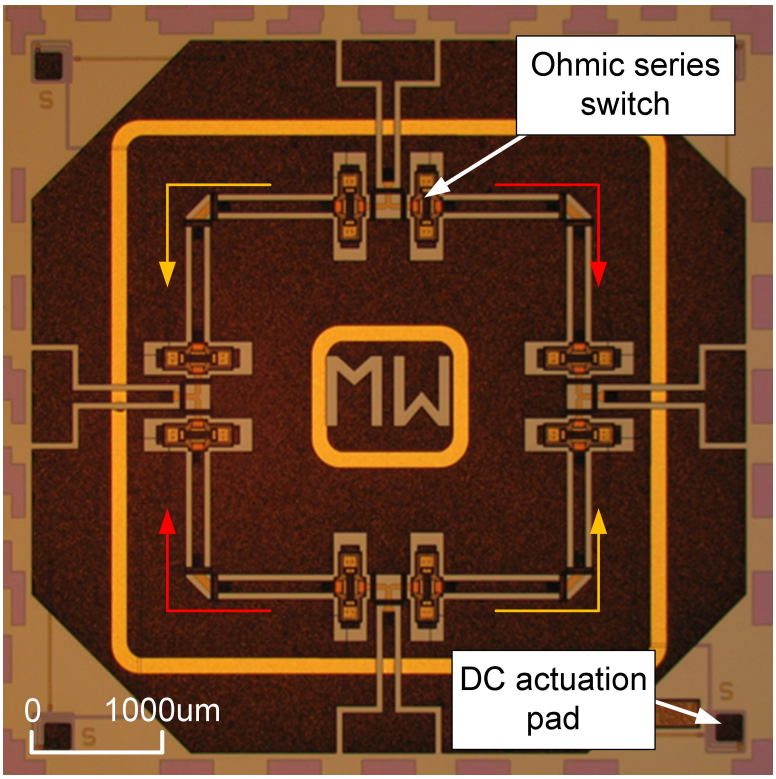

(a) DPDT switch using Ohmic series switches

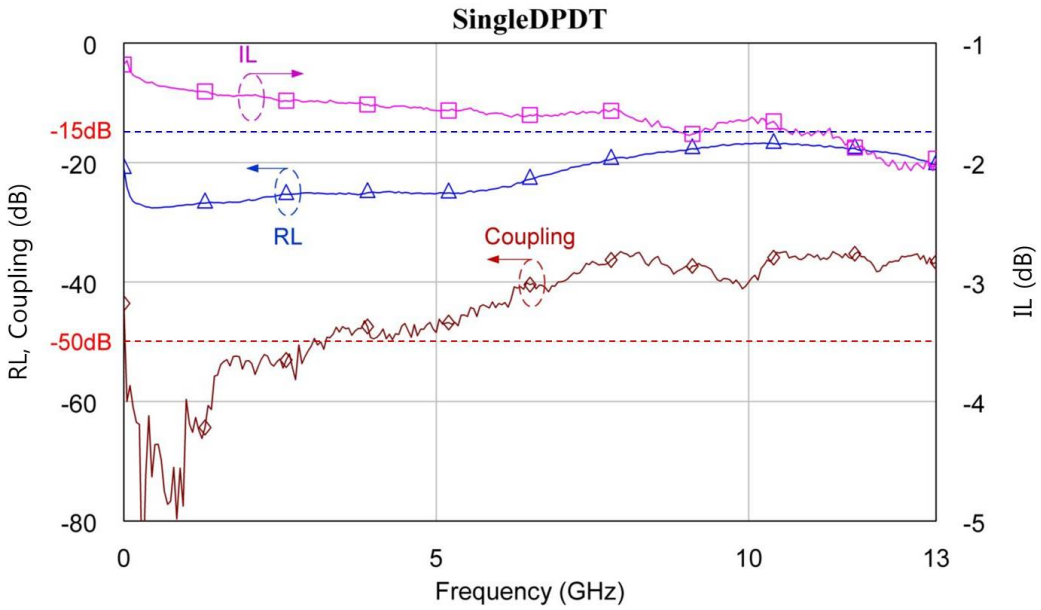

(b) DPDT performance

Figure 3.8: DPDT switch using Ohmic series switches

(CNR). The DPDT switch has a ring structure which routes the two input signals to the desired outputs according to the DC control signals.

As shown in Figure 3.6, the switch and the LTCC circuit are connected by bond wires. Figure 3.9(a) shows the bondwire connection between DPDT switch and LTCC circuit. As shown in the figure, two bond wires are used. Compared to the single one, the double bondwire transition introduces a lower series inductance. However, even though the double bondwire connection is adopted, the series inductance is still remained too high. The excessive series inductance is compensated by shunt capacitive structures. This can be explained by an impedance matching scheme. The transmission line impedance Z is given as

$$Z = \sqrt{\frac{R_{se} + j\omega L_{se}}{G_{sh} + j\omega C_{sh}}}. \tag{3.1}$$

R_{se} and L_{se} are the series resistance and the inductance. G_{sh} and C_{sh} correspond to the shunt conductance and the capacitance. The thin bond wire has a high series inductance which makes L_{se} high and this results in high line impedance Z. When Z is larger than the characteristic line impedance Z_0, a reflection occurs due to the impedance mismatch. The line impedance Z can be decreased by increasing the denominator of Eq.(3.1). The denominator consists of G_{sh} and C_{sh}. Compared to G_{sh}, C_{sh} can be easily increased by broadening of the transmission line. In this work, it corresponds to the center line broadening of the grounded CPW. This can be also discussed as a low-pass filter construction. The series inductance (L_{se}) and the shunt capacitance (C_{sh}) determine a cutoff frequency (ω_c). Below ω_c, the signal passes with low reflection. Figure 3.9(b) shows the simulated compensated RF transition performance, which shows a low-pass filter transition characteristic. The simulation has been done by a transient solver provided in CST MICROWAVE STUDIO [Computer Simulation Technology GmbH, 2010].

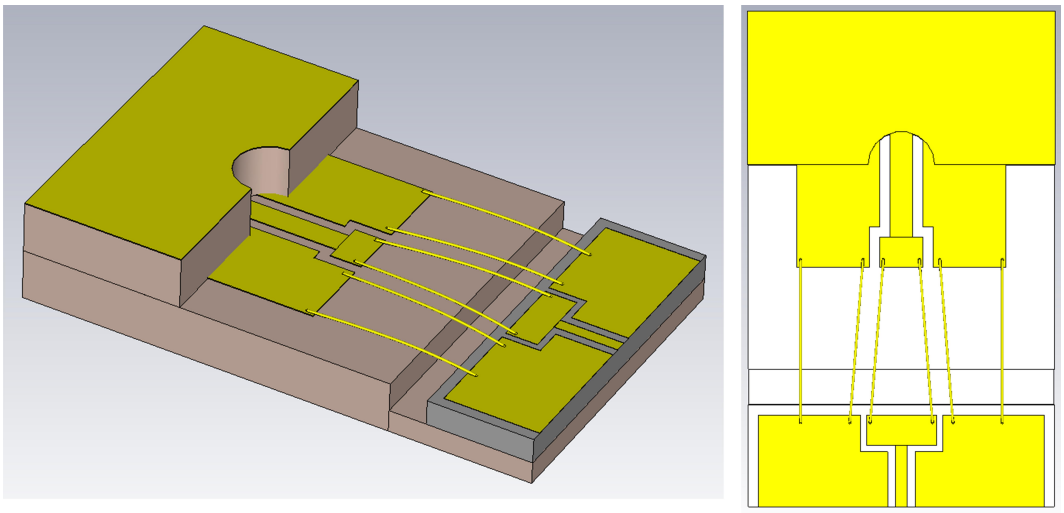

(a) Bondwire connection between switch and LTCC circuit

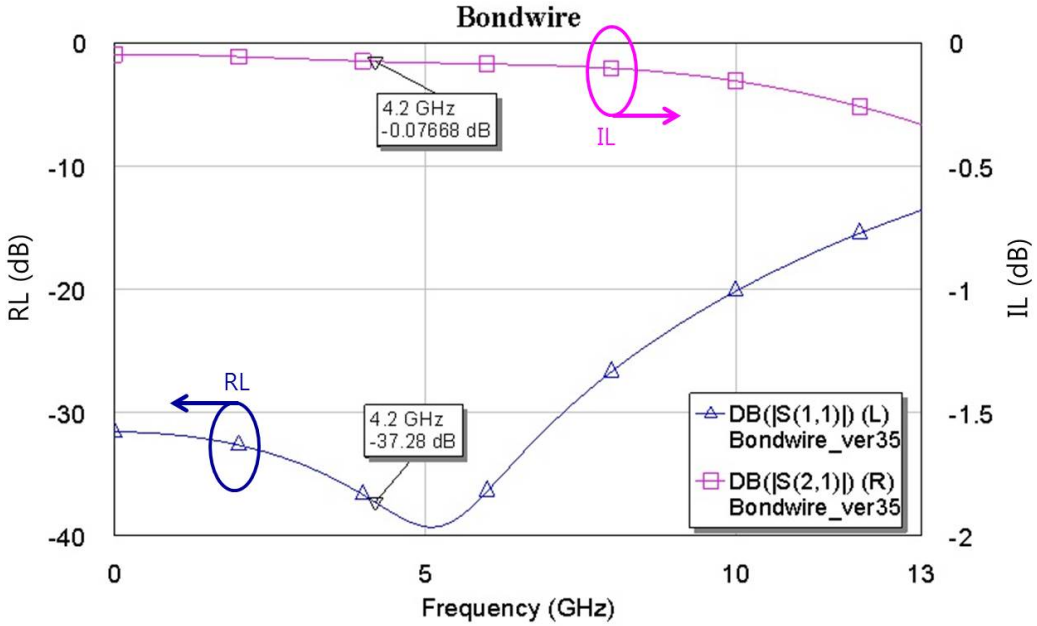

(b) Transition performance of the bondwire connection between switch and LTCC cicuit (simulated by CST [Computer Simulation Technology GmbH, 2010])

Figure 3.9: RF MEMS DPDT switch-LTCC circuit connection

3.3.2.2 Transmission line design

All transmission lines on the present switch matrix are designed to get 50 Ω characteristic impedance. A DPDT switch is also designed to have a 50 Ω impedance and the network assembly input/output impedance is the same as well. The distance between transmission lines is decided to suppress the line coupling and fulfill the crosstalk specification. Due to the LTCC board size limitation, the switching components are densely populated and transmission lines have to be densely located. However, a high transmission line population density causes a coupling problem. In this work, all transmission lines on the LTCC are separated by 4000 μm at least and ground via fences are inserted between them as shown in Figure 3.10. From the EM simulation, it is investigated that the coupling is less than -80 dB between 8000 μm long parallel lines.

What is worthy of being discussed is the stripline (SL) bending. In some positions, the SLs should be bent by 90° to interconnect switching cells. When the line is bent, an additional shunt capacitance is introduced from the corner. The additional shunt capacitance changes the local line impedance which degrades the transition quality. In this work, the corner is mitered by an optimal amount to compensate the additional shunt capacitance. Figure 3.11 compares the transition performance between a straight and a 90° bent SL through CST simulation [Computer Simulation Technology GmbH, 2010]. The 90° bent SL is mitered by 69% according to the EM optimization. It is investigated that the mitered SL shows a comparable transition performance to the straight one.

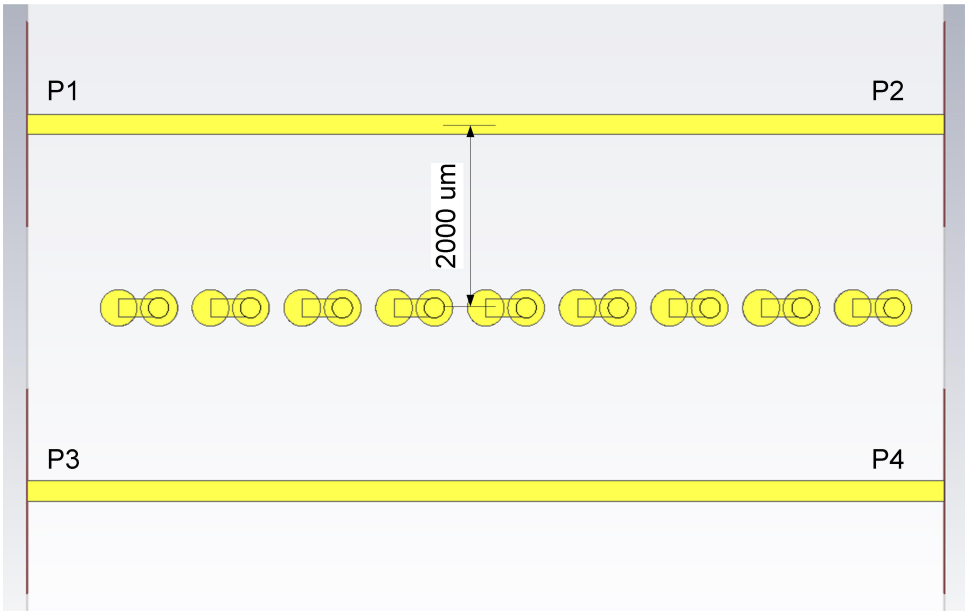

(a) Via fence between SLs

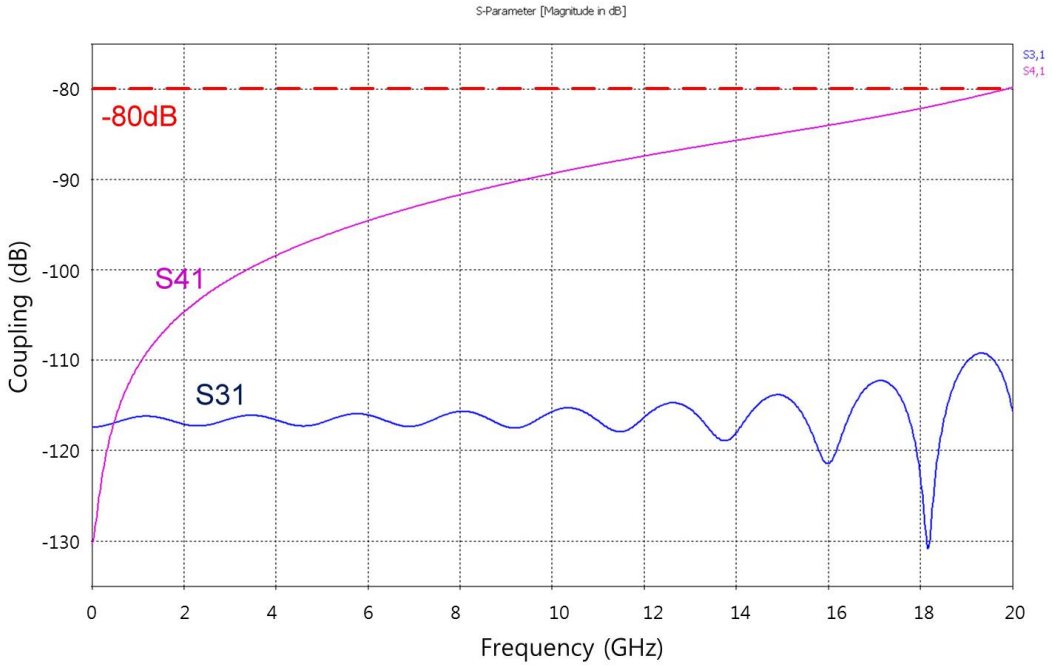

(b) Simulated Coupling between SLs using CST [Computer Simulation Technology GmbH, 2010]

Figure 3.10: Via fence insertion to suppress coupling between SLs

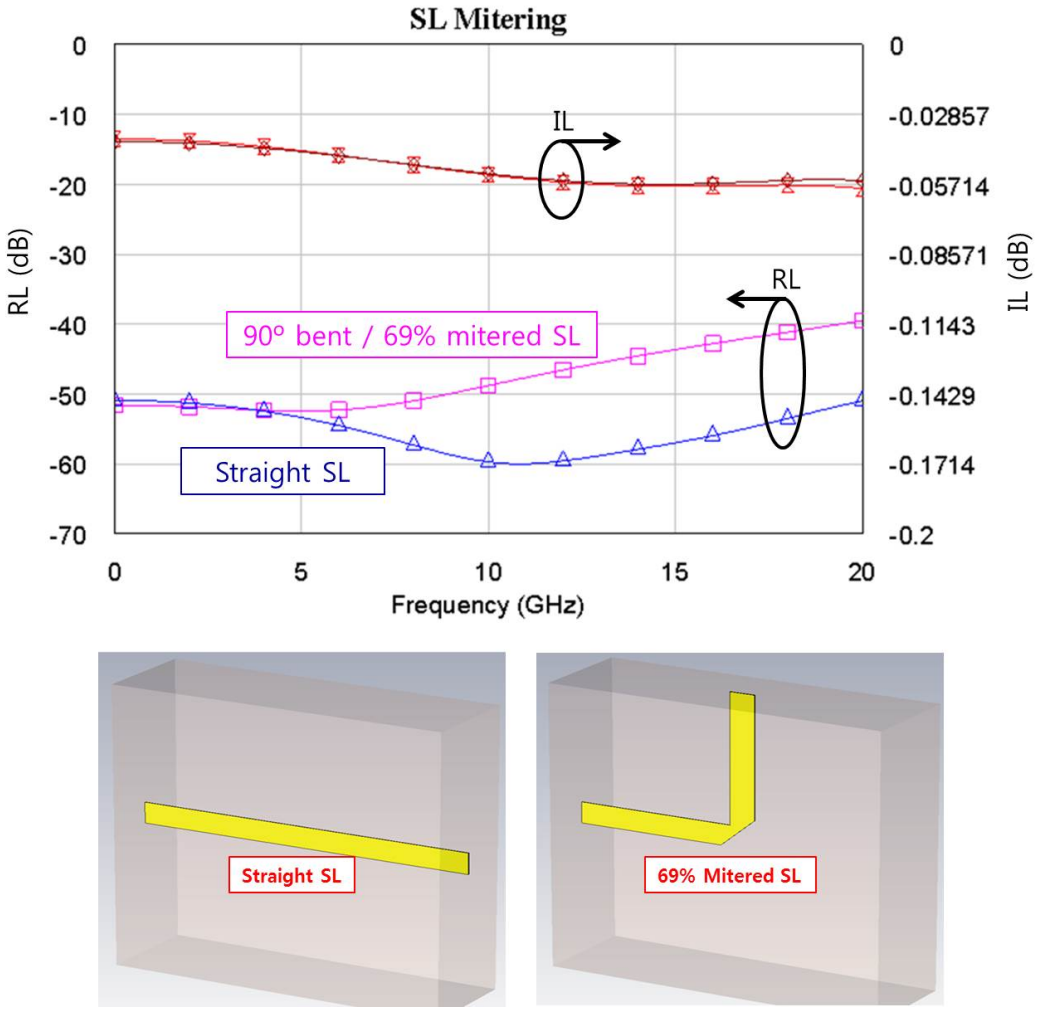

Figure 3.11: SL mitering to compensate additional shunt capacitance and the simulated transition performance by CST [Computer Simulation Technology GmbH, 2010]

3.3.2.3 Vertical transition

The planar Benes network physically involves lots of RF path crossings and the paths should be crossed without interference. Therefore, the network has to be realized by a multi-layer circuit technology involving vertical transmission lines.

The LTCC technology provided by TAS-I allows multiple layer via transitions, however the vertical via can only penetrate double LTCC layers at the maximum. A deeper penetration could make the LTCC crack or exhibit a stress concentration during the firing process.

Figure 3.12(a) shows three kinds of vertical transition involving 0°, 90° and 180° curves. The reason of designing three transitions is to minimize the accommodation areas. In many cases, vertical transition and bends are simultaneously required. Therefore, if they are realized together, a more compact network fabrication is possible. The vertical transitions in Figure 3.12 are optimized to have the best RF transition performance. Figure 3.12(b) shows the simulated transition performance by CST [Computer Simulation Technology GmbH, 2010]. It shows that the 180° transition has the best quality. For the 0°, 90° transitions, the optimal dimensions are out of feasible fabrication limits and cannot be further optimized.

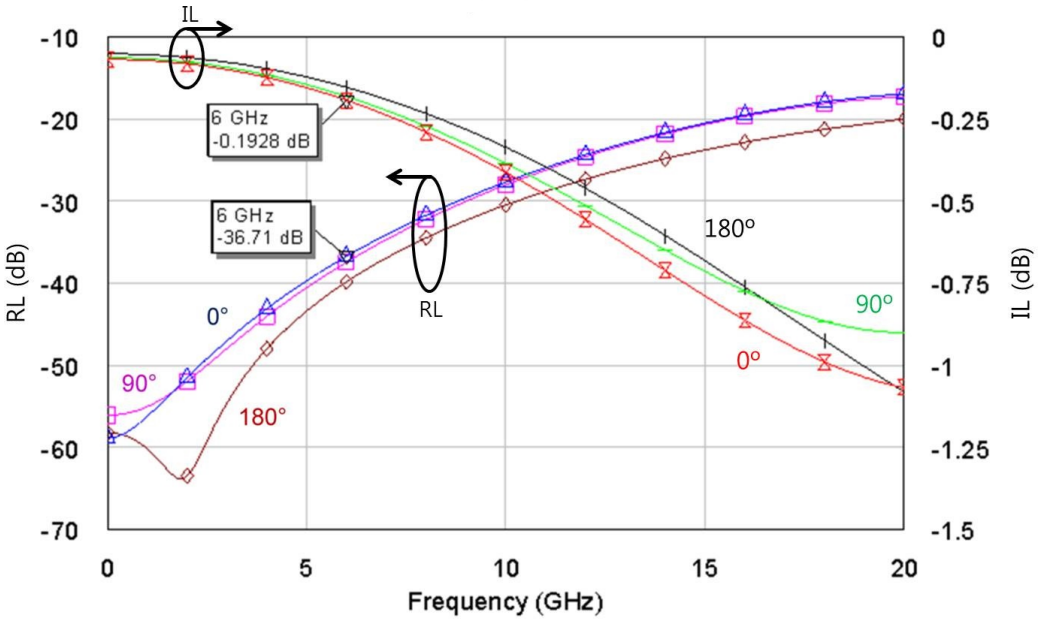

(a) Transition performance (simulated by CST [Computer Simulation Technology GmbH, 2010])

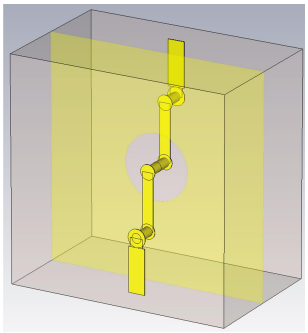

(b) 0°

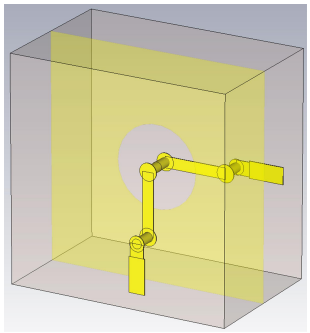

(c) 90°

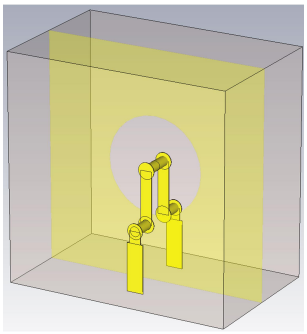

(d) 180°

Figure 3.12: Vertical transition between SLs

3.3.2.4 Board to Board transition

As discussed, the switch matrix consists of 4 LTCC boards connected by bond ribbons. Figure 3.13(a) shows the RF connection between LTCC circuits. To compensate a high bondribbon inductance, a CPW center line is widened. The amount of widening is decided through EM optimization. Figure 3.13(b) shows the simulated RF transition performance by CST [Computer Simulation Technology GmbH, 2010]. It is investigated that the RL is below -40 dB up to C band. It is difficult to design a broadband structure covering bands of interest. However, the matching is still better than -25 dB up to Ku band.

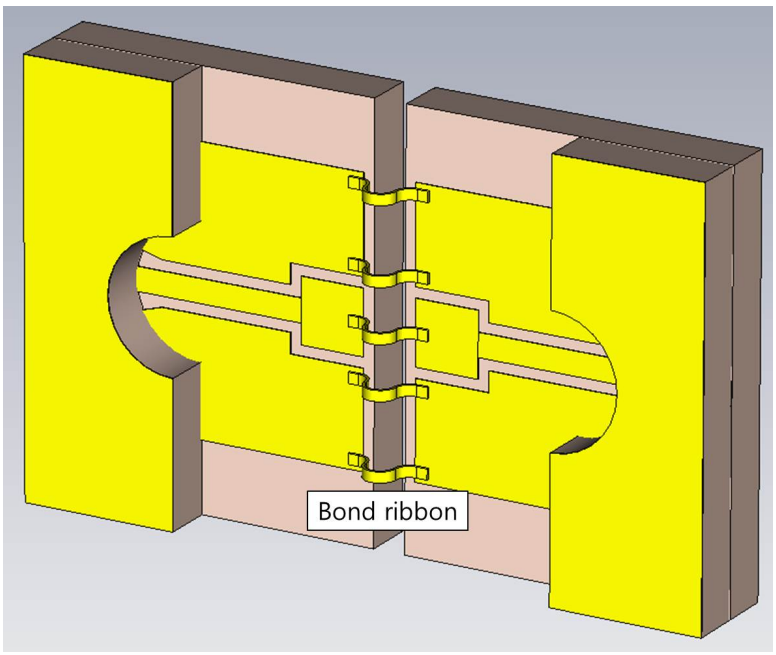

(a) Transition

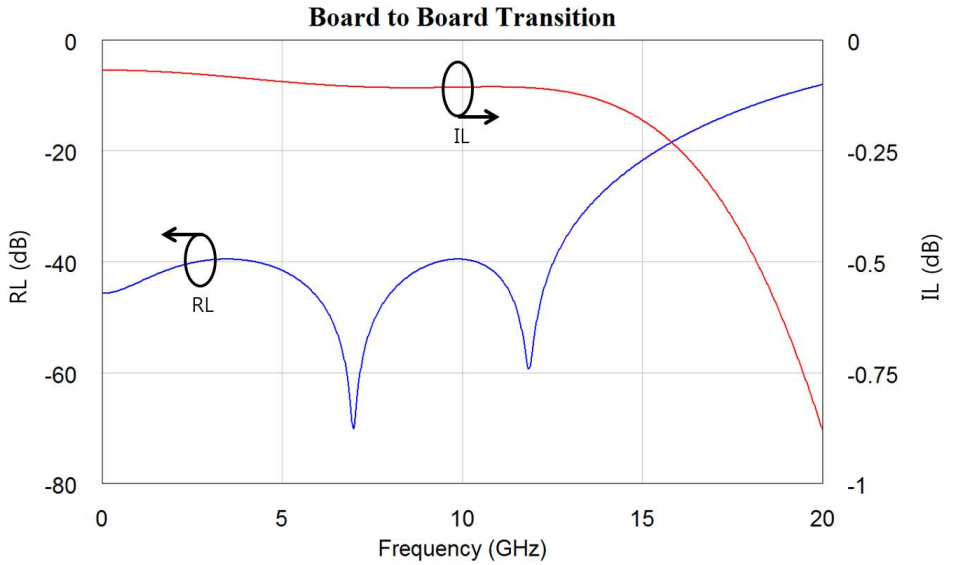

(b) Transition performance (simulated by CST [Computer Simulation Technology GmbH, 2010])

Figure 3.13: Board to board transition

3.3.2.5 Alumina-LTCC connection

The RF signal delivery between the switch matrix and the environment is achieved by 24 input/output RF ports mounted on the switch matrix housing. The inner LTCC circuits are connected to RF ports by intermediate circuits on the alumina boards. The reason of using intermediate alumina boards is to avoid LTCC edge-RF pin collisions when the LTCC boards are installed on the housing. Figure 3.14(a) shows an Alumina-LTCC bond ribbon transition including bond ribbon compensation structures. From Figure 3.14(b), it is investigated that the RL is better than -30 dB up to Ku band.

The structure in Figure 3.15(a) is to check the coupling between multiple Alumina-LTCC transitions. Figure 3.15(b) shows the simulated couplings between one port (P5) to the other ports (P1,...,P4, P6,...,P24). They are all below -50 dB.

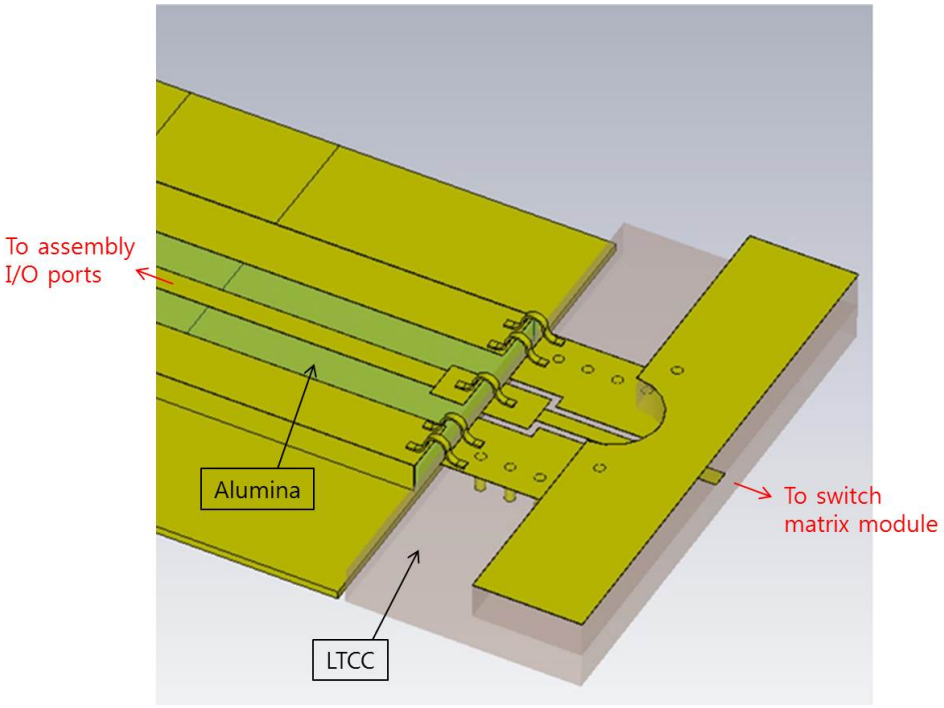

(a) Transition

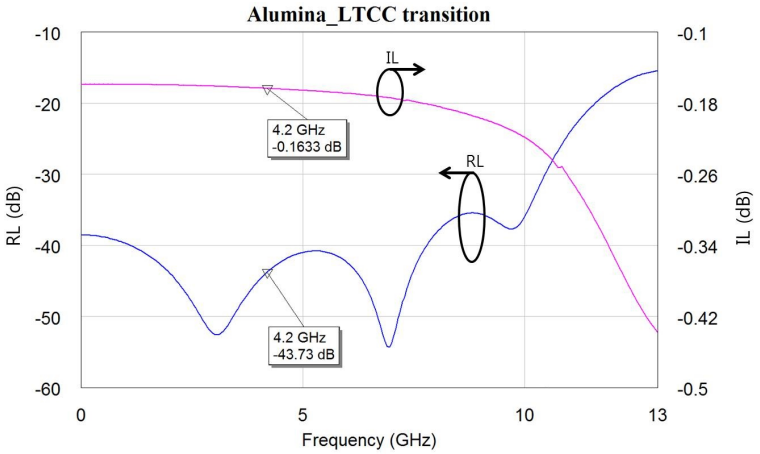

(b) Simulated transition performance by CST [Computer Simulation Technology GmbH, 2010]

Figure 3.14: Alumina-LTCC transition

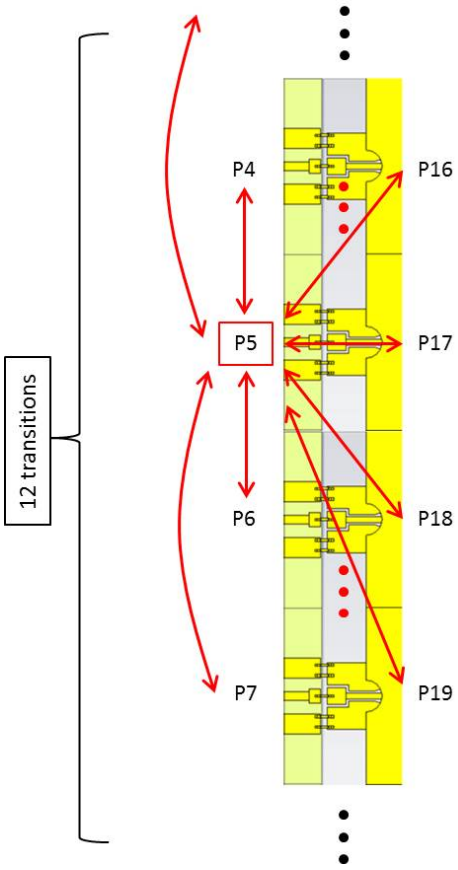

(a) Multi transition

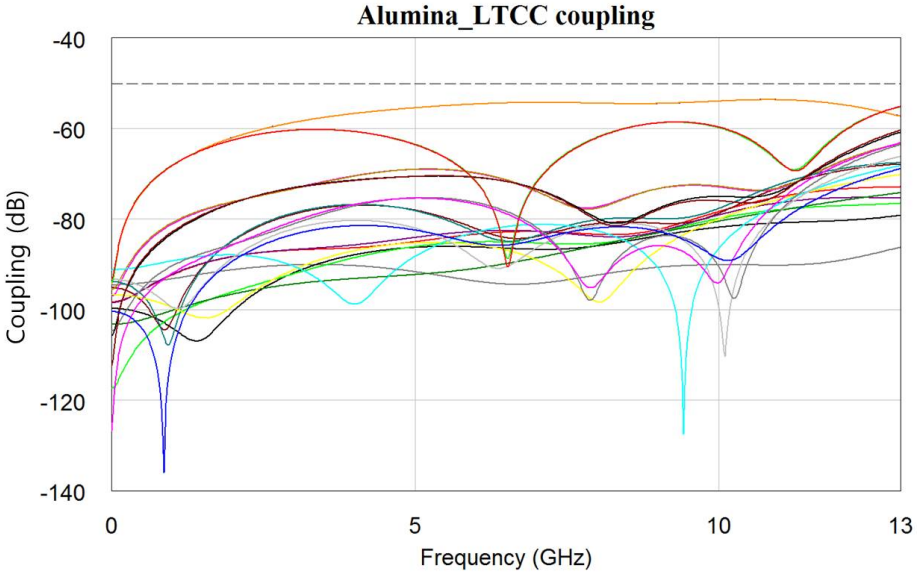

(b) Simulated coupling by CST [Computer Simulation Technology GmbH, 2010]

Figure 3.15: Multiple Alumina-LTCC transitions

3.3.2.6 Cavity resonance

The DPDT switch is encapsulated by the metal cap, vias and the ground plane. Therefore, a resonance may occur if the box resonance frequency is located in the target frequency bands. The resonance may cause unexpected peaks or ripples which jeopardize the RF transition performance. Therefore, the resonance inside a cavity is to be checked.

The Figure 3.16 shows a simulated resonance of the switch cavity. The simulation has been done by using the Eigenmode solver of CST MICROWAVE STUDIO [Computer Simulation Technology GmbH, 2010]. It is investigated that the first resonance occurs at 14 GHz, which is out of the bands specified in Table 3.1. With the designed cavity size, it is expected that there is no resonance problem at the operating frequency.

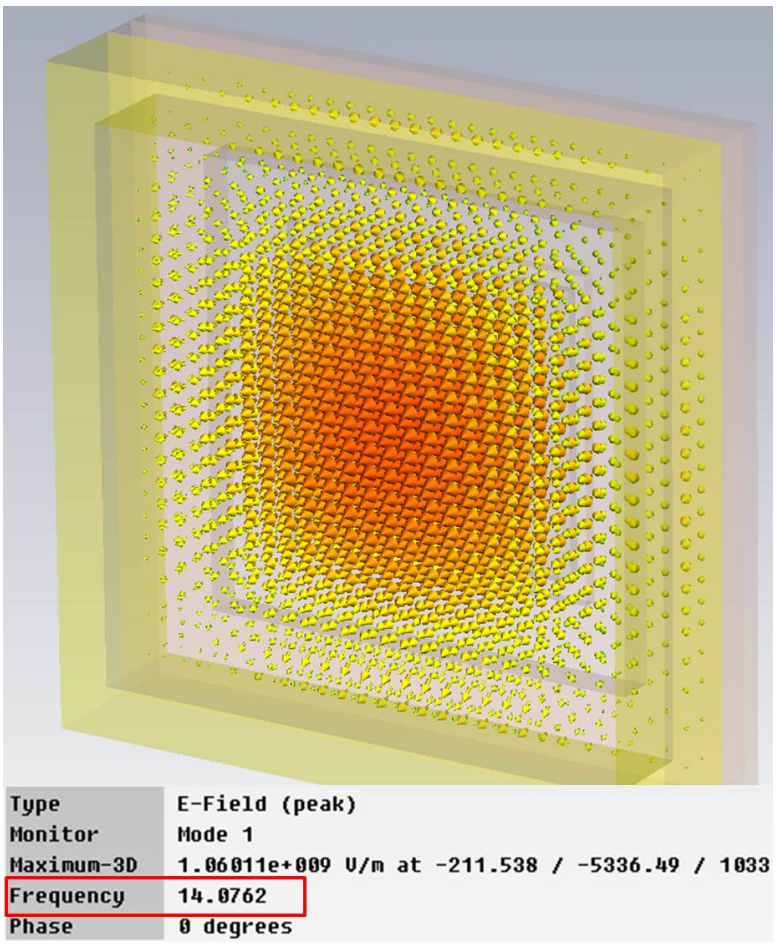

(a) Perspective view

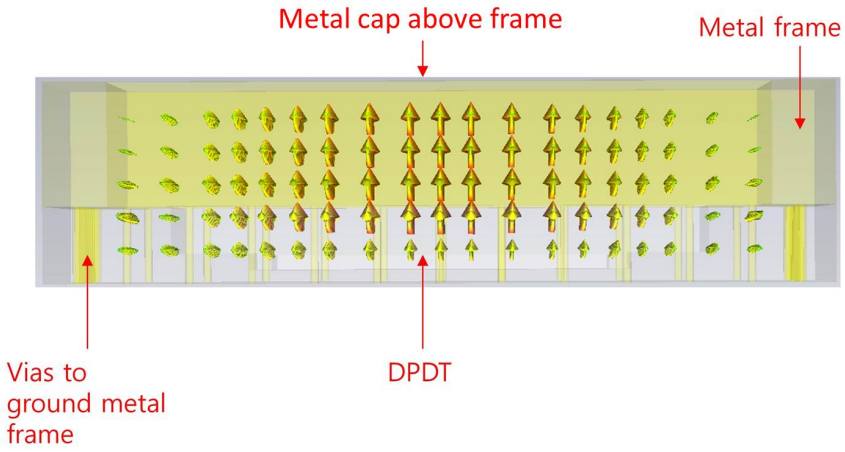

(b) Side view

Figure 3.16: Simulated resonance inside the cavity which DPDT switch is mounted (simulated by CST [Computer Simulation Technology GmbH, 2010])

3.3.3 Network control

Generally, high-order switch matrices require a specific control algorithm because they normally involve lots of assignment signals. In the proposed matrix, 144 control inputs should be simultaneously assigned. Moreover, the number of feasible matrixing configurations is 479,001,600 (=12!), which is not manageable by the manual way or referring to look-up tables. Therefore, the specific control algorithm should be implemented to generate desired control input assignments for any permutations. There are lots of control algorithms which have been mainly investigated in computer architecture. The representatives are looping algorithms, m-matching algorithms, Euler partition algorithms, Karol's algorithms or frame-based matching algorithms, etc.

For the Beneš network, one of the oldest but still powerful control algorithm is the looping algorithm. It is a simple sequentially optimal matching algorithm. The main constraint of the looping algorithm is that the network has to possess two center modules and the input/output switching elements should be of 2x2 order. The proposed switch network uses DPDT switches with 2x2 order and its center stage consists of two identical modules, which satisfies the constraint of the looping algorithm [Chao and Liu, 2007]. Therefore, in the present work, a looping algorithm is used. The graphical user interface shown in Figure 3.17 is programmed based on MATLAB [The MathWorks, Inc., 2010]. By using the looping algorithm, it calculates the DC control signals which should be applied to the DC pads on the LTCC board according to the port assignment. It also exports the generated DC control inputs to ASCII file which can be used for the controller inputs.

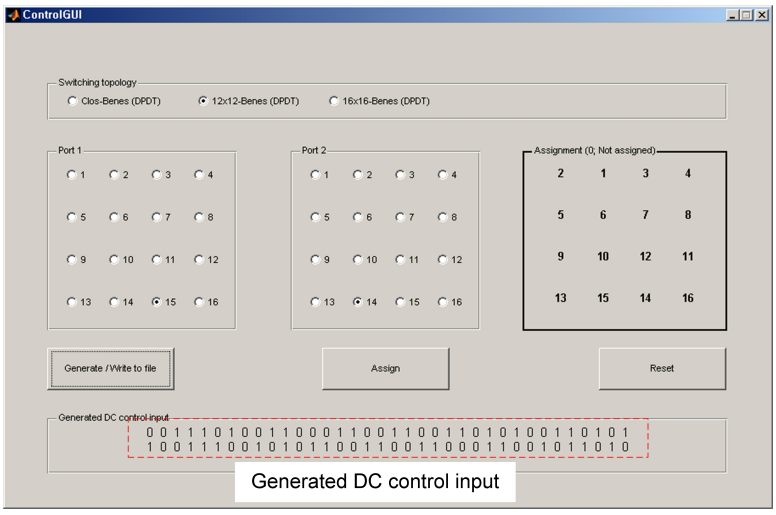

Figure 3.17: Control input generation using looping algorithm

3.4 EM simulation of the full matrix

Since the switch matrix is large and involves complicated structures, it is difficult to perform a full-wave simulation for the entire matrix. In this work, the specific parts are full-wave simulated by CST and their results are combined by a circuit simulator by AWR Microwave office [Computer Simulation Technology GmbH, 2010; National Instruments, 2010].

3.4.1 4x4 switch matrix

The 4x4 switch matrix in Figure 3.18 has been fabricated to verify the design process used for the 12x12 switch matrix design. The 4x4 matrix is a simplified version of the 12x12 matrix. The differences are as follows:

- There is no bond wire compensation structure in the DPDT switches because DPDT switches with compensation structures are not fabricated at the time of the 4x4 matrix fabrication. This means that only the LTCC circuits contain the bond wire compensation structures. Therefore, the matching is expected to be worse compared to the 12x12 network which adopts double side bond wire compensation.
- No via fence is inserted between SLs.
- DPDT switches are mounted on the higher layer in the LTCC board. In other words, the DPDT circuit is at the same level as the surface of the LTCC board.

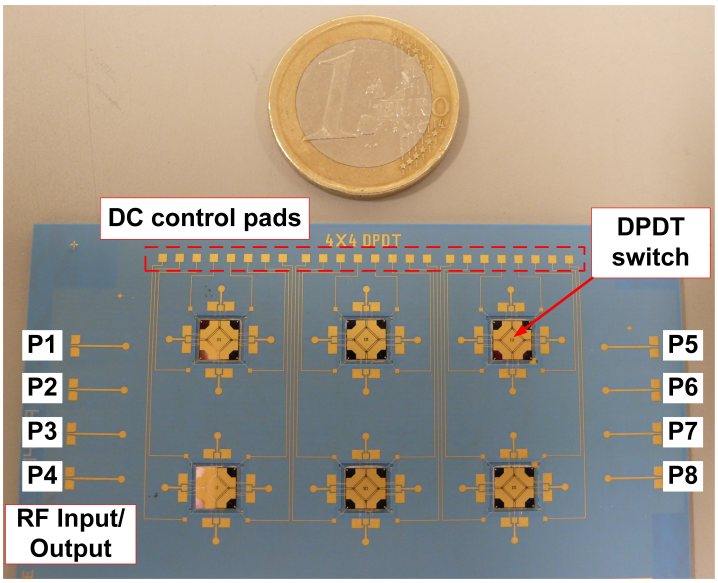

Figure 3.18: Fabricated 4x4 switch matrix [DiNardo et al., 2013]

For the 12x12 network, the DPDT switches are mounted deep into the SL level as depicted in Figure 3.6.

- It has an MSL-SL transition to connect DPDT switches to LTCC circuits. The 12x12 network has no MSL-SL transition.

Despite the listed differences, the 4x4 matrix analysis is still important because the 4x4 matrix and 12x12 fabrications have the same simulation/optimization approaches.

Figure 3.19 and Figure 3.20 describe the performance of the 4x4 switch matrix. The measurement has been performed using multi-standard de-embedding structures at the 1-6 GHz and 4-20 GHz frequency bands. Figure 3.19 shows the RL, IL and Isolation when port 1 and 5 are connected, and Figure 3.20 port 4 and 5 connection on each. The solid and dashed lines stand for the measured and simulated results on each. The measurements have been carried out by CNR and CST has been used for simulation [Computer Simulation Technology GmbH, 2010]. The transition performance does not fulfill the design specifications. That is mainly due to the imperfect bond wire compensation between the switches and the LTCC circuits. The switches are produced from the first fabrication run and they have no compensation structures. However, in terms of the IL and RL, the simulation and measurement results show a good agreement. The crosstalk level is below -50 dB up to 4.5 GHz.

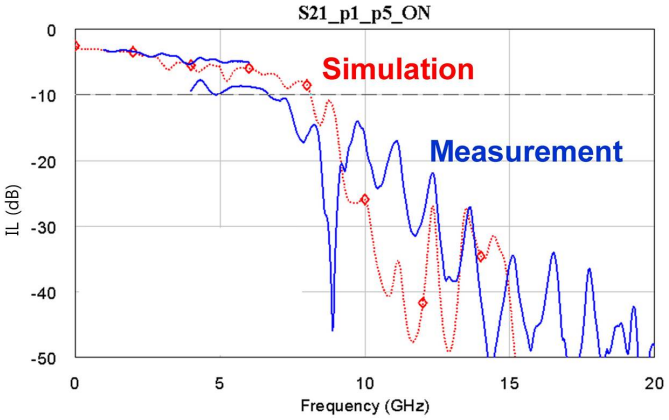

(a) IL (P1-P5)

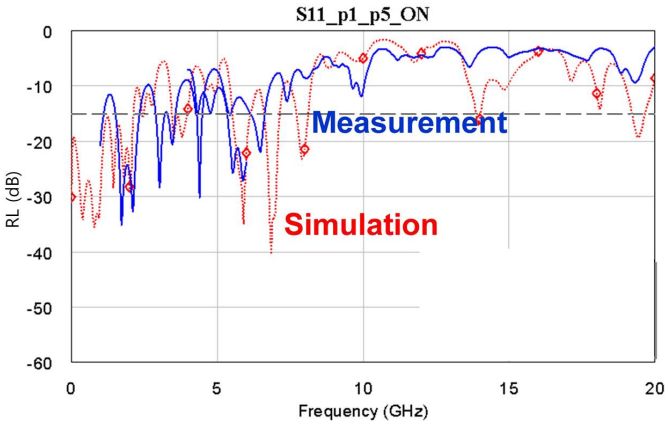

(b) RL (P1-P5)

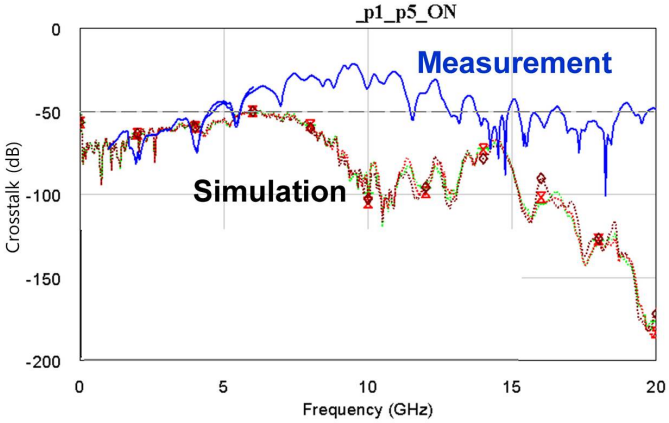

(c) Crosstalk (P1-P5)

Figure 3.19: Performances of the 4x4 switch matrix P1-P5 (measured by CNR, simulated by CST and AWR [Computer Simulation Technology GmbH, 2010; National Instruments, 2010])

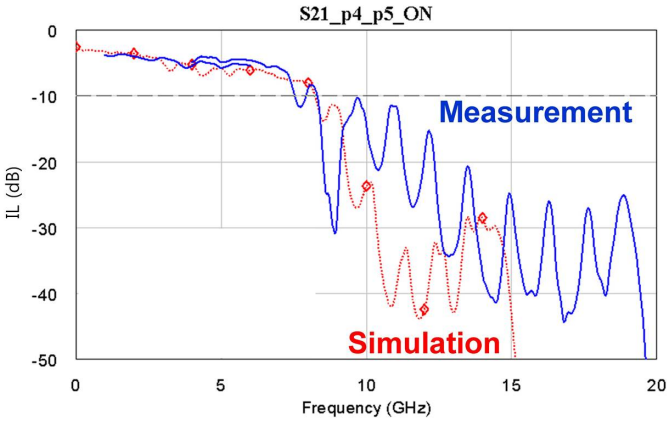

(a) IL (P4-P5)

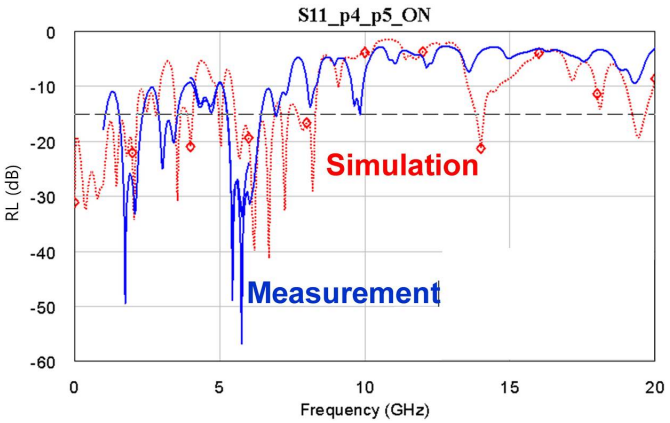

(b) RL (P4-P5)

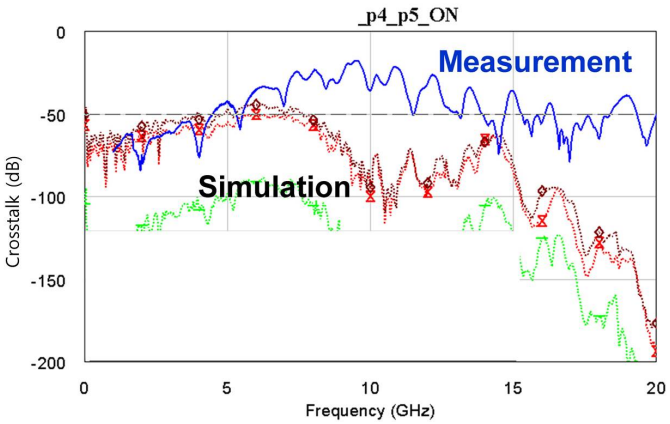

(c) Crosstalk (P4-P5)

Figure 3.20: Performances of the 4x4 switch matrix P4-P5 (measured by CNR, simulated by CST and AWR [Computer Simulation Technology GmbH, 2010; National Instruments, 2010])

3.4.2 12x12 planar Beneš network

As aforementioned, the matrix is designed by full-wave EM simulation together with circuit simulation. The matrix is divided to sub-sections and each sub-section has been designed by full-wave EM simulation. The parts expected to have significant couplings have not been divided to account for the crosstalk as accurate as possible. For example, all striplines on the laminate are full-wave EM simulated without division. For the full-wave and circuit EM simulations, CST and AWR have been used [Computer Simulation Technology GmbH, 2010; National Instruments, 2010].

In the 12x12 network, lots of permutations are possible. It is impossible to check every permutation. Therefore, the EM simulation is carried out for the specific cases involving the best and the worst cases in terms of RF performance. The best and the worst cases are decided considering the number of RF transitions (LTCC-DPDT switch transition, vertical transition, etc.) and the number of switches on the path. Figure 3.21 shows the port number assignment and selected paths. The test assignment is selected so that they may involve the best and worst cases.

3.4.2.1 IL

The 12x12 planar Beneš network is not a symmetric network in terms of the IL. The IL performance is path dependent. This is because the number of DPDT switching, vertical transitions and the transmission line length are different according to the path.

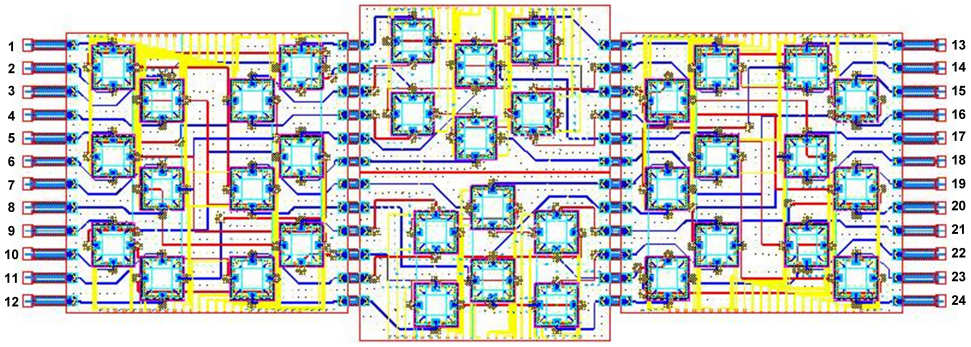

(a) Matrix port number definition

Input	1	2	3	4	5	6	7	8	9	10	11	12
Output	13	17	14	16	20	19	18	21	23	15	22	24

(b) Test port assignment

Figure 3.21: Matrix port assignment for test

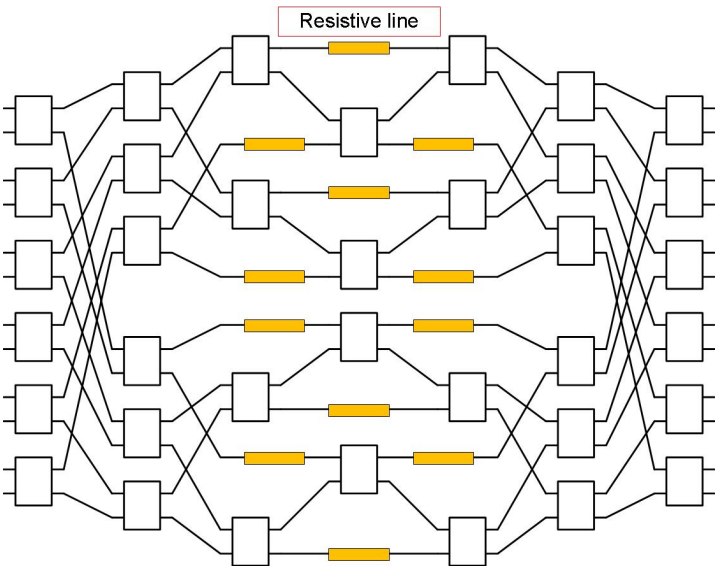

Figure 3.22: IL balancing by inserting resistive lines

This is not desired because the switch matrix should be as transparent as possible from the RF signal's point of view. Therefore, IL balancing using resistive lines is adopted. As described in Figure 3.22, 12 resistive lines are inserted where the DPDT switch is absent due to the network asymmetry. This means, the resistive line compensates the IL contribution of the missing DPDT switch. A buried resistor CF011 is used as the resistive material. The CF011 is co-processed with the LTCC fabrication and has a 10 Ω/sq sheet resistance [Resistors, 2013]. The structures in Figure 3.23 are to check a loss contribution of the resistive line. Figure 3.23(a) shows the structure design and Figure 3.23(b), (c) are the fabricated test structures with two different CF011 line lengths. By comparing ILs of the two structures, the practical sheet resistance can be figured out. The measurement says that the loss from the resistive line is -5.84 dB/mm, which corresponds to 58 Ω/sq sheet resistance. Considering unbalanced IL difference, it is decided to use 200 μm long resistive lines.

Figure 3.24 shows the simulated ILs for the path given in Figure 3.21(b). The simulation result shows the IL deviation is less than 1 dB up to C band. At Ku band, the difference is still 5.57 dB. It's possible to decrease IL deviation up to Ku band by inserting a higher resistive line. However, the excessive resistance leads to a severe RL increase. It is difficult to balance IL up to the high frequency due to the high RL degradation.

The IL is higher than 10 dB for all frequency bands, which is higher than the desired specification. It is expected that the network needs a signal amplifier to compensate the high IL. To adopt a low loss circuit substrate could be a solution to decrease the IL, since a considerable portion of the loss is contributed by the transmission line. The

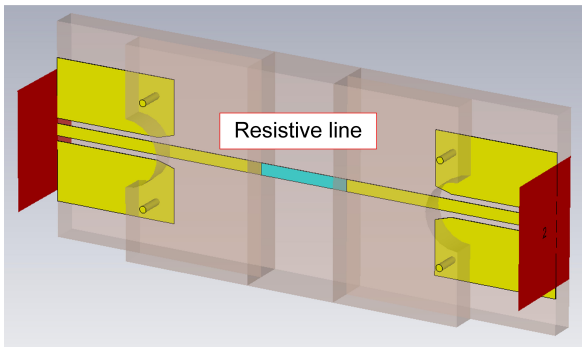

(a) Test structure design

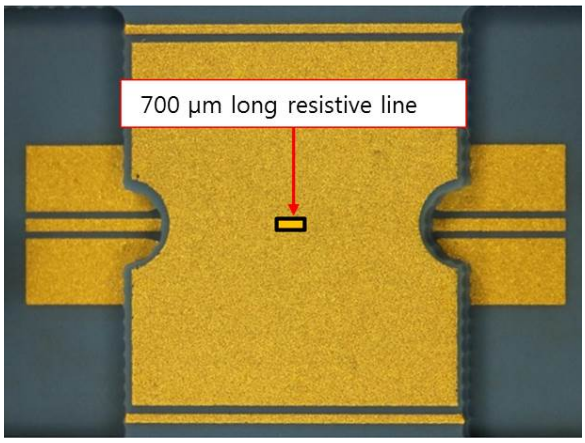

(b) 700 μm long resistive line

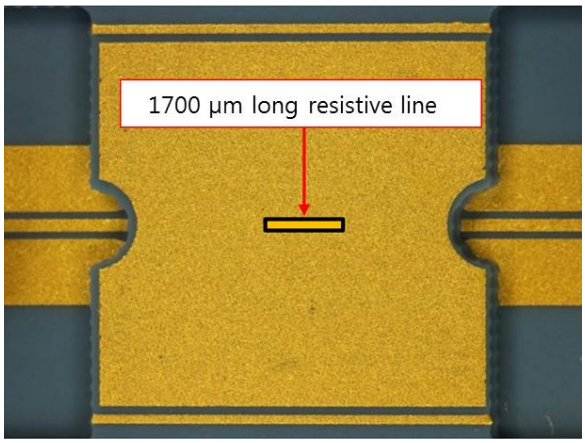

(c) 1700 μm long resistive line

Figure 3.23: Test structure to check resistivity of the resistive lines

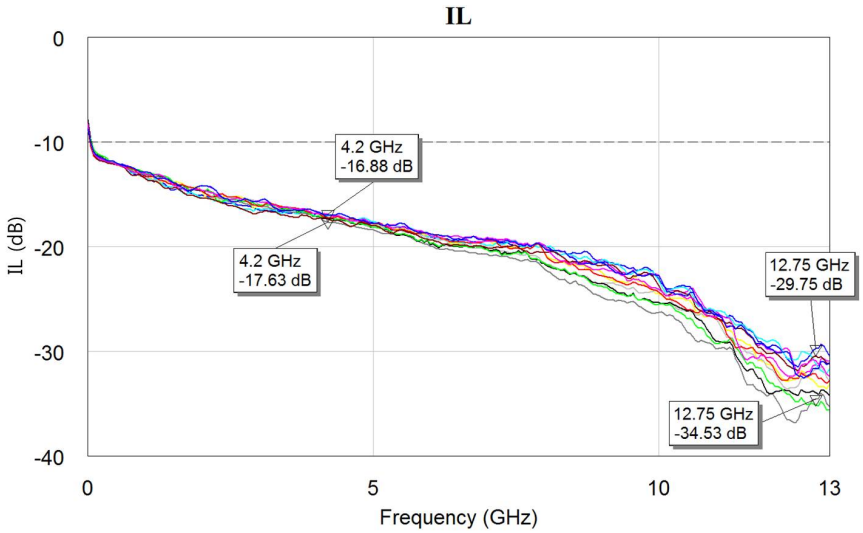

Figure 3.24: Simulated IL by CST and AWR [Computer Simulation Technology GmbH, 2010; National Instruments, 2010]

LTCC material (DuPont 951) is relatively lossy ($\tan\delta = 0.045$).

3.4.2.2 RL

Figure 3.25 describes the RL of the switch matrix. Figure 3.26 and Figure 3.27 are scaled graphs on each frequency band of interest. It is investigated that the RL is -12 dB,..., -15 dB up to C band in overall. It is difficult to maintain the RL level comparably up to Ku band. This is mainly due to the bondwire transition. It is possible to suppress the Ku band RL by changing the shunt capacitance of which the bond wiring is constructed. However, in this case, the other band's RF performance get worse. The bondwire transition is a kind of filter. With the given condition, it is hard to design effective broadband compensation structures covering up to Ku band. In this work, the optimization effort is more devoted to the L, S and C band performance improvement.

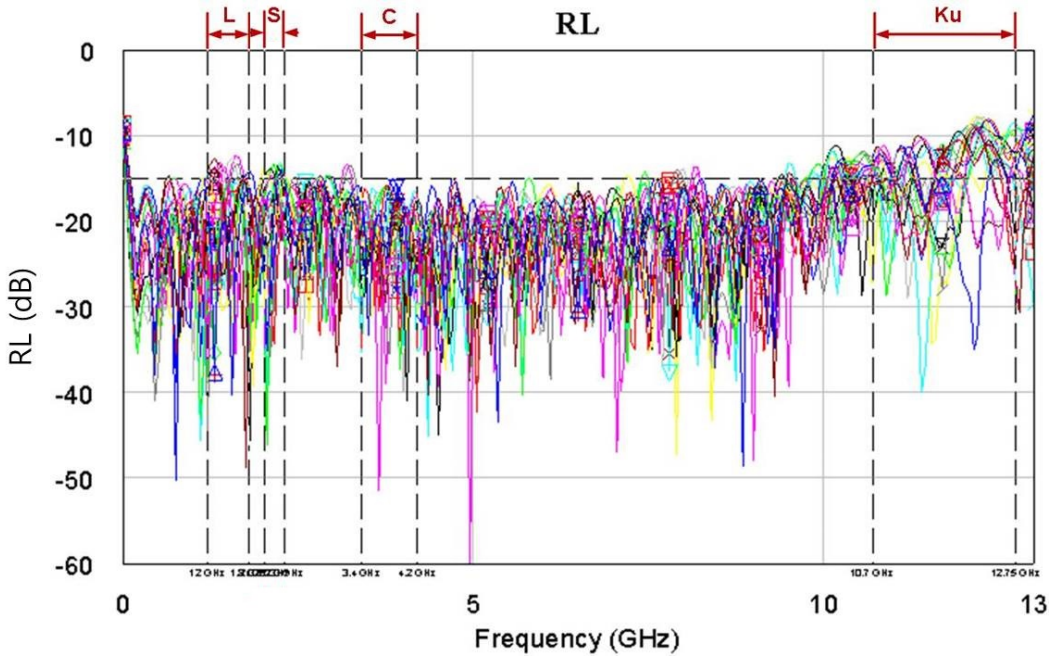

Figure 3.25: Simulated RL of 12x12 planar Beneš network by CST and AWR [Computer Simulation Technology GmbH, 2010; National Instruments, 2010]

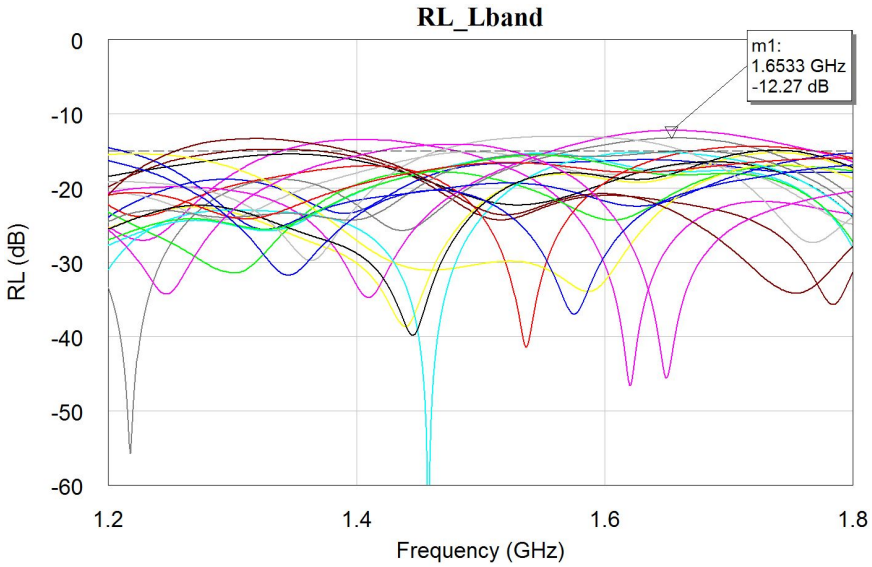

(a) L band

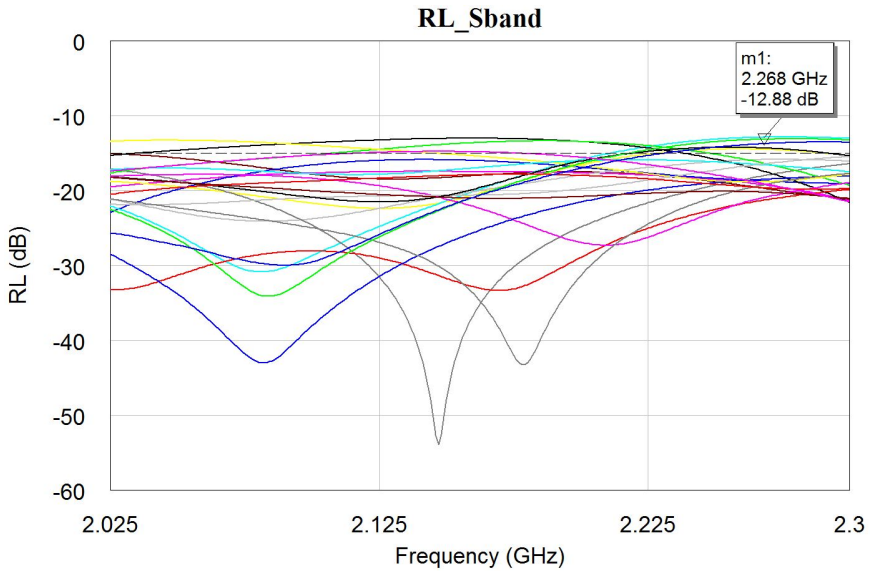

(b) S band

Figure 3.26: Simulated RL - L, S bands (by CST and AWR [Computer Simulation Technology GmbH, 2010; National Instruments, 2010])

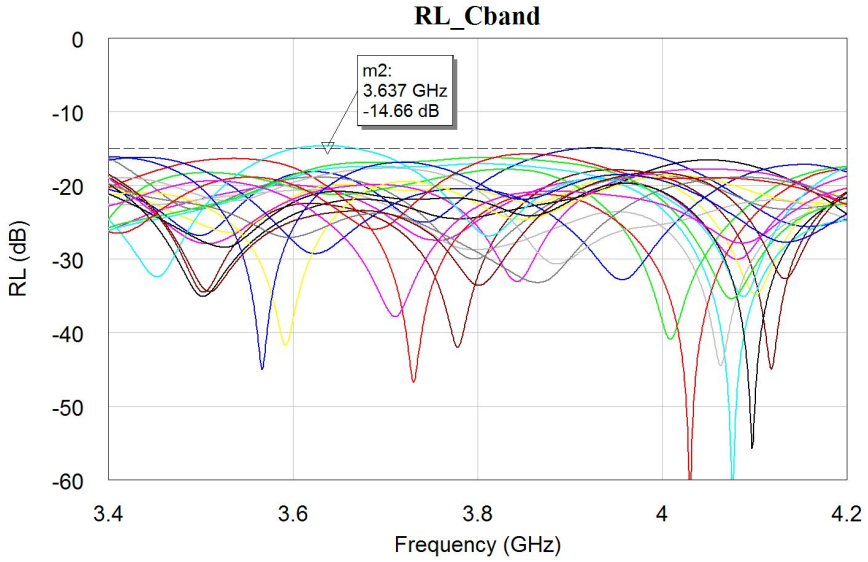

(a) C band

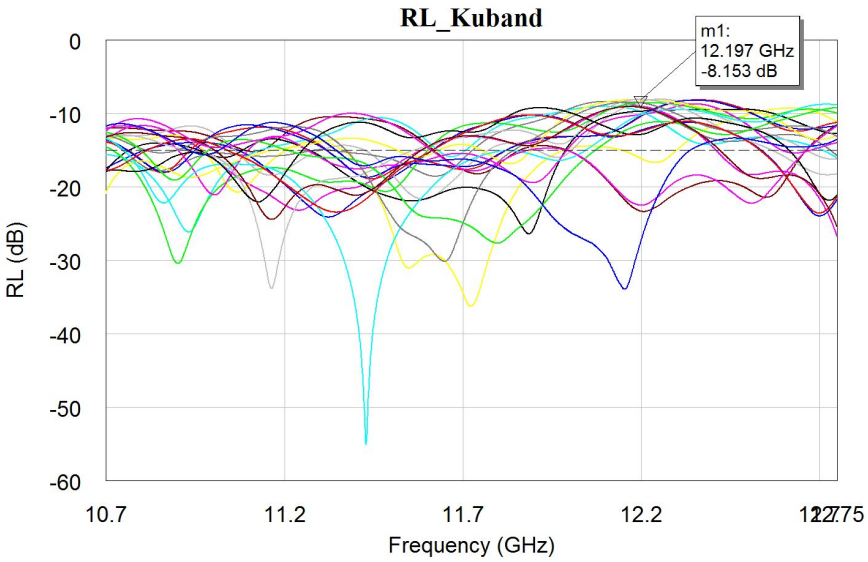

(b) Ku band

Figure 3.27: Simulated RL - C, Ku bands (by CST and AWR [Computer Simulation Technology GmbH, 2010; National Instruments, 2010])

3.4.2.3 Crosstalk

Figure 3.28 shows the crosstalks between a reference path (P5-P20) to the other paths. The crosstalk level can be categorized into three groups in terms of the physical distance and the number of switching elements shared with the reference path. The highest crosstalk occurs between the paths which share the same DPDT switches with the reference line by 1 2 times. It is investigated that the maximum crosstalk is smaller than -50 dB over the frequency of interest.

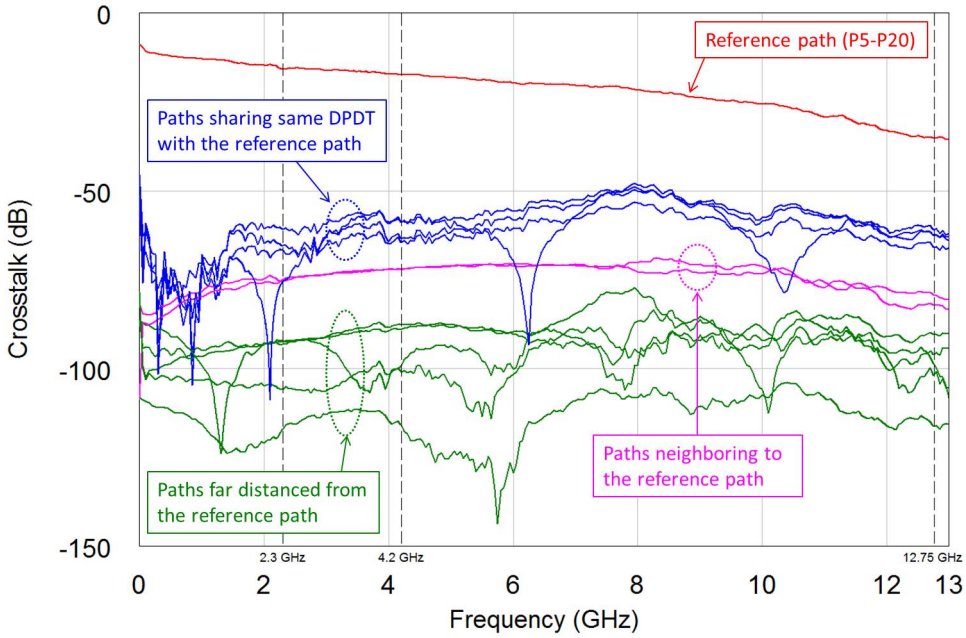

Figure 3.28: Crosstalk from the reference path to the others (simulated by CST and AWR [Computer Simulation Technology GmbH, 2010; National Instruments, 2010])

3.4.2.4 Sensitivity

The fabrication process generally involves manufacturing errors such as component mis-positioning, misalignment or size deviation, etc. The manufacturing scattering becomes dominant when the whole assembly's complexity increases.

The proposed planar Beneš network consists of many components. Ideally, they should be precisely fabricated, positioned and assembled. RF performance scattering from the DPDT switches can be ignored because they are fabricated by a fine semiconductor technology with high resolution. The LTCC circuitry manufacturing scattering is a little bit higher, but it does not deviate RF performance significantly. According to the test structure measurements, a meaningful RF performance scattering is investigated from the bond wire connections. The structures having bond wire connections show a higher discrepancy between measurement and simulation compared to the ones which don't have any. This is because the bond wire is manually soldered. The bonding position is easily mis-located.

Figure 3.29 shows the DPDT switch to LTCC circuitry connection via double bond wires. In principle, two center bond wires should be as short as possible and they must be maximally distanced to reduce mutual inductance. Therefore, a 0-0 connection would be the best. This positioning is also recommended by TAS-I. The other positions 1-1, 2-2 and 3-3 suppose the mis-positioning shifted by 100 μm.

Figure 3.30 shows the RF performance deviation simulated by CST and AWR [Computer Simulation Technology GmbH, 2010; National Instruments, 2010]. The pair (0-0, 1-1) and (2-2, 3-3) show a similar performance. This means the the mutual coupling deviation is more dominant compared to the series inductance change. It is also investigated that the RL and IL do not change too much up to C band. For Ku band, the performance deviation pronounces, but the amount is not significant. This means, the RF performance of the matrix is not severely affected by the bond wire construction errors up to C band. At Ku band, they contribute more. If an automatic bonding machine was used, the RF performance deviation could be lowered.

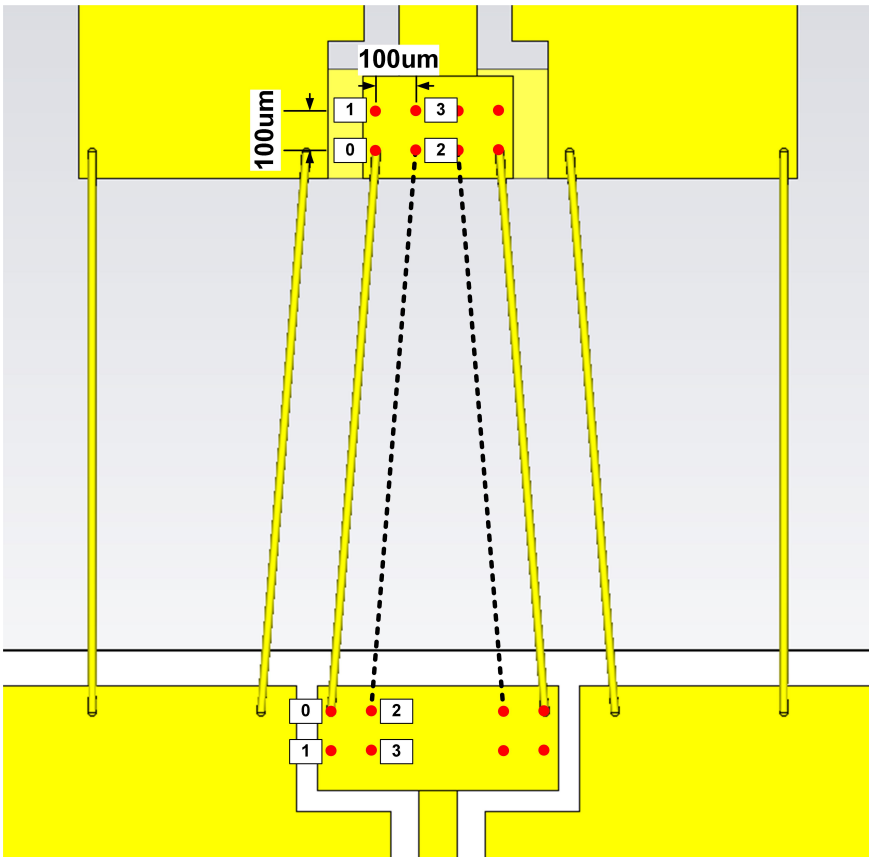

Figure 3.29: Sensitivity analysis model

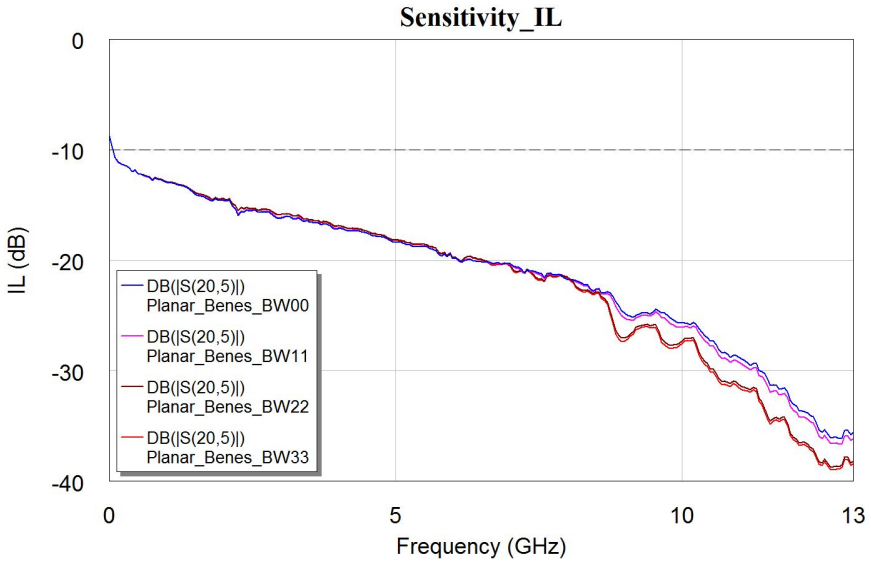

(a) IL variation

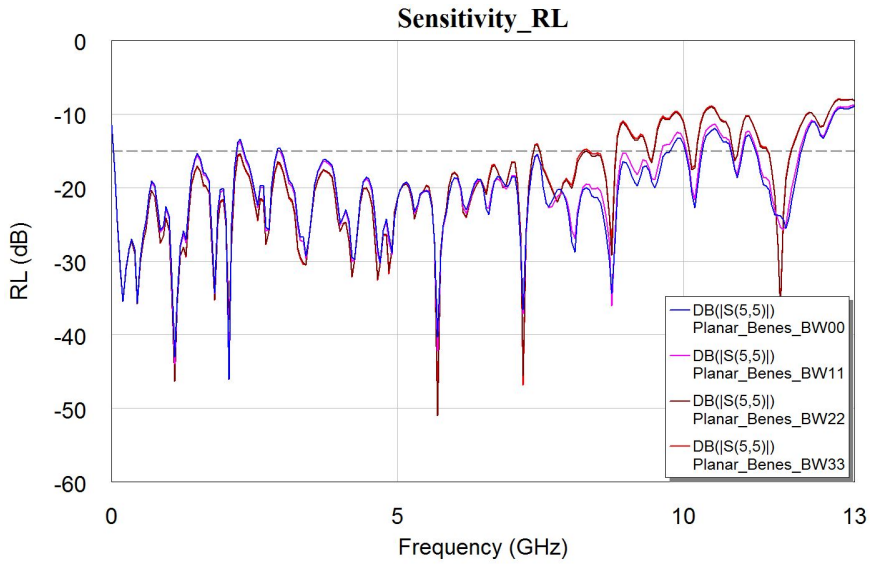

(b) RL variation

Figure 3.30: Sensitivity analysis (simulated by CST and AWR [Computer Simulation Technology GmbH, 2010; National Instruments, 2010])

3.5 Conclusion

The presented work has been carried out in the frame of the ESA Project No AO/1-5136/06/NL/GLC. The responsible parts of TUM were network topology definition, control algorithm programming and RF circuit design including the physical layout drawing.

Table 3.2 lists RL, IL and couplings of the planar Beneš network. According to the frequency increase, the IL becomes worse. At Ku band, IL is worse than -30 dB. The simulated RL is 12 dB,...,15 dB up to C band. The crosstalks at L, S and C band are about -47 dB,...,-40 dB, which mainly comes from DPDT switch.

It is possible to construct a high order switch matrix using RF MEMS technology. However, the complexity dramatically increases along with the order increase. It is not easy to accommodate a high order switch matrix on a limited area. Moreover, it requires an efficient control algorithm since the number of permutations is huge and the paths have to be simultaneously assigned. In this work, a simple looping algorithm is used to control 36 DPDT switches on the matrix. Since many RF MEMS switches are involved, their level of integrity is also concerned. Each switch has to possess a uniform performance and all switches should be mounted by a definite method so that they may have identical transition performance with the LTCC circuitry. The measurement strategy has to be discussed as well. Since the measurements for all permutations are physically impossible, the representative permutations which can verify the network performance are to be decided. After the first prototype is assembled, the environmental test will follow for space application, which includes shock immunity test, vibrations and abrupt temperature changes.

Band	**IL[dB]**	**RL[dB]**	**Coupling[dB]**
L band	-15.14,...,-14.64	-12.27	-45.54
S band	-15.86,...,-14.93	-12.88	-46.79
C band	-17.73,...,-16.9	-14.66	-41.72
Ku band	-36.15,...,-30.56	-8.15	-25.68

Table 3.2: 12x12 planar Beneš network RF performance

4 Smart Antennas using RF MEMS and Metamaterials

4.1 Introduction

4.1.1 Smart antennas

Smart antennas have been investigated for fast reconfigurable networks or features which require high data rate, user mobility and adaptability to the varying network conditions. They are remarkably used in tracking and scanning RADAR (RAdio Detection And Ranging), acoustic signal processing, cellular systems, etc. Recently, due to the need of efficient high speed communicating systems for moving vehicles, there is a strong demand for beam steerable high frequency antennas.

One of the important features of smart antennas is beam steerability. A beam steerable antenna can control the beam firing direction and even focus on a specific point with high gain [Alexiou and Haardt, 2004]. The conventional beam steering method is to use an active phased array with phase shifter MMICs (Monolithic Microwave Integrated Circuits). Many phase shifters have been based on solid state components such as varactor diodes or FETs. But their fabrication cost is rather high to construct multiple numbers of MMIC chips with high complexity. They suffer from high loss and low linearity, especially at mm-wave applications. Smart antennas using RF MEMS technology have been discussed as one of the best candidates due to its low loss and highly linear functionality up to microwave frequencies. Generally, reported MEMS phase shifters show about 4 dB improvement compared to GaAs FET based device [Schobel et al., 2004; Lee et al., 2006].

4.1.2 Beam steerable antennas using RF MEMS technology

RF MEMS beam steerable antennas can be classified into two types, mechanical or electrical. In the mechanical steering approaches, the beam firing direction is mechanically changed by the physical movement of the beam radiator. The mechanical steering antenna possesses constant RF gains and does not require phase shifters [Kim et al., 2011; Baek et al., 2003]. But they need complicated moving structures which generally require a cost-effective fabrication process. Moreover, the steering speed is much slower especially compared to the electric steering approach, since the whole part of the antenna should be physically tilted or rotated.

In electrical beam steering, the antenna changes the beam firing direction by changing electric properties such as electrical length, phase velocity or propagation constant. The representative method is to use phased arrays connected to phase shifters. Many RF MEMS phase shifters adopt several phase shifting methods such as switched line, loaded line, reflected line or distributed line types, etc. Generally, switched line phase shifters are simple and easy to be implemented. They are also simpler and faster than the mechanical steering. For smart antennas using RF MEMS phase shifters, the electric beam steering time is mainly determined by the RF MEMS switching speed.

4.1.3 Beam steerable antennas using metamaterials

Beam steering antennas can also be realized using metematerials (MTMs). MTMs are materials which are artificially synthesized to have unique EM characteristics. One of the unique characteristics is that they have negative values both on the effective permittivity and permeability under specific conditions. MTMs were firstly demonstrated in 2001 using thin wires and split ring resonators (TW-SRR). However, due to the resonant nature, they suffered from narrow bandwidth, high loss and fabrication difficulties, which limits the application in microwave engineering.

Apart from the TW-SRR type, composite right/left-handed transmission Lines (CRLH-TLs) are more practical approaches. They are also MTMs based on a transmission line operated in the fundamental mode. The CRLH-TLs are made up with additional series capacitance (C_L) and shunt inductance (L_L) other than unavoidable series inductance (L_R) and shunt capacitance (C_R) as described in Figure 4.1(a). The series resistance and the shunt conductance are ignored in the figure. Figure 4.1(b) shows the $\omega - \beta$ dispersion diagram of the CRLH-TL. ω is the operating frequency and β is the phase

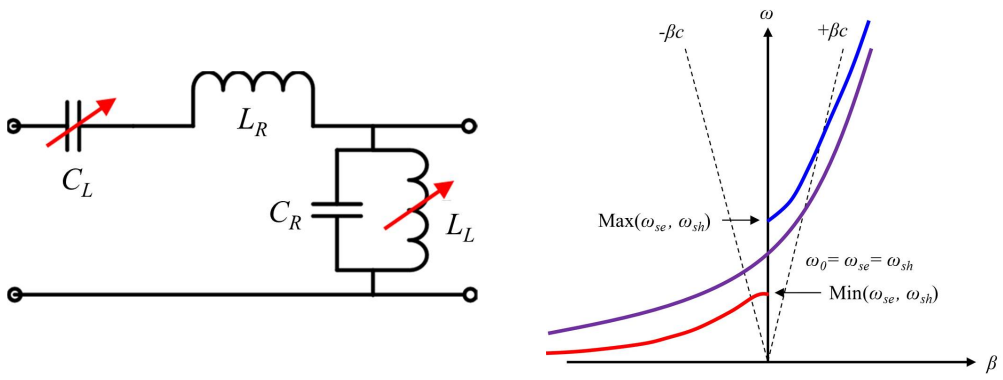

(a) Equivalent circuit representation

(b) Dispersion diagram

Figure 4.1: Composite Right/Left-Handed Transmission Line (CRLH-TL)

constant. The ω_{sh} and ω_{se} are given as

$$\omega_{sh} = \frac{1}{\sqrt{L_L C_R}}, \tag{4.1}$$

$$\omega_{se} = \frac{1}{\sqrt{L_R C_L}}. \tag{4.2}$$

It is investigated that, unlike the normal transmission line (so called right-handed TL), the phase constant β can be zero and even negative. The dispersion diagram in Figure 4.1(b) describes the β variance according to the frequency change for the EM signal flowing through the CRLH-TL. At the lower frequency, β is negative (LH region) and increased to a positive value at higher frequencies (RH region). For the case when $\omega_{sh} = \omega_{se}$, the CRLH-TL has the continuous β transition at the LH-RH changing position, which is called the balanced condition.

Together with the CRLH-TL, another significant design concept to realize beam steerability is to use a leaky wave antenna (LWA) principle. An LWA is a kind of waveguiding structure which possesses a mechanism that permits power leakage all along its length. It progressively radiates power along the longitudinal direction of the LWA. It is not a resonating structure and, therefore, the antenna size is not decided by the operating frequency. Its length determines the directivity of the beam. The LWA makes leakage radiation when the wave is faster than the light speed ($v_p > c$, fast wave). In other words, the radiating condition of the LWA is $\beta < k_0$ or $\omega > \beta c$. v_p and k_0 are the phase velocity and the freespace wavenumber.

In LWA, the radiating direction is determined by the phase constant of the propagating wave. The beam firing direction θ_m is calculated as

$$\sin\theta_m = \frac{\beta}{k_0}. \tag{4.3}$$

Figure 4.2 shows a schematic drawing of a leaky wave antenna using CRLH-TLs. A conventional LWA can radiate beams only to the forward direction ($0° < \theta_m < 90°$), because its phase constant β is limited to positive values. However, the LWA using CRLH-TLs can steer beams even to backward and broadside direction as well as to forward direction ($-90° < \theta_m < 90°$). CRLH-TL LWAs have a broad phase constant varying range in the fast wave radiation range ($|\beta| < k_0$) [Volakis, 2007; Caloz and Itoh, 2006].

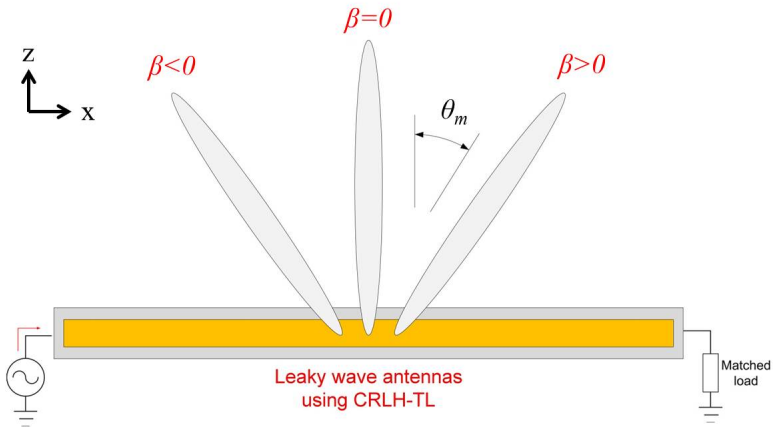

Figure 4.2: Leaky wave antenna using CRLH-TLs

4.2 LWA using CRLH-TL and RF MEMS

The main drawback of a CRLH-TL based LWA is that the phase constant is a function of frequency. The main beam direction is decided according to the frequency. In many cases, this is unsuitable for the practical beam steering antennas since the operating frequency is usually preset to a certain value and fixed during operation.

The representative solution to get over this drawback is to change the reactive loads of the CRLH-TLs, which is normally done by using variable solid state devices. However, in many cases, the solid state devices consume high power. They are lossy and non-linear at mm-wave frequencies [Lim et al., 2004; Nguyen et al., 2007; Albani et al., 2007; Matsuzawa et al., 2006]. This work discusses RF MEMS as the reactive component controlling technology using its advantages over solid state counter parts. In this chapter, a beam steerable LWA using CRLH-TLs is discussed, which adopts RF MEMS devices to tune the reactive loads of the CRLH-TL.

4.2.1 Tunable balanced CRLH-TL

For an LWA use, the CRLH-TL should be balanced. The 'balanced' condition means the dispersion curve transition shows a seamless profile at $\beta = 0$. That is to say, $\omega_{sh} = \omega_{se}$ is fulfilled and there is no stop band (see Figure 4.1(b)). In addition to that, the CRLH-TL is to be impedance matched. Generally, the CRLH-TL is only matched in a restricted frequency band. However, it can be matched over an infinite bandwidth when

$$Z_0 = Z_R = Z_L \tag{4.4}$$

is fulfilled. Z_0 is the line impedance. The CRLH-TL in Figure 4.1(a) can be decomposed into purely right-handed (PRH) and purely left-handed (PLH) representations as

described in Figure 4.3. The PRH impedance Z_R and PLH impedance Z_L are given as

$$Z_R = \sqrt{\frac{L_R}{C_R}}, \tag{4.5}$$

$$Z_L = \sqrt{\frac{L_L}{C_L}}. \tag{4.6}$$

It is investigated that the conditions Eq.(4.4), Eq.(4.5), Eq.(4.6) also allow the balanced condition ($\omega_{sh} = \omega_{se}$) by Eq.(4.1) and Eq.(4.2) at the same time. After the matching condition is fulfilled, the CRLH-TL is already balanced and vice versa. Since the line impedance Z_0 is fixed and the balanced frequency ω_0 is given, the design process is to construct the structure which has proper L_R, C_R, L_L and C_L for the desired Z_0 and ω_0.

For the LWA use, it is strongly preferred to make the CRLH-TL be balanced and matched regardless of the reactive component tuning. This means, the balanced dispersion curve will be vertically shifted along with the tuning state. However, this is not easily achieved by simple single reactive component tuning, because the reactive components L_R, C_R, L_L and C_L are closely correlated to each other by the matching and the balancing conditions. Once one reactive component is tuned, the CRLH-TL (which was initially balanced) is no longer matched and balanced. It is investigated that at least two reactive loading parameters should be simultaneously tuned for matching and balancing.

In this work, series capacitance (C_L) and shunt inductance (L_L) are selected as the tuning components. The tuning is done by a tunable interdigital capacitor and a stub inductor. The series inductance (L_R) and the shunt capacitance (C_R) are mainly contributed by parasitic components which are not easily controlled. However, C_L and L_L are artificially inserted components which are rather easily controlled compared to L_R and C_R.

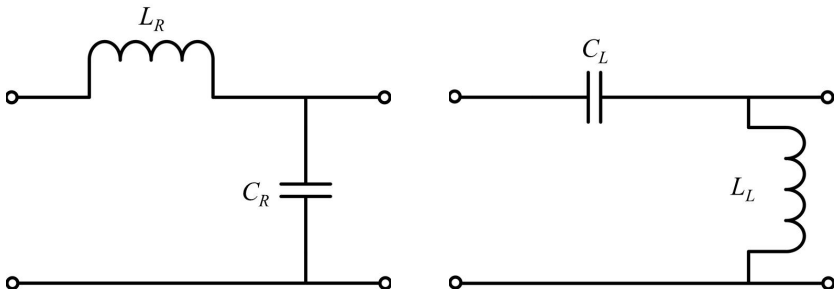

(a) PRH (b) PLH

Figure 4.3: CRLH-TL decomposition into PRH and PLH

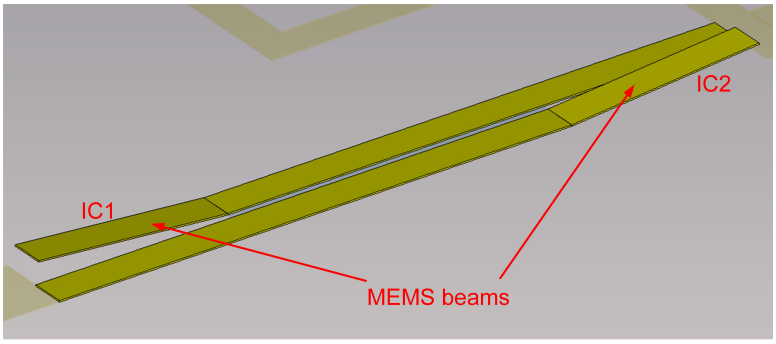

(a) Tunable interdigital capacitor

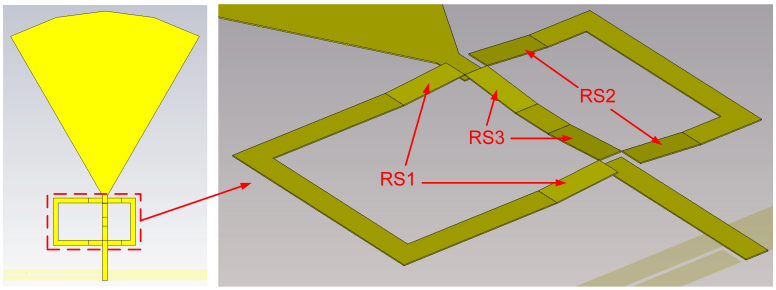

(b) Tunable stub inductor using radial stub

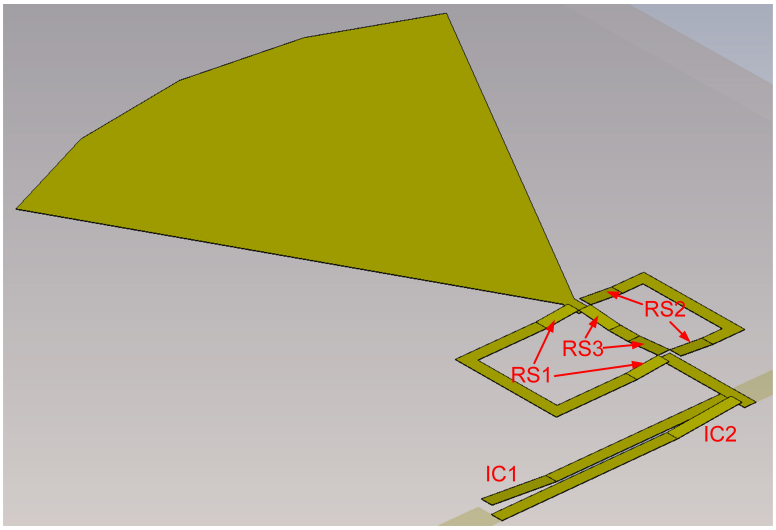

(c) Assembled CRLH unit cell

Figure 4.4: Tunable CRLH-TL cell [Kim and Vietzorreck, 2011]

Figure 4.4(a) shows a tunable interdigital capacitor by MEMS beams. The tunable capacitor can tune a series capacitance (C_L) to one of the three states according to the MEMS beam position. When the beam is down, the finger is more coupled with the neighboring finger, which increases C_L. The shunt inductance (L_L) tuning is by the tunable stub inductor which is depicted in Figure 4.4(b). The inductance is related to the stub length. RF MEMS switches (RS1, RS2, RS3) control the stub length, which leads to a shunt inductance variance. A radial stub is used for cost-effective grounding without via construction. Compared to a uniform line $\lambda/4$ extension, the radial stub is more broadband. In Figure 4.4(b), one of the switches (RS1, RS2, RS3) is ON whereas others are OFF, and, therefore, three values of L_L can be realized. Figure 4.4(c) is to show the assembled tunable CRLH-TL cell. According to the control signal, the RF MEMS components are assigned by three states as shown in Table 4.1. Each state is designed to be impedance matched and balanced.

State	**IC1**	**IC2**	**RS1**	**RS2**	**RS3**
State 1	Down	Down	On	Off	Off
State 2	Up	Down	Off	On	Off
State 3	Up	Up	Off	Off	On

Table 4.1: Beam/Switch state assignment [Kim and Vietzorreck, 2011]

Figure 4.5(a) shows the simulated S_{21} for the three states. It is shown that the frequency, at which the phase is 0°, is shifted to 7.3 GHz, 8.2 GHz and 9.6 GHz. These are the transition frequencies between LH and RH regions. A deeper investigation of the LH-RH transition is feasible by discussing dispersion curves calculated by ABCD parameters. For the reciprocal network with physical length p, the propagation constant γ is given as

$$\gamma = \alpha + j\beta = \frac{1}{p}\cosh^{-1}\frac{A+D}{2}. \tag{4.7}$$

The imaginary part of Eq.(4.7) corresponds to the phase constant β. Figure 4.5(b) shows calculated dispersion curves. The three curves are from each state assigned by reactive load tuning. Around 8 GHz, it is investigated that the wave of State 1 propagates forward ($\beta > 0$) and State 3 backward ($\beta < 0$). The wave of State 2 stays at the same position ($\beta = 0$). This means, β of the CLRH-TL is controlled by simple reactive load tuning at the fixed frequency. Regardless of the tuning, they are still balanced and impedance matched as desired [Pozar, 2005].

Strictly speaking, the CRLH-TL is slightly unbalanced as depicted in Figure 4.5(b). This is mainly due to the reactive load changes due to the component couplings which should be taken into account through the optimization using full wave simulation. However, the balanced condition is most critical on State 2 where the operating position is $\beta = 0$. The other cases are relatively relaxed. It is investigated that the dispersion curve

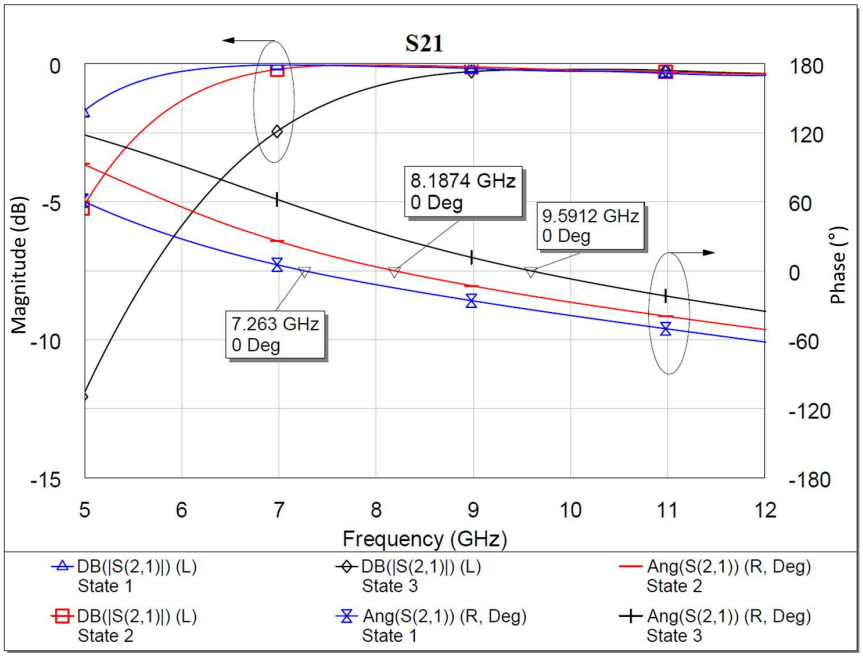

(a) S_{21} of the tunable CRLH-TL cell (simulated by CST [Computer Simulation Technology GmbH, 2010])

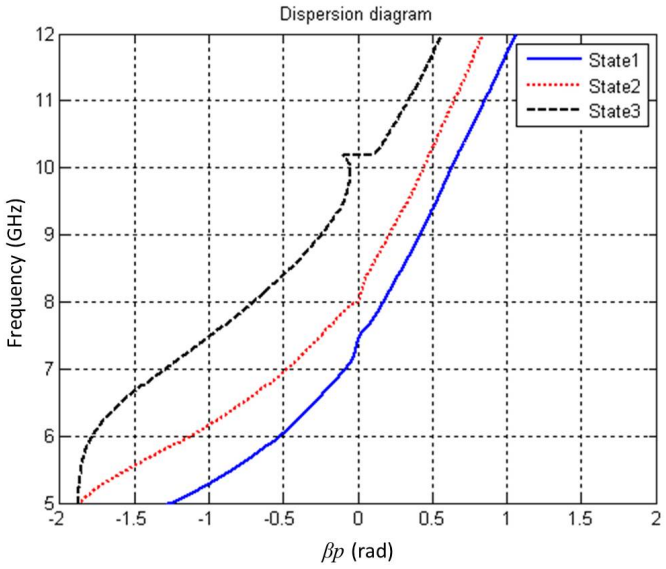

(b) Dispersion diagram of the tunable CRLH-TL cell (calculated and drawn by MATLAB [The MathWorks, Inc., 2010])

Figure 4.5: Simulated S_{21} and dispersion diagram of the tunable CRLH-TL cell [Kim and Vietzorreck, 2011]

of State 2 in Figure 4.5(b) is most seamless [Kim and Vietzorreck, 2011].

4.2.2 LWA using tunable balanced CRLH-TL

Figure 4.6 shows LWA using tunable RF MEMS CRLH-TLs. It is constructed by cascading CRLH-TL cells as shown in Figure 4.4(c). The presented LWA is a uniform type where its cross section is invariant or continuously tapered along the longitudinal direction. In the LWA, the traveling wave's characteristics along the aperture are decided by the leakage constant α and the phase constant β as a function of the longitudinal position. α means the leaked (radiated) power per unit length. An aperture is formed by

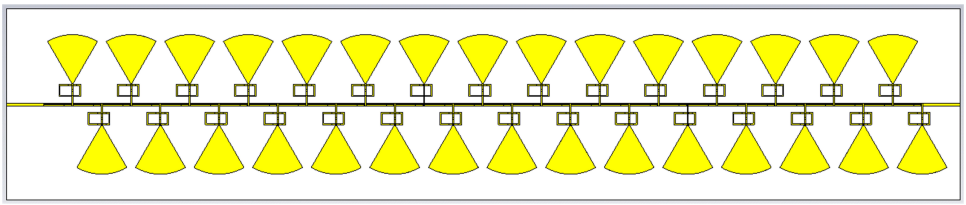

(a) Leaky wave antenna by cascading tunable CRLH-TL cells

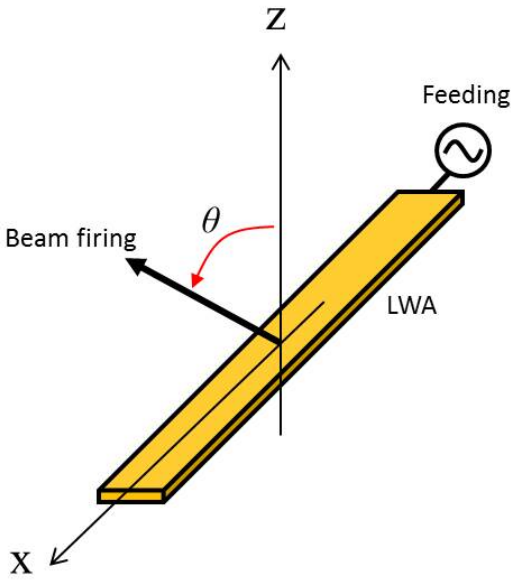

(b) Antenna feeding position and the definition of beam radiation angle θ

Figure 4.6: Leaky wave antenna using CRLH-TLs and RF MEMS

the antenna length L. The large aperture L with the uniform phase constant β generally obtains high directivity. The leakage constant α is mainly relevant to the beam shape [Volakis, 2007].

As shown in Figure 4.6(b), the LWA is fed from the antenna edge and the applied power travels along the antenna on radiating power. Practically, the LWA length L is decided so that the applied power is radiated by about 90%, which corresponds to

$$\frac{L}{\lambda_0} \approx \frac{0.18}{\alpha/k_0}. \tag{4.8}$$

The remaining 10% is dissipated by a matched load. Considering a typical ratio $\alpha/k_0 = 0.02$ and 8 GHz operation, the LWA would be 33.75 cm long. This is a much larger radiation aperture compared to the resonant type antenna, which yields high directivity. The EM structure in Figure 4.6 is to verify the LWA functionality. It consists of 30 CLRH-TL cells and is 4.7 cm long in total. Practically, the LWA length will be determined according to the substrate size.

Figure 4.7 shows the simulated LWA far-field radiation according to the three CRLH-TL states. The simulation is done by ADS Momentum [Keysight Technologies, 2009] and the depicted patterns show the E-field radiation under normalized option. It is investigated that the LWA beam firing direction is changed according to the CRLH-TL state (see Table 4.1). Reactive components change make the phase constant β change and the changed β steers the main beam radiation angle θ_m (see Eq.(4.3)). The beam radiation angle θ is defined as the angle between a beam firing direction and the line perpendicular to the LWA surface. In Figure 4.7 and Figure 4.8, θ has been defined on the z-x plane as shown in Figure 4.6(b). Figure 4.7(a) and Figure 4.7(b) depict the backfiring where the phase constant β is negative and the broadside firing with $\beta = 0$, which is impossible in a conventional LWA. Figure 4.8 depicts E-field radiation patterns according to the radiation angle θ, which are normalized by the main lobe level. It is also shown that the backfiring angle is about -15°. The forward firing angle is around 20°.

In Figure 4.7 and Figure 4.8, it is investigated that the sidelobe level is relatively high compared to the main lobe (65% to 85% of the main lobe level). This is mainly due to the nature of the perfectly uniform leaky wave structure. Since an exponentially decaying power along the line makes a high side lobe level, an optimal tapering technique is generally required to suppress side lobes. The tapering is focused to design an optimal α profile along the line, which leads to minimum side lobe levels on keeping β as invariant as possible. In this work, the tapering technique is not used due to the difficulty of the CRLH-TL cell's reactive components control on each position.

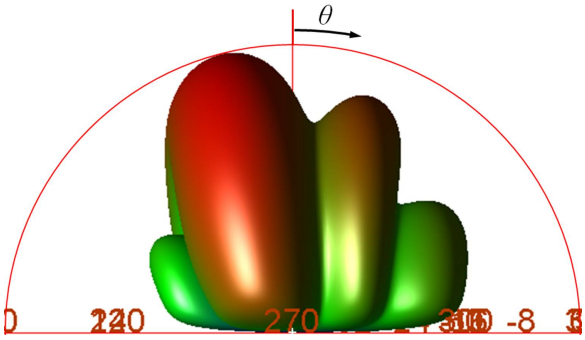

(a) State 3 (Backward)

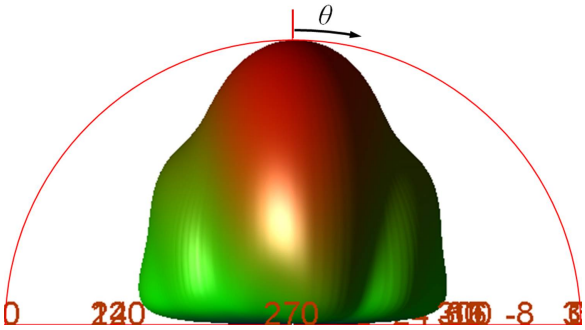

(b) State 2 (Broadside)

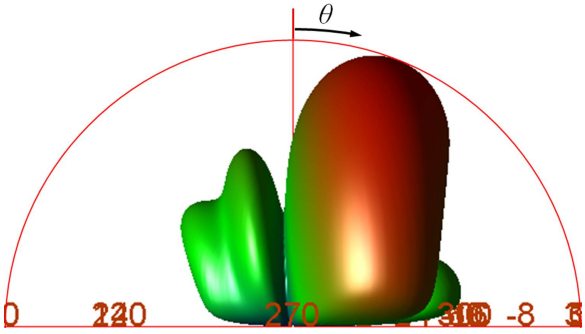

(c) State 1 (Forward)

Figure 4.7: Normalized E-field radiation pattern according to the state (simulated by ADS Momentum) [Keysight Technologies, 2009; Kim and Vietzorreck, 2013]

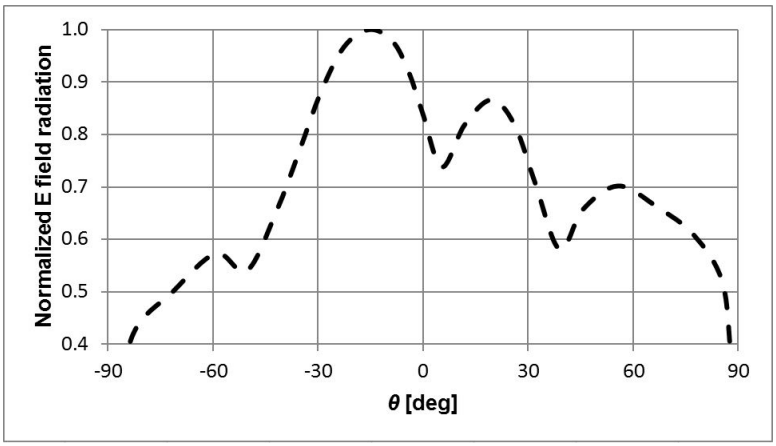

(a) State 3 (Backward)

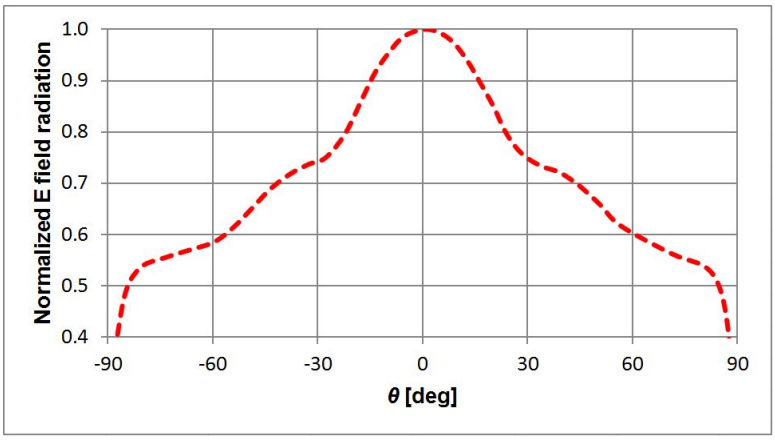

(b) State 2 (Broadside)

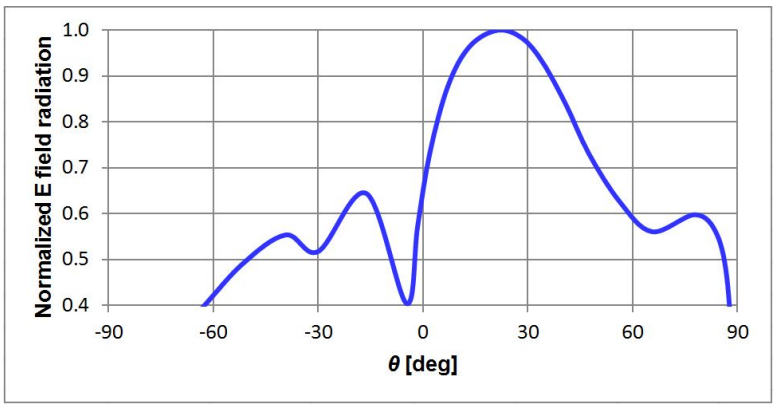

(c) State 1 (Forward)

Figure 4.8: Normalized E-field radiation pattern according to the radiation angle θ

What is also remarkable is, since its transversal aperture is very small, the LWA fires a 'fan beam', narrow in the longitudinal plane and wide in transversal. In addition to that, it is also possible to realize a 2D beam steerable antenna by combining CLRH-TL LWA with phase shifters. Figure 4.9 explains the beam steering concept. The horizontal steering is done by the CRLH-TL LWAs and vertical steering is done by phase shifters connected on the LWA feeds. Of course, the 2D beam steering is also feasible by using several phase shifters without LWAs. However, the feeding network construction is complicated and generally needs complex multi-layered structures. The LWA demonstrated in Figure 4.9 can be realized by simple surface micromachining, which is more easy and cost-effective [Caloz and Itoh, 2006; Kim and Vietzorreck, 2012, 2013].

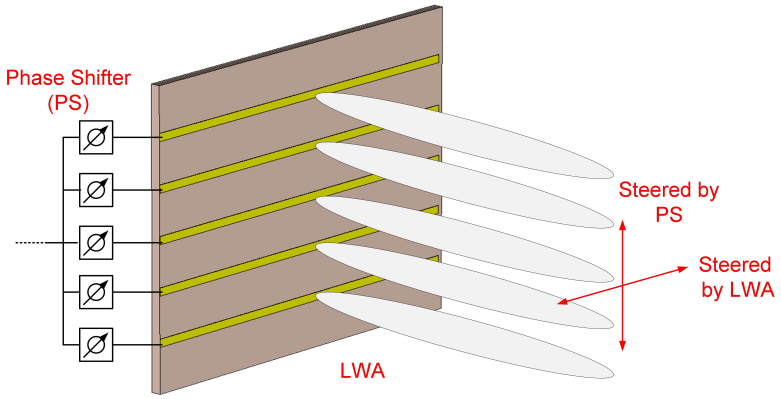

Figure 4.9: 2D beam steerable antenna using LWA and phase shifters

4.2.3 Test structure fabrication and measurement

The LWA in the work consists of several CRLH-TL cells. Therefore, the design process starts from the single CRLH-TL cell design. The test structures in Figure 4.10 are to verify a functionality of the CRLH-TL cell in Figure 4.4(c). In the test structure, the RF MEMS components have been replaced with electromagnetically equivalent fixed planar structures. They were fabricated on the dielectric substrate using an in house laser circuit pattern generator at TUM. De-embedding structures have also been fabricated for TRL calibration.

Figure 4.11 and Figure 4.12 show measured/simulated S_{21} and dispersion curves. The simulations have been done by ADS Momentum and the dispersion curves have been generated by MATLAB [Keysight Technologies, 2009; The MathWorks, Inc., 2010]. It is investigated that the dispersion curves in Figure 4.12 are not well-matched with the simulation. A possible reason would be that the laser cutter doesn't make exact patterns with enough resolution. It is inspected that metals between interdigital capacitor fingers are not completely removed for some positions, which makes C_L higher. A possible solution to improve fabrication quality is to use less critical circuit resolution (ex. $50\,\mu\text{m} \rightarrow 100\,\mu\text{m}$) and redesign cells according to the new resolution. Another source of error would be dielectric substrate property deviations. It might happen that the actual substrate property would be different from the simulation. But for whatever reason, balanced CRLH-TLs are tricky to realize, since even a small error of the reactive component easily breaks the balancing conditions. Several test structures would be required to have exact balancing conditions.

However, Figure 4.12(b) still shows that the CRLH-TL tuning is possible by using a reactive components control. Even though the CRLH-TLs are unbalanced, their dispersion curves are tuned according to the reactive components change. After balancing, the cell can be used for the beam steerable LWA construction [Kim and Vietzorreck, 2013].

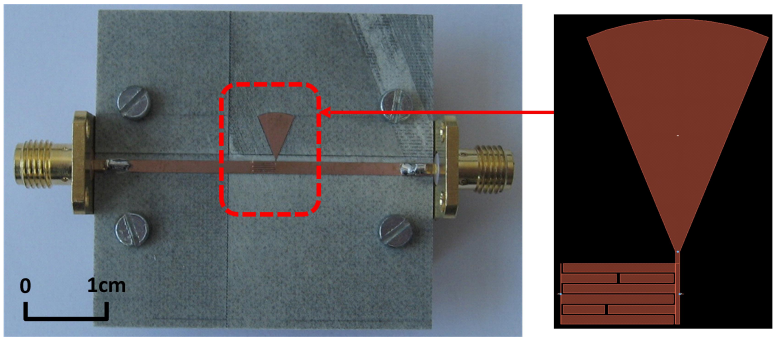

(a) Backward

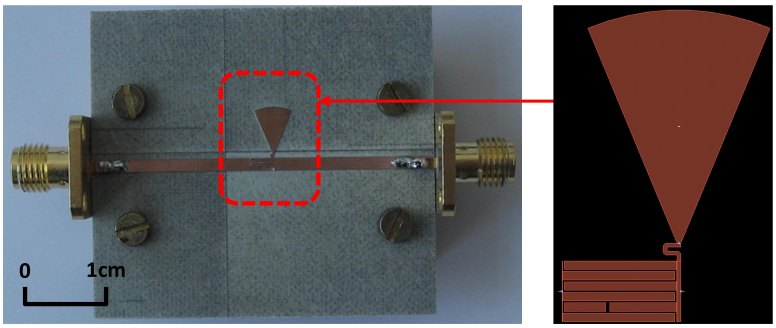

(b) Broadside

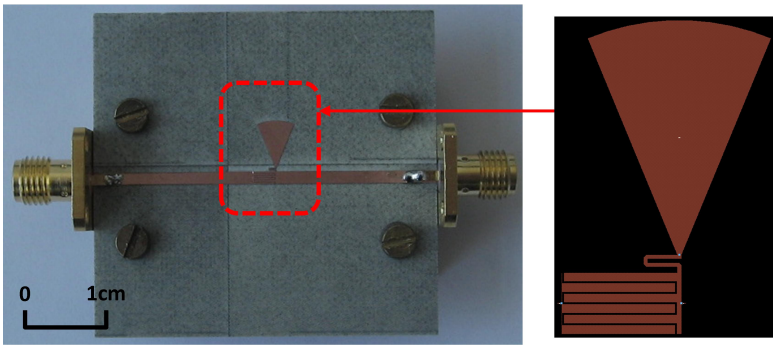

(c) Forward

Figure 4.10: CRLH-TL cell test structure

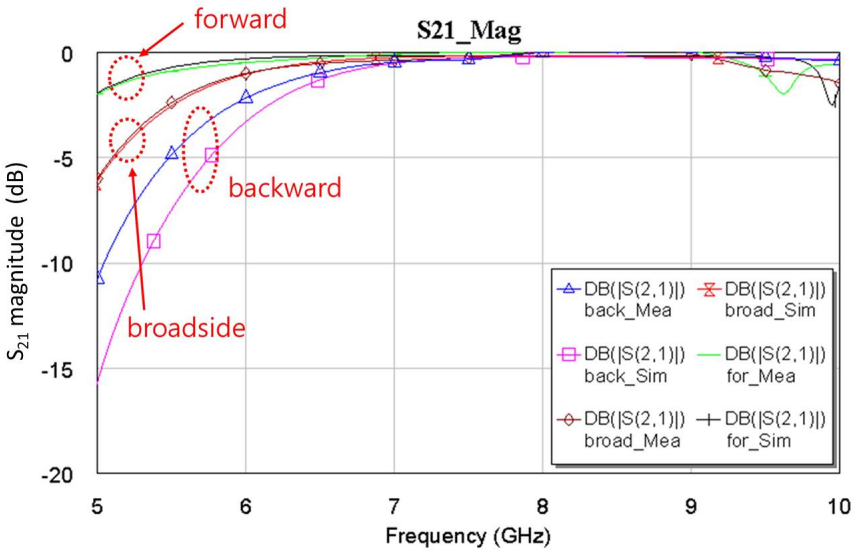

(a) S_{21} Magnitude

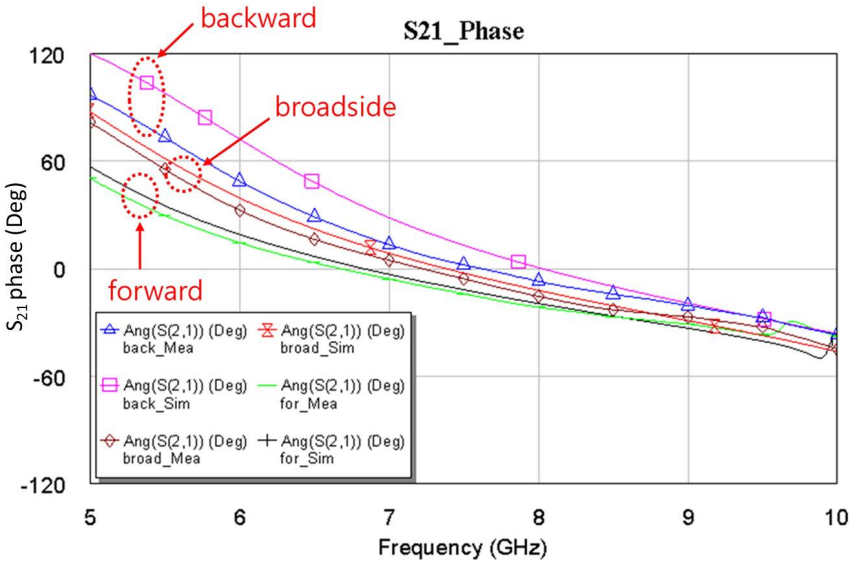

(b) S_{21} Phase

Figure 4.11: Comparison between S_{21} measurement and simulation (simulated by ADS Momentum [Keysight Technologies, 2009])

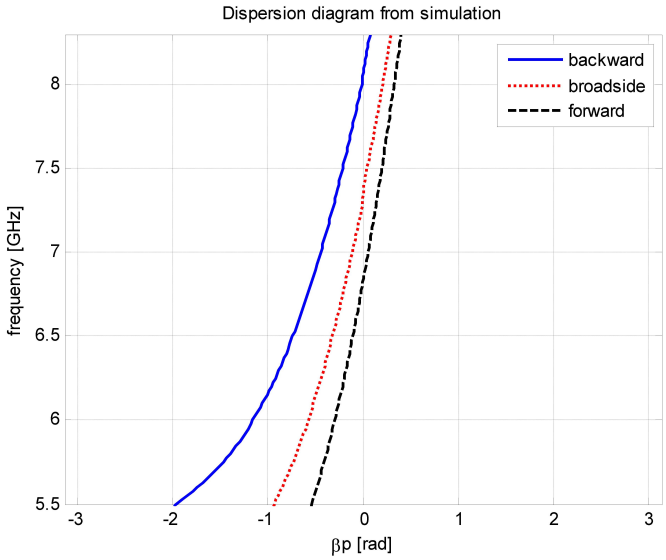

(a) Simulation

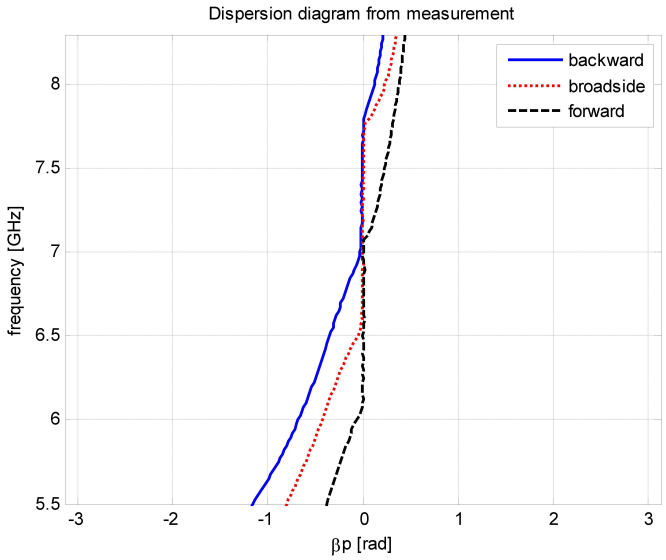

(b) Measurement

Figure 4.12: Dispersion diagram of the CRLH-TL cell as shown in Figure 4.10

Figure 4.13 shows the LWA fabricated for the testing purpose. It consists of 30 CRLH-TL cells shown in Figure 4.10(b) which is for the broad side beam firing. The feed line is connected by a K-connector and the other port is terminated by a matched load to avoid reflection. Practically, the balanced CRLH-TL cell becomes unbalanced after being cascaded due to the coupling between the cells. Therefore, an additional balancing process should follow on cascading cells.

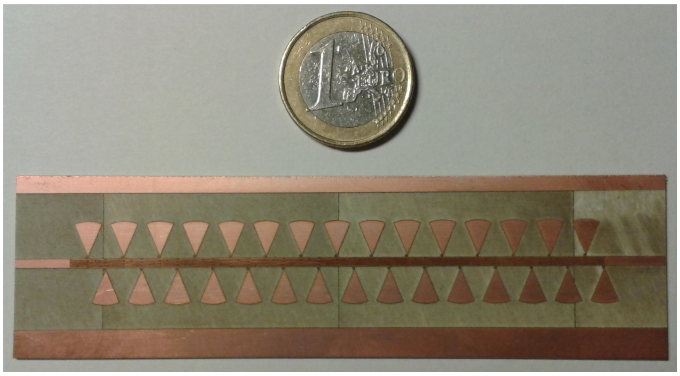

Figure 4.13: Fabricated LWA using CRLH-TLs

4.2.4 2D beam steerable LWA

Figure 4.14 shows a feasibility study of the 2D beam steerable antenna in Figure 4.9. They are fixed test structures assuming in-house laser cutter fabrication. As discussed, phase shifters vertically steer the beam firing direction and horizontal beam firing directions are controlled by beam steerable LWAs. To represent the phase shifter, feeding structures consisting of power dividers and quarterwave transformers have been designed. The RF signal fed from Port 1 is divided and the phase shifted signals are applied to the 4 LWA feeds accordingly. The phase shifts are decided according to the electrical length difference between input and LWA feeding reference planes. The phase difference $\Delta\Phi$ between neighboring LWAs is given by

$$\Delta\Phi = \frac{2\pi}{\lambda_0} d \sin\theta. \tag{4.9}$$

d is the distance between neighboring LWAs and λ_0 is the free space wavelength. The phase shifters in Figure 4.15 make 90° phase difference at the LWA feeds ($\Delta\Phi = 90°$). The distance between the LWAs is decided considering the side lobes suppression. The side lobes decrease the power and antenna gain. They also introduce undesired signals and noise. For the LWA distance d,

$$\frac{d}{\lambda_0} < \frac{1}{1 + \sin\theta_{max}} \tag{4.10}$$

should be fulfilled in terms of the desired maximum scan angle θ_{max} [Volakis, 2007]. In this work, the distance between LWAs is decided as 2 cm. Considering the given phase shift $\Delta\Phi$ and distance d, the beam firing is vertically steered by around 30° at the operating frequency.

What is shown in Figure 4.15 are the simulated far-field radiation patterns according to the azimuth angle φ (see Figure 4.14(b)). The depicted E field patterns have been simulated by ADS Momentum under normalized option [Keysight Technologies, 2009]. Figure 4.15(a) and (b) show the beam pattern for the forward/upward firing. In this case, the phase constant of the LWA is positive ($\beta > 0$) and the phase of the bottom LWA is advanced compared to the top LWA's phase. The main beam direction is around 50° in azimuths ($\varphi = 50°$). Figure 4.15(c),(d) show the backward/upward beam firing, which the main beam is fired to 125° in azimuths ($\varphi = 125°$). It is also investigated that the maximum side lobe levels are around 75% to 85% of the main lobe levels.

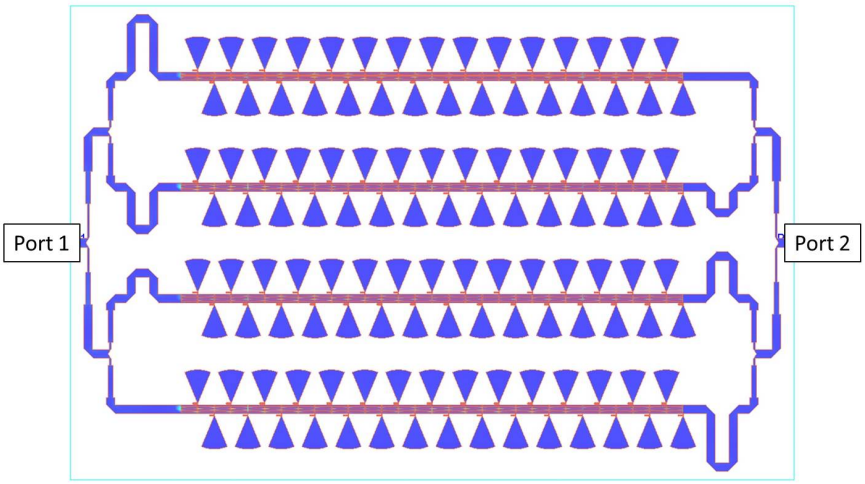

(a) 2D beam steering antenna

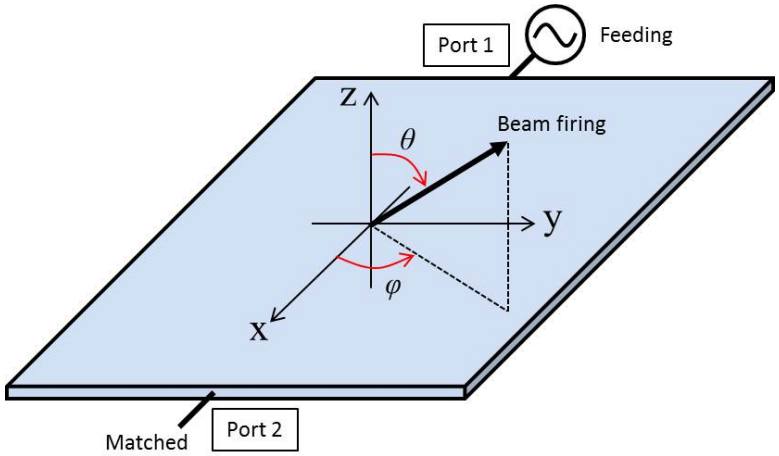

(b) Antenna feeding

Figure 4.14: 2D beam steering antenna design

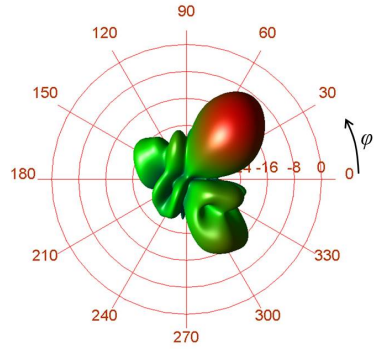

(a) Beam (Forward/Upward)

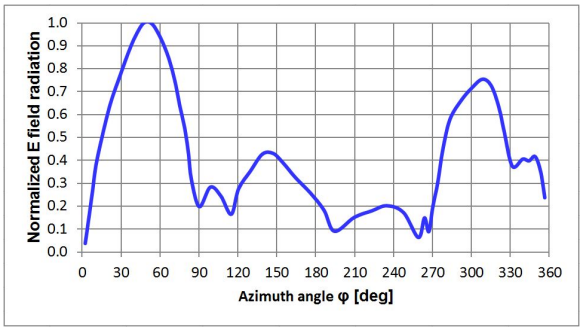

(b) Normalized E field (Forward/Upward)

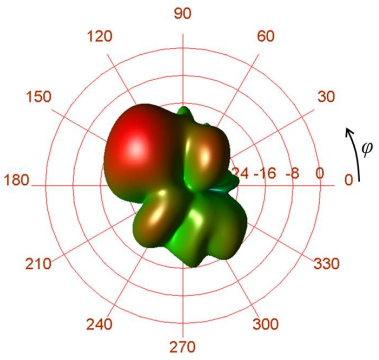

(c) Beam (Backward/Upward)

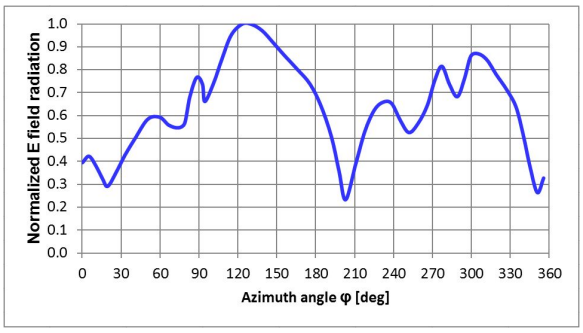

(d) Normalized E field (Backward/Upward)

Figure 4.15: Simulated E field radiation pattern of 2D beam steerable antenna (simulated by ADS Momentum [Keysight Technologies, 2009])

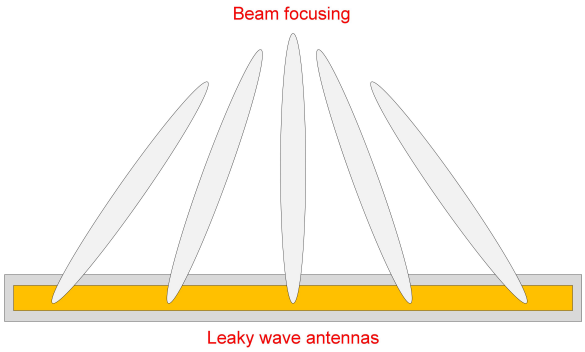

Figure 4.16: Beam focusing of the LWA using CRLH-TLs

4.3 Conclusion

A conventional LWA only provides forward beam firing (end-firing) due to the phase constant β variation limit. Adopting CRLH-TLs, the presented LWA can realize backward and broadside beam firing. This is because the CRLH-TL can realize negative β as well as zero phase constant. For non-tunable LWAs, the beam firing direction is frequency dependent, which is not suitable because the operating frequency is generally fixed. It is possible to realize a frequency-fixed beam steerable LWA using RF MEMS technology. RF MEMS devices tune the reactive components of the CRLH-TL and vertically shift its dispersion curve on keeping a balanced condition. Therefore, the presented LWA can steer main beam direction from backward to forward at a fixed frequency. In this work, the design of a beam steerable LWA is demonstrated and the CRLH-TL cell test structures have been fabricated and measured to verify the functionality. Test structures of the 2D beam steerable antenna are also designed. In the 2D beam steerable antenna, the beam is steered by phase shifting and phase constant β control.

Since lots of RF MEMS components should be simultaneously controlled, the LWA would need control electronics. The control electronic can be also used for beam focusing. As described in Figure 4.16, the fired beam can be focused by local β controlling, which increases the antenna directivity. Since the β should be smoothly changed, the corresponding RF MEMS components must be carefully controlled as well. The proposed beam-steerable antennas using CRLH-TL and RF MEMS technologies can be applicable in many areas, such as automotive radar, arbitrary shape antenna or in-flight entertainments (IFE) system, etc. The antenna will provide highly linear and low loss beam firing with high directivity.

5 RF MEMS Switch Design and Optimization using ANNs

5.1 RF MEMS switch modeling

In many cases, RF MEMS switches are modeled by 3D electromagnetic (EM) simulators using the finite integration technique (FIT) or the finite element method (FEM). The 3D EM simulators can simulate almost every EM structure. A 2.5D EM simulator using methods of moments (MoM) is also applicable. Since most RF MEMS switches have a high aspect ratio - large width compared to small thickness, the switch geometry can be described as a stack of multiple layers. However, since RF MEMS switches consist of many complicated thin structures, the 3D/2.5D EM simulation normally needs lots of simulation effort (time, computing resources, etc.). Moreover, the computing load is further increased when the switches should be optimized, which requires multiple simulations. A circuit simulation using equivalent circuit representations can be also usable. The circuit simulator uses mathematical models to represent RF properties of the RF MEMS switch. The models are generated by the measured/modeled S parameters or a lumped element circuit representation of the RF MEMS switches. The circuit simulator is fast and needs less simulation effort. However, it cannot represent components coupling during optimization and requires more complex lumped circuit representations for increasing structure complexity. Moreover, the direct relation between geometry and RF properties is usually missing.

RF MEMS switches are mechanically configurable RF switching components. They require mechanical modeling as well as EM modeling and these are normally correlated to each other. Mechanical properties contribute to the EM performance and vice verse. For instance, the bridge stiffness of the RF MEMS switches affect the actuation voltage. The bridge stiffness is decided by many mechanical properties, which can also influence EM properties. For the RF MEMS capacitive shunt switch, the shunt resonant frequency is significantly affected by the bridge length, which also determines the bridge stiffness. This means mechanical properties should be considered along with the EM properties, which requires multi-physics modeling. Conventional multi-physics modeling mostly adopts an iterative approach. For example, EM characteristics are firstly simulated and the mechanical state is simulated based on the EM state. Then another EM simulation is following from the given mechanical state and this process is repeatedly carried on until both states are converged on a certain level. However, it generally requires high

computing resources and state divergence should be carefully controlled.

An artificial neural network (ANN) can be a good solution to overcome these drawbacks. The ANN provides fast and efficient simulation capabilities with multiple input/output variable handling. The variables are not only limited to the RF circuit parameters but also include the mechanical properties. Once it is trained, the ANN can easily characterize the device properties and estimate the unknown properties with low computational effort, which is effectively used for device optimization. Additionally the ANN can be implemented to the circuit simulator block where the circuit representation is difficult due to the coupling or multi-physical parameter handling, etc. The ANN can be also used to find the initial parameter values for the optimization using 3D simulation, which decreases the total optimization resource [Kim et al., 2013b; Marinkovic et al., 2013].

5.2 Artificial Neural Network (ANN)

In the biological nerve system, a neuron processes information. As described in Figure 5.1(a), it consists of a soma, an axon and dendrites. The neuron receives information from the other neurons through dendrites and transmits a signal by using its axon. The signal transition between neurons is achieved by a synapse, the functional unit between one neuron's axon strand and a dendrite of another. At the synapse, specific chemical neurotransmitters are released and they enhance or inhibit the receptor neuron according to the synapse type. The effectiveness of the synapse is continually adjusted according to the passing signals. In other words, the synapse keeps learning from the participating activities, which is possibly relevant to the human memory. Through synapses, the neurons are connected to each other to form a massively complex and dense network. The network is like a parallel computer. When complicated information is entered, it

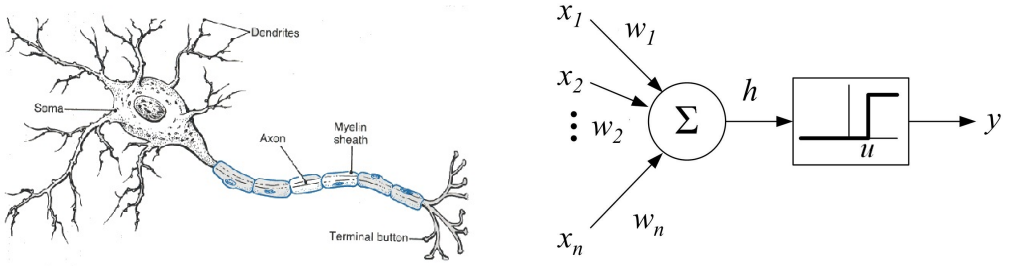

(a) Biological Neuron sketch [Carlson, 1992]

(b) McCulloch-Pitts model [McCulloch and Pitts, 1943]

Figure 5.1: Neuron and McCulloch-Pitts logical model

is divided into simple information and distributed, processed and the final outputs are generated [Carlson, 1992].

Artificial neural networks (ANNs) are the mathematical models inspired by the central nervous systems, brains for example. They describe some brain functions by computer simulation to perform machine learning, pattern recognition, forecasting or data compression, etc. The basic element of ANN is the neuron. They simply react according to the superposed outside stimulation. Like a biological neural network, the ANN consists of lots of neurons which are connected as a complicated network. As the computational representation of the neuron, McCulloch and Pitts suggested the logical model as shown in Figure 5.1(b). It calculates a weighted sum of the inputs $(x_1, x_2, ..., x_n)$ and computes y as 1 when the summation is above a specific threshold u, which is described as

$$y = U\left(\sum_{j=1}^{n} w_j x_j - u\right). \tag{5.1}$$

$U()$ is the unit step function and w_j is the synapse weight corresponding to the j^{th} input, which determines the excitatory or inhibitory synapses. Since the first model was proposed, the model has been further developed and generalized according to the function, topology, learning algorithms or hybrid constructions, etc. One remarkable variation is to use an activation function as well as a threshold function. The activation function adopts a piecewise linear, sigmoid or Gaussian function, etc. [McCulloch and Pitts, 1943; Jain et al., 1996]. The model in Figure 5.1(b) is connected as a complex network and mathematically combined to process information by ANNs as described in Figure 5.2. The figure shows a widely-used ANN which is called a multilayer perceptron (MLP) ANN. The MLP consists of input/output layers (layer 0, layer N_l) and multiple hidden layers (layer 1, ..., layer l). The connections between neurons are weighted as

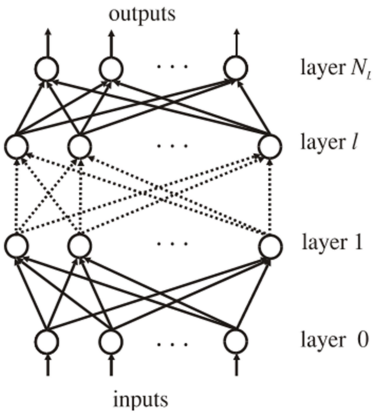

Figure 5.2: Multilayer Perceptron (MLP) ANN [Kim et al., 2013b]

noted in Figure 5.1(b). The aim of an ANN is to obtain the desired output for specific inputs, which is normally achieved by adjusting artificial neuron weights (w_j). The process of adjusting weights is called 'training' or 'learning'. However, for an ANN which has lots of neurons, it is very difficult to find proper weights in a manual way. Therefore, a special algorithm for training is required. One of the most common training algorithm is a backpropagation algorithm for a given set of input patterns with known classifications [Rumelhart and McClelland, 1986; Gershenson, 2003]. The output vectors are generated from the input vectors which is applied to the input neurons. The output vectors are compared to the desired value. Then the error derivatives are computed for each weight and biased until the whole training sets are processed to the network. The computed error derivatives also update the neuron weights and biases of the model. Generally, the termination condition for the ANN training is when the errors are less than the prescribed values or when the training process number is reached to the prescribed maximum number.

In this chapter, the feasibility of applying ANNs to design and optimize RF MEMS switches is discussed. The work has been carried out in a close collaboration with the ANN research group in the University of Niš, Serbia. The group in the University of Niš performs the ANN coding and simulation. The TUM group provides RF MEMS characteristics and takes part of the ANN model parameter definition.

5.3 RF MEMS switch modeling using ANN

5.3.1 Ohmic series switch modeling

Figure 5.3(a) shows the bridge type Ohmic series switch fabricated by the RF MEMS technology in FBK, Trento [DiNardo et al., 2006]. Figure 5.3(c) shows its cross section. When the bridge is down and touched to the Au bumpers, the switch is ON and transmits the RF signal. The bridge length L_s, bridge width W_s, gap L_g and W_g are the main design parameters. However, the bridge shape is too complicated to be described by four parameters. Therefore, in this work, a simplified structure is used for the ANN modeling and the simplified feature is described in Figure 5.3(b). The simplified structure is used to characterize the Ohmic series RF MEMS switch by the ANN modeling.

Figure 5.4 shows the ANN parameter definitions for the Ohmic series RF MEMS switch. In addition to the physical dimension L_s, W_s, L_g and W_g, the frequency f is also included in the input parameters. These five inputs are separately applied to the four ANNs and each ANN computes the magnitude and the phase of S_{11} and S_{21}. After the input/output parameters are defined, EM simulations are performed by CST Microwave Studio [Computer Simulation Technology GmbH, 2010] with various combinations of the input parameters, which is to generate ANN training sets. The training sets are decided on considering feasible input parameter sweeping ranges. The ANNs, depicted in Figure 5.4, consist of two hidden layers and the neuron numbers are independently determined through the training process considering their training performance.

Figure 5.5 and Figure 5.6 show the comparison between ANN and CST simulation results. The test set depicted in Figure 5.5 and Figure 5.6 is not included in the training set. It is investigated that the magnitude and the phase of the S_{11} and S_{21} show good agreement to the EM simulation results. In other words, in terms of the output accuracy,

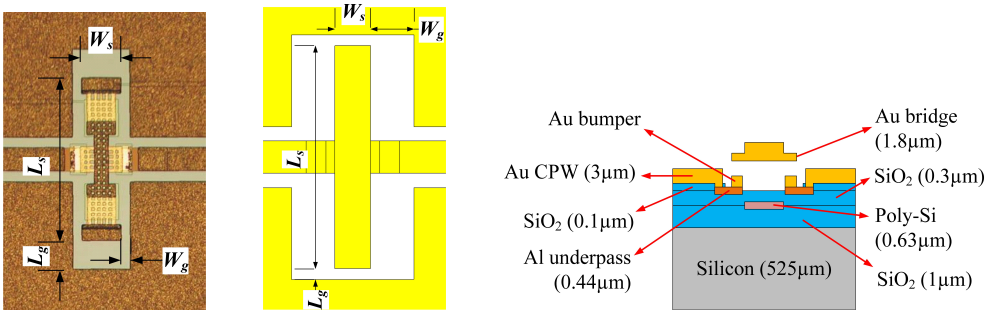

(a) Top view [DiNardo et al., 2006]

(b) Simplified

(c) Cross section schematic

Figure 5.3: Ohmic series switch

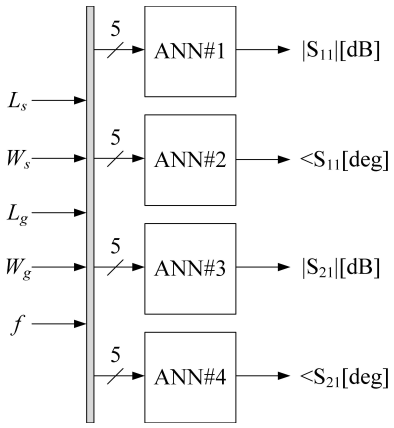

Figure 5.4: ANN parameter definition for the ohmic series switch modeling [Milijic et al., 2014]

the ANN can replace EM simulation. Moreover, the ANN simulation time is less than a second, which is much faster than the 3D simulator. It turns out that the ANN has an advantage of time consumption and computing effort compared to the EM simulation [Milijic et al., 2014].

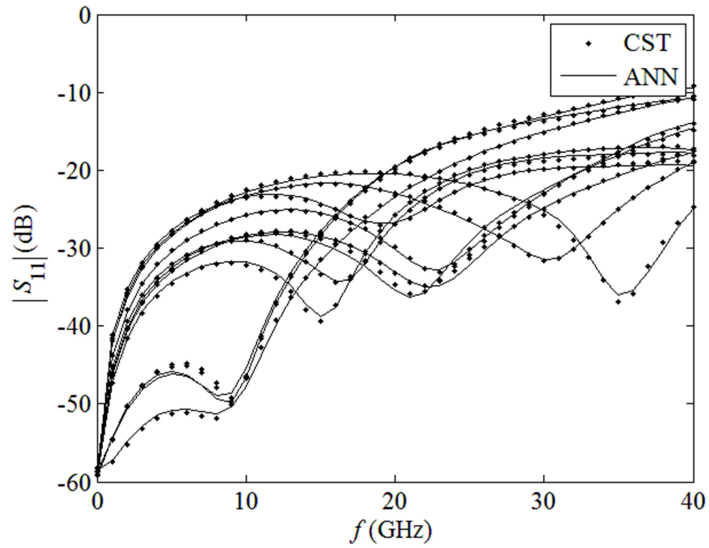

(a) $|S_{11}|$

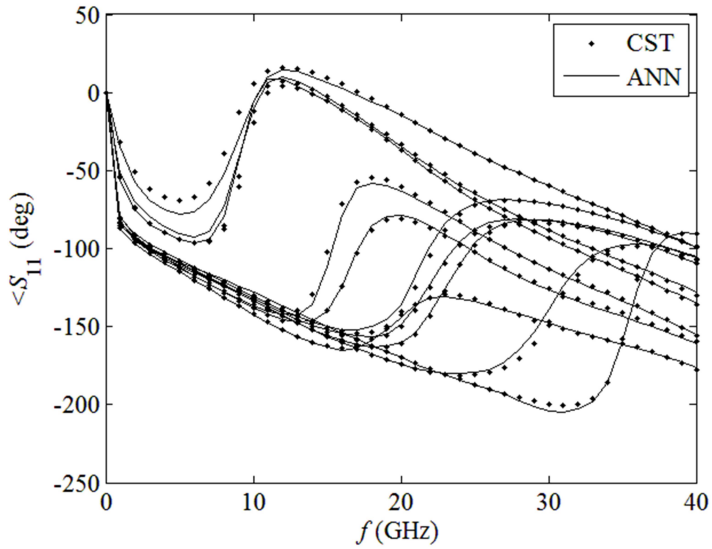

(b) $\angle S_{11}$

Figure 5.5: Simulated S_{11} of the Ohmic series switch (Figure 5.3) by ANN and CST [Milijic et al., 2014; Computer Simulation Technology GmbH, 2010]

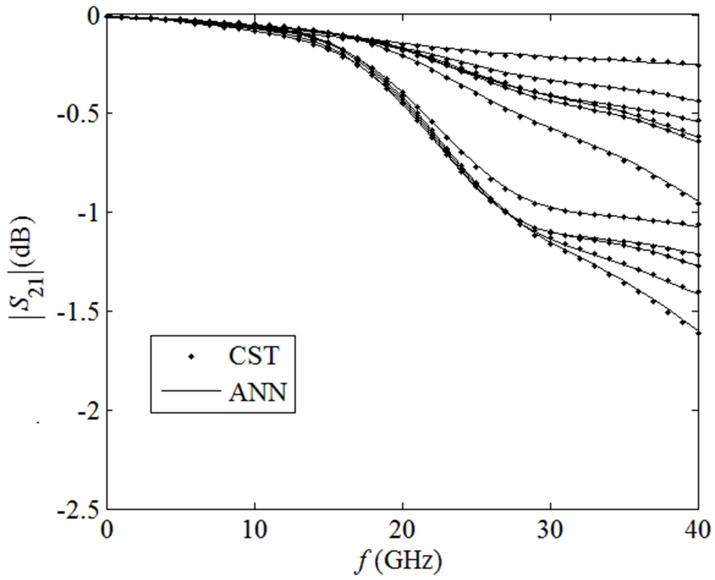

(a) $|S_{21}|$

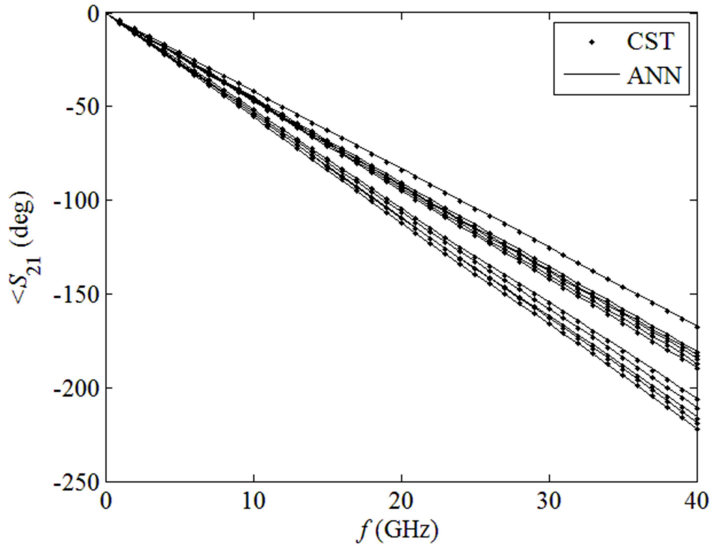

(b) $\angle S_{21}$

Figure 5.6: Simulated S_{21} of the Ohmic series switch (Figure 5.3) by ANN and CST [Milijic et al., 2014; Computer Simulation Technology GmbH, 2010]

5.3.2 Capacitive shunt switch modeling

Figure 5.7 depicts a capacitive shunt RF MEMS switch fabricated by FBK technology [DiNardo et al., 2006]. As shown in Figure 5.7(b), the switch consists of several complicated thin layers which require a high computing resource. This section shows the capacitive shunt RF MEMS switch modeling by ANNs.

5.3.2.1 Scattering parameter simulation

A scattering parameter simulation would be the one of the most interesting topics on the switch modeling. Figure 5.8 shows ANN input/output parameter definitions. The input parameters L_s and L_f correspond to the lengths of the solid and finger parts of

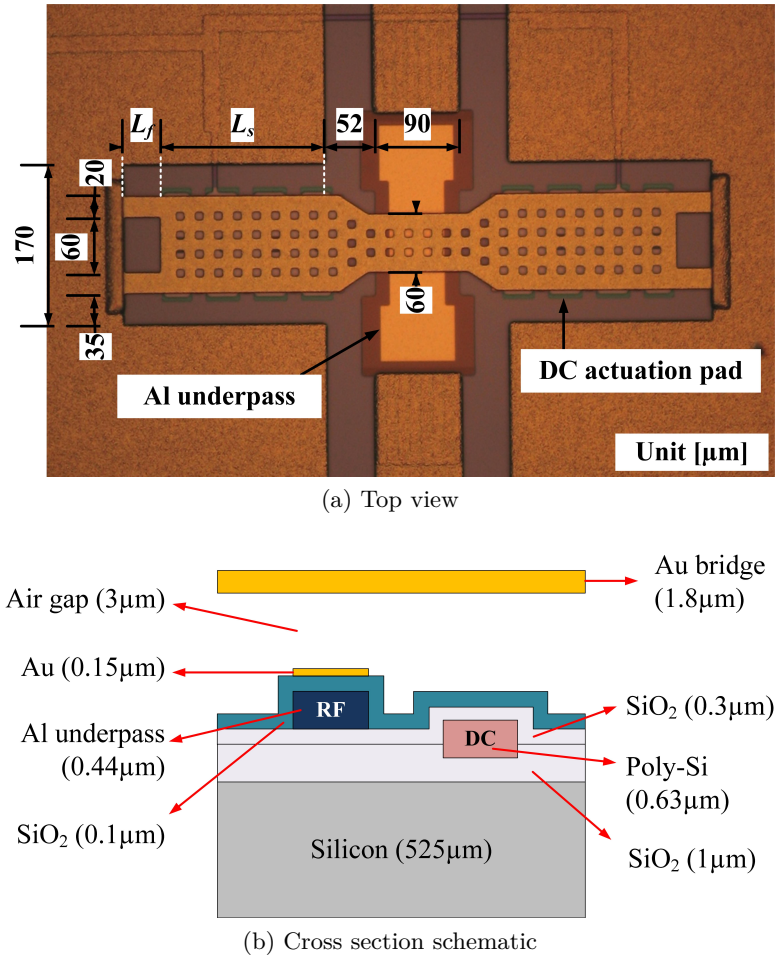

(a) Top view

(b) Cross section schematic

Figure 5.7: Capacitive shunt switch [DiNardo et al., 2006; Marinkovic et al., 2013]

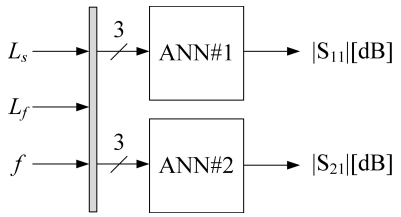

Figure 5.8: ANN parameter definition for scattering parameter modeling

the bridge as described in Figure 5.7(a). $|S_{11}|$ and $|S_{21}|$ are the output parameters. The training sets are generated by the ADS Momentum simulation [Keysight Technologies, 2009]. Figure 5.9 shows the simulated result using test sets which are not included to the training sets. The dot-line stands for the ADS simulation result and the solid lines are from ANN simulations. It is shown that the $|S_{11}|$ and $|S_{21}|$ by ANN simulation are quite in line with the ADS result. The ANN simulation can replace EM simulations for finding scattering parameters of the capacitive shunt RF MEMS switch. Generally, the ADS simulation takes several minutes, whereas the ANN simulation only needs 1-2 seconds. This is the remarkable advantage of the ANNs. This advantage becomes more significant when the switch should be optimized because the optimization process generally involves lots of simulation runs and needs much more computing resources.

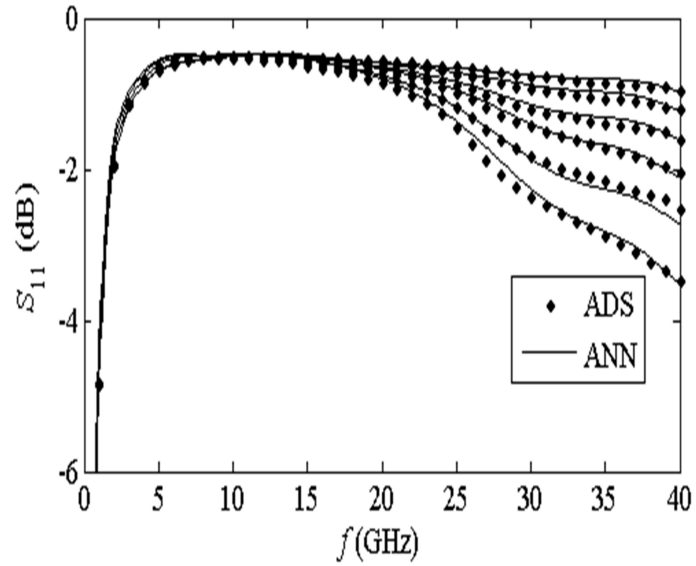

(a) $|S_{11}|$

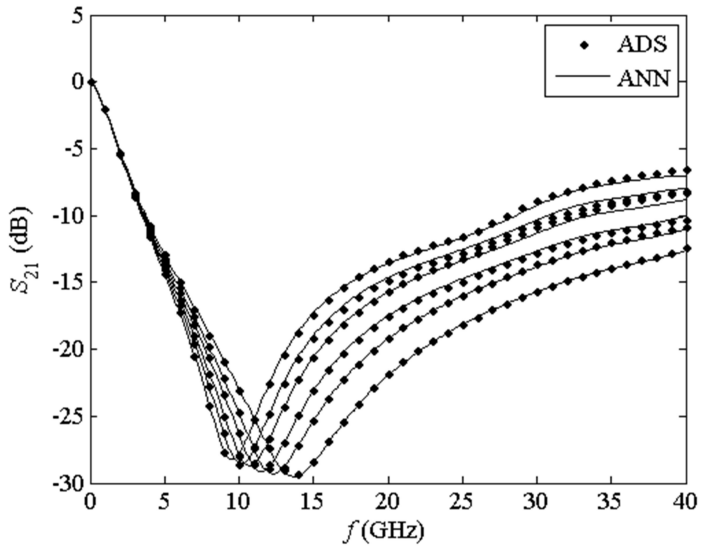

(b) $|S_{21}|$

Figure 5.9: Simulated scattering parameters of the capacitive shunt switch (Figure 5.7) by ANN and ADS [Kim et al., 2013b; Keysight Technologies, 2009]

5.3.2.2 Resonant frequency modeling

As discussed in Chapter 2, an RF MEMS capacitive shunt switch has a high OFF state isolation using a shunt resonance (see Figure 2.5 and Eq.(2.2)), which is mainly relevant to the bridge inductance L_b and the capacitance C_b between bridge and the CPW center line (see Figure 2.5). From Eq.(2.2), the shunt resonant frequency ω_{res} is given as

$$\omega_{res} = \frac{1}{\sqrt{L_b C_b}}. \tag{5.2}$$

The OFF state C_b is mainly determined by the bridge/centerline overlapping area and the dielectric layer thickness. The L_b corresponds to the bridge inductance which is determined by bridge length and width. Changing L_s, L_f strongly affects the bridge inductance L_b. The C_b and L_b are the main factors which decide the OFF state resonant frequency. The OFF state resonant frequency of the capacitive shunt switch is one of the key design parameters, which is normally found by EM simulation. However, if the resonant frequency is the only parameter of interest, it can be easily predicted by ANNs with a much lower computing effort.

Figure 5.10 shows the ANN input/output parameter definition. The two parameters L_s, L_f are used as ANN inputs and the output f_{res} is calculated. The ANN consists of three layers (input/output layer and one hidden layer) including five neurons. The ANN is trained by several training sets and the test sets are applied to the input vector of the ANNs.

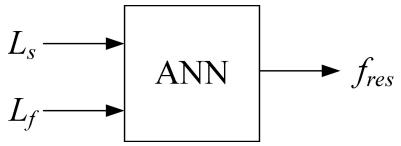

Figure 5.10: ANN parameters for resonant frequency modeling

Table 5.1 lists the ANN simulation results. A $f_{res|ANN}$ is the resonant frequency simulated be ANN and a $f_{res|ADS}$ is from the full wave simulation using ADS Momentum solver [Keysight Technologies, 2009]. It is shown that the ANN and ADS results show good agreement with less than 1% relative errors [Kim et al., 2013b].

L_s [μm]	L_f [μm]	$f_{res\|ANN}$ [GHz]	$f_{res\|ADS}$ [GHz]	Relative error [%]
250	25	13.7	13.689	0.08
250	75	12.4	12.403	0.02
350	25	11.6	11.550	0.43
350	75	10.7	10.638	0.58
450	25	10.2	10.127	0.71
450	75	9.5	9.499	0.041

Table 5.1: Resonant frequency comparison [Kim et al., 2013b]

5.3.2.3 Inverse modeling (Resonant frequency)

The ANNs can be used when the input/output parameters are exchanged on Figure 5.10. This means that it is able to optimize a switch geometry (L_f) so that the device may have a desired RF performance (f_{res}). This is the so called 'inverse modeling'. Figure 5.11 shows the ANN parameter definition. In addition to the input/output layers, the ANN consists of two hidden layers containing three neurons each, which are determined through the training process.

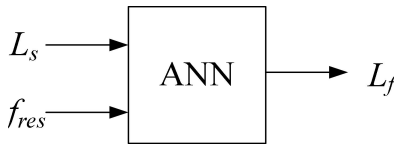

Figure 5.11: ANN parameters for inverse modeling (resonant frequency)

Table 5.2 describes the inverse modeled results by ANNs. With the resonant frequency and the one bridge length, the finger length is quickly calculated. Apart from the previous modeling, the relative errors to the target is somehow high, but considering physical length difference (maximum 5 μm), the result can be still applicable. The prediction error would be decreased if more training sets are used [Kim et al., 2013b].

L_s [μm]	f_{res} [GHz]	$L_{f\|Target}$ [μm]	$L_{f\|ANN}$ [μm]	Relative error [%]
250	13.7	25	24.5	2
250	12.4	75	76.5	2
350	11.6	25	19.5	22
350	10.7	75	70.7	5.7
450	10.2	25	21.4	14.4
450	9.5	75	76.6	2.1

Table 5.2: Inverse modeling using ANN (Resonant frequency) [Kim et al., 2013b]

5.3.2.4 Inverse modeling (Pull-in voltage)

As aforementioned, the mechanical modeling is one of the important parts on the RF MEMS switch design. The RF MEMS switch in Figure 5.7(a) is actuated by an electrostatic force induced by the DC potential on the actuation pad. The minimum potential which can make the bridge down to the CPW center line is the pull-in voltage V_{PI}. The V_{PI} would be one of the most representative electrical parameters related to the mechanical properties, since it is mainly determined by the bridge spring constant, bridge height, anchor and actuation pad design, etc. Because the V_{PI} is determined by the mechanical properties together with the electromagnetic characteristics, its computational estimation has been commonly performed by multi-physics simulators, finite element method (FEM) simulators in general. However, a multi-physics simulator normally requires a heavier resource compared to the single-physics simulator and the effort is further increased when optimization is performed.

This section discusses the mechanical/electromagnetic co-simulation by ANNs. The ANNs can make a quick prediction of a desired parameter with acceptable accuracy. Figure 5.12 describes the ANN parameter definition for the V_{PI} as inverse modeling. The input parameters are L_s and V_{PI}. The output is L_f. With the given L_s and the desired V_{PI}, the ANN estimates the bridge dimension L_f. The ANN consists of 2 hidden layers and each hidden layer involves 25 neurons, which are decided during the training process. The training sets are generated by using a COMSOL Multiphysics simulator [COMSOL Inc., 2013].

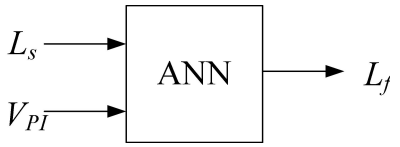

Figure 5.12: ANN parameters for inverse modeling (pull-in voltage)

Table 5.3 shows the ANN simulation results. $L_{f|Target}$ are the desired targets and the $L_{f|ANN}$ corresponds to the ANN outputs. The ANN predicts the bridge dimension L_f with a certain error. If more training sets are provided, the accuracy would be increased. However, it is still meaningful with the current results, since it can provide good starting points which can be used for further multi-physics optimization.

L_s [μm]	V_{PI} [V]	$L_{f\|Target}$ [μm]	$L_{f\|ANN}$ [μm]	Relative error [%]
150	55.6	25	24.877	0.5
150	43	65	66.730	2.7
250	33.3	25	24.281	2.9
350	28.2	65	65.062	0.1
350	25.2	10	11.188	12.0
350	23.8	25	23.986	4.1
350	21.1	65	62.735	3.5
350	20.5	75	74.382	0.8
350	16.9	65	62.466	3.9

Table 5.3: Inverse modeling using ANN (Pull-in voltage) [Marinkovic et al., 2013]

5.4 Conclusion

Inspired by biological neurons, ANNs have been developed as effective estimation tools. It is possible to apply ANNs for RF MEMS switch modeling. Once trained, an ANN can predict the outputs with short time and small computing resource. For some cases, it can even replace the full wave simulation due to its high speed and low computational effort. The drawback of the ANN modeling is that it requires enough training sets normally generated by full wave simulations or measurements. Therefore, it is suitable for specific applications where enough training sets are available. The generation of the training set needs long time and computing resources. However, once the ANN is trained, it can compute the desired outputs in seconds, which is a remarkable advantage compared to the time consuming EM simulation. The advantage is further significant when the switch needs the optimization process requiring multiple simulations. Its application is also extended to multi-physics simulation which is frequently required during the RF MEMS design and development. It is expected that the importance of ANN modeling will be more significant especially in the area of multi-physics simulation which generally needs much more resources compared to single-physics.

6 Conclusion

This thesis has discussed RF device and system designs using RF MEMS switches, which are one of the most representative RF MEMS devices.

As a first example, RF MEMS SPDT satellite redundant switches were demonstrated. Compared to mechanical or solid-state switches, RF MEMS switches have advantages in terms of the size, weight, linearity and power consumption, etc. Since a high isolation performance required in the satellite system cannot be fulfilled by a single switch, several SPDT designs combining different kinds of RF MEMS switches have been employed in this thesis. The measurements of fabricated SPDT switches and the simulations show good agreement, which fulfills the required RF performance.

A next example is a 12x12 RF MEMS switch matrix. The presented switch matrix is based on a 12x12 planar Beneš network which consists of 36 RF MEMS DPDT switches and 12 input/output ports. The switch matrix has been designed to be used at L, S, C and Ku band, which adopts multi-layer LTCC circuit technology. To verify the design process, a simplified 4x4 switch matrix has been designed. The measured results of a fabricated prototype agree well with the simulation. RF MEMS switches on the matrix are controlled by a looping algorithm. The RF MEMS switch matrix is expected to have a 16 cm x 20 cm x 9 cm size and 2.3 kg weight, which is quite small and light compared to commercial 12x12 electromechanical RF switching systems.

The third example for the use of RF MEMS components is a beam steerable leaky wave antenna (LWA) using composite right/left-handed transmission lines (CRLH-TLs). The CRLH-TL is the transmission line approach to electromagnetic metamaterials. It can be used to construct a smart antenna which possesses beam steering capabilities. In CRLH-TLs, it is possible to vary the phase constant β from negative to positive, which enables backward, broadside and forward beam firing. The beam steering is controlled by a tunable balanced CRLH-TL of which reactive loads are varied according to the state of RF MEMS components. The presented LWA has been constructed by cascading several CRLH-TL cells. In this work, the functionality of the CRLH-TL cell has been practically demonstrated by a CRLH-TL cell prototype fabricated on a dielectric substrate. In the prototype cell, the RF MEMS components have been replaced by fixed structures possessing a comparable RF contribution to the cell. As an extension of the 1D beam steerable antenna, a 2D beam steerable antenna has also been proposed, which adopts phase shifters to provide a more broad beam steering capability.

As the last topic, the use of artificial neural networks (ANNs) for RF MEMS switch design and optimization has been discussed. Since most RF MEMS switches consist of

several complicated thin layers, the full wave switch simulation generally requires a high computing resource. An ANN is one of the good solutions to save computing resources on the RF MEMS switch modeling. Starting from the mimesis of the biological neurons, ANNs have been developed to provide a powerful estimating capability with small computing resources. In this work, Ohmic series and capacitive shunt switches using RF MEMS technology have been modeled by ANNs to predict scattering parameters, the resonant frequency and the pull-in voltage. The switch is also inversely modeled to find the corresponding dimension from the desired performance, which can be used for optimization. Even though the ANNs need to be trained by several training sets, they provide quick parameter prediction with acceptable accuracy. This advantage is more pronounced when time consuming optimizations should be performed. ANNs can be used not only to solve electromagnetic problems but also to compute multi-physical ones, such as an RF MEMS switch actuation voltage prediction or a thermal effect estimation, etc.

The RF MEMS technology has been widely applied to RF components and systems. Since they are multi-physical systems, RF MEMS designers should understand multi-physical phenomena involved in the system. However, RF MEMS enable designers to explore new architectures or configurations that have been not feasible with conventional technology. Even though it still suffers from the fabrication yields, reliability and packaging issues, etc., the problems are being solved by maturing the fabrication technology and improvements in the design, which will extend the areas of application usage.

References

Albani, M., Cadili, T., Di Maggio, F., Gardelli, R., Incorvaia, A., Mollura, C., Pomona, I., Russo, M., Sbarra, E., Sorrentino, R., and Gatti, R. (2007). A 2-D electronic beam steering phased array for point-multipoint communication applications. In *European Microwave Conference*, pages 1629–1632, Munich, Germany.

Alexiou, A. and Haardt, M. (2004). Smart antenna technologies for future wireless systems: trends and challenges. *IEEE Communications Magazine*, 42(9):90–97.

Atwater, H. (1985). Circuit Design of the Loaded-Line Phase Shifter. *IEEE Transactions on Microwave Theory and Techniques*, 33(7):626–634.

Baek, C., Song, S., Park, J., Lee, S., Kim, J., Choi, W., Cheon, C., Kim, Y., and Kwon, Y. (2003). A V-band micromachined 2-D beam-steering antenna driven by magnetic force with polymer-based hinges. *IEEE Transactions on Microwave Theory and Techniques*, 51(1):325–331.

Caloz, C. and Itoh, T. (2006). *Electromagnetic Metamaterial: Transmission line theory and Microwave Applications*. JohnWiley & Sons Inc., Hoboken, New Jersey, USA.

Carlson, N. R. (1992). *Foundations of Physiological Psychology*. Needham Heights, Massachusetts: Simon & Schuster.

Chang and Melhem (1997). Arbitrary Size Beneš Networks. *Journal: Parallel Processing Letters - PPL*, 7(3):279–284.

Chao, H. and Liu, B. (2007). *High performance switches and routers*. JohnWiley & Sons Inc., Hoboken, New Jersey, USA.

Computer Simulation Technology GmbH (2010). CST STUDIO SUITE 2010. `https://www.cst.com/`.

COMSOL Inc. (2013). COMSOL. `https://www.comsol.com/`.

De Angelis, G., Lucibello, A., Proietti, E., Marcelli, R., Bartolucci, G., Casini, F., Farinelli, P., Mannocchi, G., Di Nardo, S., Pochesci, D., Margesin, B., Giacomozzi, F., Vendier, O., Kim, T., and Vietzorreck, L. (2012). RF MEMS Ohmic switches for matrix configurations. *International Journal of Microwave and Wireless Technologies*, 4:421–433.

DiNardo, S., Farinelli, P., Giacomozzi, F., Mannocchi, G., Marcelli, R., Margesin, B., Mezzanotte, P., Mulloni, V., Russer, P., Sorrentino, R., Vitulli, F., and Vietzorreck, L. (2006). Broadband RF-MEMS Based SPDT. In *European Microwave Conference*, pages 1727–1730, Manchester, UK.

DiNardo, S., Farinelli, P., Kim, T., Marcelli, R., Margesin, B., Paola, E., Pochesci, D., Vietzorreck, L., and Vitulli, F. (2013). Design of RF MEMS based switch matrix for space applications. *Advances in Radio Science*, 11:143–152.

Dowkey, . M. . E. R. S. (2013). Dow-Key Microwave. `http://www.dowkey.com/_news_attach_files/0/_plk102_1_4701v2.0.pdf`. Accessed: 2013-07-26.

Farinelli, P., Giacomozzi, F., Mannocchi, G., Marcelli, R., Margesin, B., Mezzanotte, P., DiNardo, S., Russer, P., Sorrentino, R., Vitulli, F., and Vietzorreck, L. (2004). RF-MEMS SPDT switch on silicon substrate for space applications. In *Silicon Monolithic Integrated Circuits in RF Systems*, pages 151–154.

Gershenson, C. (2003). *Artificial Neural Networks for Beginners*.

Imanaka, Y. (2005). *Multilayered Low Temperature Cofired Ceramics (LTCC) Technology*. Springer Science + Business Media Inc., Boston, USA.

Ishida, T., Kakushima, K., and Fujita, H. (2013). Degradation Mechanisms of Contact Point during Switching Operation of MEMS Switch. *Journal of Microelectromechanical Systems*, PP(99):1–1.

Jain, A., Mao, J., and Mohiuddin, K. (1996). Artificial neural networks: a tutorial. *Computer*, 29(3):31–44.

Keysight Technologies (2009). Advanced Design System 2009. `http://www.keysight.com/`.

Kim, S., Cunningham, S., McKillop, J., and Morris, A. (2013a). Characterization of dielectric charging and reliability in capacitive RF MEMS switches. In *IEEE International Reliability Physics Symposium (IRPS)*, pages 6B.4.1–6B.4.5, Monterey, USA.

Kim, T., Faz, M., and Vietzorreck, L. (2009). Investigation and optimization of transitions in an LTCC based RF MEMS switching matrix for space applications. In *Asia Pacific Microwave Conference*, pages 988–991, Singapore.

Kim, T., Marinkovic, Z., Markovic, V., Milijio, M., Pronio-Rancic, O., and Vietzorreck, L. (2013b). Efficient modelling of an RF MEMS capacitive shunt switch with artificial neural networks. In *Proceedings of 2013 URSI International Symposium on Electromagnetic Theory (EMTS)*, pages 550–553, Hiroshima, Japan.

Kim, T. and Vietzorreck, L. (2011). Tunable via-free microstrip composite right/left-handed transmission lines using MEMS switches. In *12th International Symposium on RF MEMS and RF Microsystems (MEMSWAVE)*, Athene, Greece.

Kim, T. and Vietzorreck, L. (2012). Investigation of smart antennas using RF-MEMS based tunable CRLH-transmission lines. In *International Conference on Electromagnetics in Advanced Applications (ICEAA)*, pages 266–267, Cape Town, South Africa.

Kim, T. and Vietzorreck, L. (2013). Development of a tunable antenna using RF-MEMS based CRLH-transmission lines. In *21st International Conference on Applied Electromagnetics and Communications*, Dubrovnik, Croatia.

Kim, Y., Kim, N., Kim, J., Lee, S., Kwon, Y., and Kim, Y. (2011). 60-GHz Full MEMS Antenna Platform Mechanically Driven by Magnetic Actuator. *IEEE Transactions on Industrial Electronics*, 58(10):4830–4836.

Kwon, H., Choi, D., Park, J., Lee, H., Park, Y., Kim, Y., Nam, Y., Joo, Y., and Bu, J. (2007). Contact materials and reliability for high power rf-mems switches. In *IEEE 20th International Conference on Micro Electro Mechanical Systems*, pages 231–234, Hyogo, Japan.

Larson, L., Hackett, R., Melendes, M., and Lohr, R. (1991). Micromachined microwave actuator (MIMAC) technology-a new tuning approach for microwave integrated circuits. In *Microwave and Millimeter-Wave Monolithic Circuits Symposium*, pages 27–30, Boston, USA.

Lee, S., Kim, J., Kim, Y., Kim, Y., Cheon, C., and Kwon, Y. (2006). V-band Single-Platform Beam Steering Transmitters Using Micromachining Technology. In *IEEE MTT-S International Microwave Symposium Digest*, pages 148–151.

Lim, S., Caloz, C., and Itoh, T. (2004). Metamaterial-based electronically controlled transmission-line structure as a novel leaky-wave antenna with tunable radiation angle and beamwidth. *IEEE Transactions on Microwave Theory and Techniques*, 52(12):2678–2690.

Marinkovic, Z., Ciric, T., Kim, T., Vietzorreck, L., Pronic-Rancic, O., Milijic, M., and Markovic, V. (2013). ANN Based Inverse Modeling of RF MEMS Capacitive Switches. In *11th International Conference on Telecommunications in Modern Satellite, Cable and Broadcasting Services*, Nis, Serbia.

Matsuzawa, S.-i., Sato, K., Inoe, Y., and Nomura, T. (2006). Steerable Composite Right/Left-Handed Leaky Wave Antenna for Automotive Radar Applications. In *European Microwave Conference*, pages 1155–1158, Manchester, UK.

McCulloch, W. and Pitts, W. (1943). A Logical Calculus of Ideas Immanent in Nervous Activity. *Bull. Mathematical Biophysics*, pages 115–133.

Milijic, M., Kim, T., Marinkovic, Z., Pronic-Rancic, O., Vietzorreck, L., and Markovic, V. (2014). Modeling and optimization of ohmic series rf mems switches by using neural networks. In *GeMiC 2014; German Microwave Conference*, pages 1–4, Aachen, Germany.

Muldavin, J. B. and Rebeiz, G. M. (2000). High-isolation CPW MEMS shunt switches. 1. Modeling. *IEEE Transactions on Microwave Theory and Techniques*, 48(6):1045–1052.

National-Instruments (2008). Redundant System Basic Concepts. `http://www.ni.com/white-paper/6874/en/`. Accessed: 2013-08-06.

National Instruments (2010). AWR 10. `http://www.awrcorp.com/`.

Newman, H. S. (2002). RF MEMS switches and applications. In *40th Annual Reliability Physics Symposium Proceedings*, pages 111–115, Dallas, Texas.

Nguyen, H., Abielmona, S., Rennings, A., and Caloz, C. (2007). Pencil-Beam Full-Space Scanning 2D CRLH Leaky-Wave Antenna Array. In *ISSSE '07. International Symposium on Signals, Systems and Electronics*, pages 139–142, Montreal, Canada.

Pozar, D. M. (2005). *Microwave engineering*. Wiley, USA, 3 edition.

Rebeiz, G. (2003a). RF MEMS switches: status of the technology. In *12th International Conference on Solid-State Sensors, Actuators and Microsystems*, volume 2, pages 1726–1729 vol.2, Boston, USA.

Rebeiz, G. M. (2003b). *RF MEMS Theory, Design, and Technology*. New York: Wiley.

Rebeiz, G. M., Patel, C., Han, S., Ko, C., and Ho, K. (2013). The Search for a Reliable MEMS Switch. *IEEE Microwave Magazine*, 14(1):57–67.

Resistors, D. C. S. B. (2013). DuPont. `http://www2.dupont.com/MCM/en_US/assets/downloads/prodinfo/CF0XX.pdf`. Accessed: 2013-08-06.

Rumelhart, D. and McClelland, J. (1986). *Parallel Distributed Processing*. MIT Press, Cambridge, Mass.

Schobel, J., Buck, T., Reimann, M., Ulm, M., and Schneider, M. (2004). W-band RF-MEMS subsystems for smart antennas in automotive radar sensors. In *European Microwave Conference*, volume 3, pages 1305–1308, Amsterdam, Netherlands.

Spengen, W. M. (2012). Capacitive RF MEMS switch dielectric charging and reliability: a critical review with recommendations. *Journal of Micromechanics and Microengineering*, 22(7).

The MathWorks, Inc. (2010). Matlab 2010. `https://www.mathworks.com/`.

TUM, UniPD, CNR, TAS-I, and FBK (2012). High Reliability MEMS Redundancy Switch. *ESA technical note*.

Volakis, J. (2007). *Antenna Engineering Handbook*. McGraw-Hill Professional, USA, 4 edition.

Yeh, C. and Feng, T. (1992). On a class of rearrangeable networks. *IEEE Transactions on Computers*, 41(11):1361–1379.

List of Supervised Student Projects

Bachelors's Thesis:

- Jingru Yang: Redundancy Circuit Based on RF MEMS switch, 2011.

Master's Thesis:

- Faisal Ahmed: Feed network design for a 60 GHz 6x6 Microstrip patch antenna array, Technical University of Munich, 2009.
- Juan Gonzalez Rodriguez: Antenna matching network using RF MEMS switch, Technical University of Munich, 2009.
- Muhammad Usman Faz: Design of LTCC based switching matrix, Technical University of Munich, 2009.
- Muhammad Imran Inayat: Hybrid integration of RF MEMS switches with LTCC substrate for the design of 8 x 16 switch matrix at 27 GHz, 2009.
- Jian Kang: Development of a tunable antenna using RF-MEMS based CRLH-transmission lines, Technical University of Munich, 2013.

List of Publications of the Author

Kim, T., Faz, M.U., Vietzorreck, L. (2009a). Investigation and optimization of transitions in an LTCC based RF MEMS switching matrix for space applications *Asia Pacific Microwave Conference*, page 988, Singapore.

Kim, T., Vietzorreck, L. (2011a). Tunable via-free microstrip composite right/left-handed transmission lines using MEMS switches *12th International Symposium on RF MEMS and RF Microsystems (MEMSWAVE)* , Athene, Greece.

Kim, T., Vietzorreck, L. (2011a). Analysis of metamaterials using analytic properties *XXXth URSI General Assembly and Scientific Symposium*, page 1581, Istanbul, Turkey.

De Angelis, G., Lucibello, A., Proietti, E., Marcelli, R., Bartolucci,G., Casini, F., Farinelli, P., Mannocchi, G., DiNardo, S., Pochesci, D., Margesin, B., Giacomozzi, F., Vendier, O., Kim, T., Vietzorreck, L. (2012a). RF MEMS ohmic switches for matrix configurations *International Journal of Microwave and Wireless Technologies*, page 421.

Kim, T., Vietzorreck, L. (2012b). Investigation of smart antennas using RF-MEMS based tunable CRLH-transmission lines *International Conference on Electromagnetics in Advanced Applications (ICEAA)*, page 266, Cape Town, South Africa

Kim, T., Vietzorreck, L. (2013a). Development of a tunable antenna using RF-MEMS based CRLH-transmission lines *21st International Conference on Applied Electromagnetics and Communications*, page 550, Dubrovnik, Croatia.

Marinkovic, Z., Ciric, T., Kim, T., Vietzorreck, L., Pronic-Rancic, O., Milijic, M. Markovic, V. (2013b). ANN Based Inverse Modeling of RF MEMS Capacitive Switches *11th International Conference on Telecommunications in Modern Satellite, Cable and Broadcasting Services (TELSIKS)*, page 366, Nis, Serbia.

Kim, T., Marinkovic, Z., Markovic, V., Milijio, M., Pronio-Rancic, O., Vietzorreck, L. (2013c). Efficient modelling of an RF MEMS capacitive shunt switch with artificial neural networks *Proceedings of URSI International Symposium on Electromagnetic Theory (EMTS)*, Hiroshima, Japan.

Vietzorreck, L., Kim, T. (2013d). RF MEMS based systems for space communications *11th International Conference on Telecommunications in Modern Satellite, Cable and Broadcasting Services (TELSIKS)*, page 360, Nis, Serbia.

Kim, T., Kang, J., Che, W., Vietzorreck, L. (2013e). Development of a tunable antenna using RF-MEMS based CRLH-transmission lines *21st International Conference on Applied Electromagnetics and Communications*, page 1, Dubrovnik, Croatia.

Vietzorreck, L., Kim, T. (2013f). Efficient modelling of finite periodicity with the method of lines *Computational Electromagnetics Workshop (CEM)*, page 15.

DiNardo, S., Farinelli, P., Kim, T., Marcelli, R., Margesin, B., Paola, E., Pochesci, D., Vietzorreck, L., Vitulli, F. (2013g). Design of RF MEMS based switch matrix for space applications *Advances in Radio Science*, page 143.

Milijic, M., Kim, T., Marinkovic, Z., Pronic-Rancic, O., Vietzorreck, L., Markovic, V. (2014a). Modeling and Optimization of Ohmic Series RF MEMS Switches by using Neural Networks *GeMiC 2014; German Microwave Conference*, page 1, Aachen, Germany.

Vietzorreck, L., Milijic. M., Marinkovi, Z., Kim, T., Markovic, V., Pronic-Rancic, O. (2014b). Artificial neural networks for efficient RF MEMS modeling *XXXIth URSI General Assembly and Scientific Symposium (URSI GASS)* , page 1, Beijing, China.

Vietzorreck, L., Di Nardo, S., Farinelli, P., Kim, T., Margesin, B., Marcelli, R., Vitulli, F. (2015a). Switch matrix for space applications based on RF MEMS *1st URSI Atlantic Radio Science Conference (URSI AT-RASC)*, page 1, Gran Canaria, Spain.

Kim, T., Klapfenberger, R., Vietzorreck, L. (2016a). Tunable leaky-wave antennas with RF MEMS *URSI International Symposium on Electromagnetic Theory (EMTS)*, page 748, Espoo, Finland.

Marincovic, Z., Kim, T., Markovic, V., Milijic. M., Pronic-Rancic, O., Ciric, T., Vietzorreck, L. (2016b). Artificial Neural Network based Design of RF MEMS Capacitive Shunt Switches *Applied Computational Electromagnetics Society (ACES) Journal*, page 756.